

UNIVERSITY OF CRETE  
DEPARTMENT OF MATERIALS SCIENCE  
AND TECHNOLOGY



---

# Theoretical Study of MoS<sub>2</sub> Defects and Dopants for Hydrogen Evolution Reaction

---

*Author:*  
Maria MINOTAKI

*Thesis Committee:*  
Prof. George KOPIDAKIS  
(*supervisor*)  
Prof. Gerasimos ARMATAS  
Prof. Ioannis REMEDIAKIS

September 8, 2020

# Contents

<b>1</b>	<b>Abstract</b>	<b>3</b>
<b>2</b>	<b>Introduction</b>	<b>4</b>
2.1	Density Functional Theory and Heterogeneous Catalysis . . . . .	4
2.1.1	Catalyst design strategies . . . . .	5
2.1.2	Hydrogen Evolution Reaction . . . . .	6
2.1.3	The Activity descriptor . . . . .	7
2.1.4	The volcano relationship . . . . .	8
2.2	Efficient HER Catalysts . . . . .	10
2.2.1	Pt-based catalysts . . . . .	10
2.2.2	MoS <sub>2</sub> as a HER catalyst . . . . .	11
2.3	Molybdenum Disulfide Catalysts . . . . .	12
2.3.1	MoS <sub>2</sub> mesoporous . . . . .	12
2.3.2	Hybrid MoS <sub>2</sub> /graphene nanostructures . . . . .	13
2.3.3	Lithium ion intercalation . . . . .	13
2.3.4	1T-MoS <sub>2</sub> . . . . .	14
2.3.5	Amorphous molybdenum sulfides . . . . .	14
2.3.6	Molybdenum sulphide molecular clusters . . . . .	15
2.3.7	Doping at the edges of MoS <sub>2</sub> . . . . .	15
2.3.8	Activation of the basal plane via sulphur vacancy formation . . . . .	16
2.3.9	Activation of the basal plane via metal atom doping . . . . .	16
2.4	Theoretical Models for Heterogeneous Catalysis . . . . .	17
2.4.1	The d-band model . . . . .	17
2.4.2	A physical model of MoS <sub>2</sub> basal plane activation . . . . .	18
2.5	DFT in Heterogeneous Catalysis and Future Challenges . . . . .	20
<b>3</b>	<b>Theoretical and Computational Methods</b>	<b>21</b>
3.1	The Many-Particle Problem and Density Functional Theory . . . . .	21
3.1.1	Born-Oppenheimer approximation . . . . .	21
3.1.2	External potential . . . . .	22
3.1.3	Electron density of the ground state . . . . .	22
3.1.4	First Hohenberg-Kohn theorem . . . . .	22
3.1.5	Second Hohenberg-Kohn theorem . . . . .	23
3.1.6	The Kohn-Sham equation . . . . .	23
3.2	Exchange-Correlation Functionals . . . . .	25
3.2.1	Local Density Approximation . . . . .	25
3.2.2	Generalized Gradient Approximation . . . . .	25
3.3	The Pseudopotential Method . . . . .	26
3.3.1	Projector augmented wave method . . . . .	27
3.4	Plane Wave Energy Cutoff . . . . .	28
3.5	K-point Grid . . . . .	29
3.6	Computational Parameters . . . . .	30

<b>4</b>	<b>Theoretical Study of Ni-MoS<sub>2</sub>-V<sub>S</sub></b>	<b>31</b>
4.1	MoS <sub>2</sub> Primitive Cell Convergence Calculations . . . . .	31
4.2	Hydrogen Adsorption on MoS <sub>2</sub> monolayer . . . . .	35
4.3	Hydrogen Adsorption on Ni-MoS <sub>2</sub> . . . . .	38
4.4	Hydrogen Adsorption on MoS <sub>2</sub> -V <sub>S</sub> . . . . .	40
4.5	Hydrogen Adsorption on Ni-MoS <sub>2</sub> -V <sub>S</sub> . . . . .	42
4.6	Comparisons on the Total Electronic Density of States . . . . .	44
4.7	Adsorption Sites of Ni-MoS <sub>2</sub> -V <sub>S</sub> . . . . .	49
4.8	Hydrogen Adsorption Site on the Ring of Basal Plane . . . . .	52
4.9	Hydrogen Coverage Effect on Ni-MoS <sub>2</sub> -V <sub>S</sub> . . . . .	52
4.10	The Heyrovsky step . . . . .	56
4.11	Formation Energy . . . . .	58
<b>5</b>	<b>Rational Design of Metal-doped MoS<sub>2</sub>-V<sub>S</sub></b>	<b>61</b>
5.1	HER Activity on Metal doped MoS <sub>2</sub> -V <sub>S</sub> . . . . .	61
5.2	Hydrogen Adsorption Sites of Metal-doped MoS <sub>2</sub> -V <sub>S</sub> . . . . .	64
5.2.1	Differential charge distribution . . . . .	67
5.2.2	The V <sub>S</sub> adsorption site . . . . .	68
5.2.3	The S0 adsorption site . . . . .	68
5.2.4	The S1 adsorption site . . . . .	69
5.2.5	Hydrogen adsorption on V <sub>S</sub> and S1 . . . . .	70
5.3	Hydrogen Coverage Effect for Metal-doped MoS <sub>2</sub> -V <sub>S</sub> . . . . .	70
5.4	Electronic Density of States for TM-MoS <sub>2</sub> -V <sub>S</sub> . . . . .	72
5.5	Activity-Stability Relationship . . . . .	76
<b>6</b>	<b>Conclusions</b>	<b>79</b>
<b>7</b>	<b>Appendix</b>	<b>82</b>
7.1	H <sub>2</sub> Energy Convergence Calculations . . . . .	82
7.2	H <sub>2</sub> S Energy Convergence Calculations . . . . .	83
7.3	Mo(bcc) Energy Convergence Calculations . . . . .	84
7.4	Ni(fcc) Energy Convergence Calculations . . . . .	86
<b>8</b>	<b>References</b>	<b>97</b>

# 1 Abstract

Hydrogen is one of the predominant clean and renewable alternatives to fossil fuels. Efficient and sustainable hydrogen production is key to its widespread use as an energy carrier in the near future. Catalysts based on precious metals are currently used in hydrogen evolution reaction (HER). Molybdenum disulfide ( $\text{MoS}_2$ ) is an earth-abundant, low cost, layered material with a variety of interesting properties, which depend on its dimensionality and structure. Previous work has established that while basal planes of  $\text{MoS}_2$  nanostructures are inert, their edges are catalytically active in HER. In an effort to increase the number of active sites for HER in  $\text{MoS}_2$  nanoparticles, Density Functional Theory (DFT) calculations were performed to examine the hydrogen adsorption ability of  $\text{MoS}_2$  basal plane when modified by defects and dopants. The hydrogen adsorption free energy ( $\Delta G_H$ ) was employed as the main activity descriptor. Introduction of a sulfur vacancy in combination with a nearby Mo-atom substitution by a transition metal enhance basal plane activity. Parameters such as hydrogen adsorption sites, hydrogen coverage, hydrogen molecule desorption mechanisms, and stability, are examined. Our findings suggest that the combination of a single Ni atom dopant and a sulfur vacancy formation in the  $\text{MoS}_2$  basal plane has the maximum performance compared to several other metal dopants. Results with other transition metals provide insight into the activation mechanism of the  $\text{MoS}_2$  basal plane. A volcano relationship exists between activity descriptor and exchange current density. The relationship between activity and stability descriptors for these systems is also examined. Finally, guidelines for the design of efficient and stable  $\text{MoS}_2$ -based catalysts for HER using DFT calculations are outlined.

## 2 Introduction

### 2.1 Density Functional Theory and Heterogeneous Catalysis

Catalysts are key factors for enhancing reactions rates [1, 2], involving transportation fuel production, such as petrol as well as chemicals such as ammonia [5].

The excessive use of fossil fuels and byproducts, has generated serious environmental problems. The aim of science in the field of renewable energy is to become independent of fossil fuels and eliminate the amount of CO<sub>2</sub> emissions. The development of efficient chemical reactions is crucial for the energy sector. Precious metals as catalysts can neutralize the negative impact of these reactions, but are high in cost. Hence, the design and development of highly active and selective catalysts from earth-abundant resources is important for the energy future.

Heterogeneous catalysis is a key factor in the energy sector. The chemical bonding between a molecule and a surface is of fundamental importance. The surface is usually a metal in solid phase, while the molecule exists in liquid-gas phase. Thus, the surface chemistry involves mainly two scientific fields, condensed-matter physics and chemistry [2]. However, heterogeneous catalysis cannot be explained in common terms of these fields. This is because the metal is a semi-infinite source of electrons at the Fermi level, so that the usual electron conversion rules do not apply. In addition, it is a complex reaction, having a variety of intermediates, transition states, different behaviour to solution environments and in many cases the interfaces between the material and adsorbate is in a complex phase, such as gel-like [1,2].

It is essential to reveal the important factors connected with the catalytic activity. The electronic structure of a material determines its catalytic properties. So modifications in its composition and physical structure can tune its performance. This method is also used for catalytic materials, batteries, hydrogen storage, optical adsorption and in homogeneous catalysis [1].

An important factor for a catalysis reaction is its kinetics. It connects the microscopic properties, such as adsorption energies and kinetic barriers with the macroscopic ones which can be observed via experiment, activity, selectivity and stability. The description of their kinetics, requires all the reaction free energies and activation energy barriers, making it a demanding task. Microkinetic models can be developed for each new catalyst, however in most cases, due to computer limitations, this is not feasible. Energy correlations between intermediates and transition states provide a decrease in the complexity and an elimination of the independent descriptors. The development of models of surface reactivity that accounts only for the most important microscopic properties corresponding to macroscopic properties is essential. The identification of the active sites in the catalyst surface is also important and depends on the complexity of the catalysts surface.

The selectivity is as crucial as the activity of a catalyst. It favours specific reaction pathways among competitive ones. In practice, it can offer cleaner chemistry, better environmental protection and economical production. An optimal catalyst should balance between selectivity and activity [1,2].

In order to develop an efficient catalyst, the necessary requirements are activity, selectivity and low cost for industrial viability. Then, a variety of other parameters have to be taken into account: the long-term stability, the lack of side-products, the efficiency on poison substances, the production cost, the enhancement in efficiency under secondary promoters, the role of defects and substrates. These characteristics can be explored through computational simulations, but the determining factor is its functionality under experimental conditions [1,2]. The advances on Density Functional Theory (DFT) make the description of catalytic reactions on surfaces possible and provide a deeper insight in the variations between different catalysts.

### 2.1.1 Catalyst design strategies

In order to enhance the activity of a catalyst through the increase of the reaction rate, two main strategies are followed. The first one is increasing the number of exposed sites responsible for the activity. This can be achieved either by loading more material or by nanostructuring the catalyst to create more active sites. The main drawback of this method is that by loading more material, a charge and mass transport limitation appears. So after adding a high amount of material, no more improvement is observed in catalyst's activity. In Figure 1 below, a stage condition appears in the diagram of the performance versus the increasing of number of active sites, in accordance to this limitation.

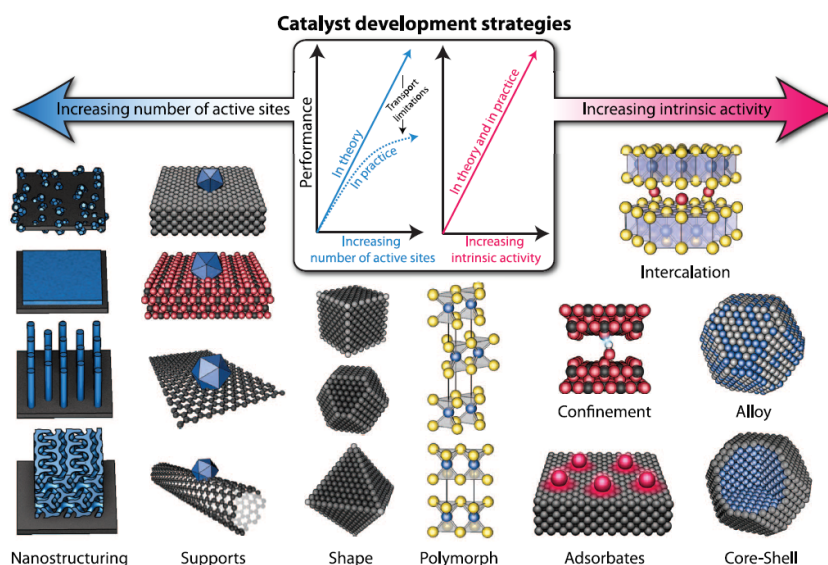


Figure 1: The two main catalyst design strategies, the increase of the number of active sites and the increase of the intrinsic activity. Various methods for each strategy are depicted. In the center of the figure, there are diagrams of their performance [10].

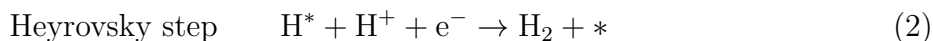
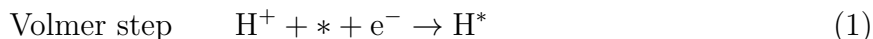
The second strategy employs the increase in intrinsic activity of each active site by modifying catalyst's physical and chemical properties. This can be achieved by techniques including alloying, surface structure doping, strain, core-shell creation, intercalation, confinement of adsorbate in the catalyst surface. The transport issues are alleviated, as a direct increase in their activity occurs. Because it requires less amount of material for a functional catalyst, it is a more economical way. Finally, a combination of these two methods can be applied.

There is a great difference in the performance of the best and the worst catalyst between the two main strategies. In the first case, the performance of the best in comparison to the worst catalyst is by 1 to 3 times greater. However, for the intrinsic activity method, this difference is about 10 times higher [9, 10].

### 2.1.2 Hydrogen Evolution Reaction

Hydrogen Evolution Reaction (HER) is a special reaction in electrochemistry. It is involved in many technologies as a side reaction and it is an efficient way for hydrogen production [11]. It follows the reaction :  $2\text{H}^+ + 2\text{e}^- \rightarrow \text{H}_2$ , where protons from the solution combine with electrons from the electrode and form a hydrogen molecule, releasing it from the catalyst surface. The role of the catalyst is to increase the reaction rate by minimizing the overpotential of the reaction.

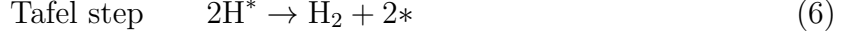
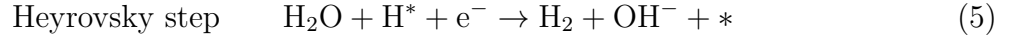
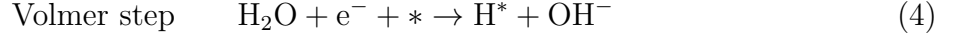
When conducted in acidic solution, it consists of a two step reaction mechanism, with two electron transfers and one intermediate, the hydrogen adsorbate  $\text{H}^*$ . It can be achieved either by Volmer-Heyrovsky or Volmer-Tafel mechanism :



where  $*$  refers to the catalyst adsorption site and  $\text{H}^*$  to an adsorbed hydrogen atom. According to these pathways, initially hydrogen adsorption occurs on the catalyst activation site through Volmer step. A proton from the solution combines with an electron from the electrode and forms a hydrogen atom, adsorbed on the catalyst surface. Then, the reaction continues by following one of the two possible ways. When the adsorbed hydrogen atom combines with a proton from the solution, they form a hydrogen molecule leaving the surface, according to the Heyrovsky step. However, when two neighbour hydrogen adsorbates are in a short distance, they interact with each other and form a hydrogen molecule that leaves catalyst surface, following the Tafel step [9-12].

The rate of the reaction depends on the interaction between  $\text{H}^*$  and catalyst's surface, the number of available adsorption sites and the pH of the solution. According to studies, low pH in acidic environment favours Pt-group catalysts. Because they are expensive, they cannot be utilized for industrial purposes. Ni-based catalysts are less expensive, but perform poorly and have low stability in acidic solutions [11].

Hydrogen is also produced through water molecules via HER in alkaline solutions:



Research work shows that in alkaline conditions the reaction has a slower rate in Volmer step than in acidic ones, because of water dissociation. Considering this and the fact that more experimental data exist for HER in acidic media [11], the focus of this study is on HER under acidic environment.

### 2.1.3 The Activity descriptor

The binding of hydrogen adsorbate in the catalyst surface is a key element for the reaction rate. Nørskov et al introduced an activity descriptor, the hydrogen adsorption free energy  $\Delta G_H$  [1]. It is defined by the relationship :

$$\Delta G_H = \Delta E_H + \Delta E_{ZP} - T\Delta S_H \quad (7)$$

where,  $\Delta E_H$  is the binding energy of hydrogen:

$$\Delta E_H = E_{(\text{monolayer}+n\text{H})} - E_{(\text{monolayer}+(n-1)\text{H})} - E_{\text{H}_2/2} \quad (8)$$

where n is the number of adsorbed hydrogen atoms in the catalyst surface,  $E_{(\text{monolayer}+n\text{H})}$  is the energy of the catalyst, the monolayer MoS<sub>2</sub> in this study, with n hydrogen atoms adsorbed,  $E_{(\text{monolayer}+(n-1)\text{H})}$  is the energy of the monolayer with n-1 adsorbed hydrogen atoms and  $E_{\text{H}_2}$  is the energy of H<sub>2</sub> molecule in the gas phase.

In case that one hydrogen is already adsorbed in the system and a second one is introduced, n = 2 in equation (8), the differential hydrogen adsorption free energy  $\Delta G_H^{diff}$  is defined.

The last two terms in (7) are the difference in zero point energy  $\Delta E_{ZP}$  and entropy  $\Delta S_H$  in the adsorbed and gas phase state of hydrogen molecule, respectively. There is a variation in the values of the last two terms. For this work, based on studies, the sum of the last two terms is 0.24 eV. Thus,  $\Delta G_H = \Delta E_H + 0.24 \text{ eV}$  [7].

When the binding of the adsorbate with the catalyst active site is too strong, with negative  $\Delta G_H$ , the adsorption sites are occupied by the adsorbates, so there are no available sites for new ones to bind and the catalyst is poisoned. In case of positive  $\Delta G_H$ , the adsorbate does not interact with the catalyst and the reaction does not occur [7].

For HER specifically, the interaction with the adsorbate has an impact in the reaction rate. If  $\Delta G_H > 0$ , a weaker interaction suggest a weak adsorption during the Volmer step that decreases the rate of the reaction. For  $\Delta G_H < 0$ , Heyrovsky or Tafel step is slower as the desorption of hydrogen molecule is more difficult.

Hence, the hydrogen adsorption free energy should be close to zero for an efficient catalyst, so that the catalytic material should bind hydrogen not too strongly and not too weakly in accordance to Sabatier principle [13]. However, we should consider that this condition is necessary, but not sufficient for an efficient HER and other factors need to be considered that will be discussed later.

### 2.1.4 The volcano relationship

In Hydrogen Evolution Reaction at equilibrium potential, the exchange current density  $i_0$  shows the intrinsic rate of electron to transfer between the electrode and the solution. In case that the proton transfer is exothermic with  $\Delta G_H < 0$ , the exchange current density is [7]:

$$i_0 = -ek_0 \frac{1}{1 + \exp(-\Delta G_H/k_B T)} \tag{9}$$

where, the rate constant  $k_0$  encloses the results of solvent reorganization when the proton transfers to the surface. It is set to  $200 \text{ s}^{-1} \text{ site}^{-1}$ . The  $k_B$  constant is Boltzmann constant. The reaction is conducted at  $\text{pH} = 0$  and  $T = 300\text{K}$  according to standard conditions. When,  $\Delta G_H > 0$  and proton transfer is endothermic, the expression for exchange current density becomes [7]:

$$i_0 = -ek_0 \frac{1}{1 + \exp(-\Delta G_H/k_B T)} \exp(-\Delta G_H/k_B T) \tag{10}$$

Considering the above two relationships, a volcano curve occurs from the fitting between exchange current density and hydrogen adsorption free energy, as it is depicted in Figure 2(a) [1,3,4,7]. The positions on the plot of the depicted metals determine their rate of reaction.

Three main areas exist in the volcano curve: the area with negative  $\Delta G_H$  values or the descending branch, the area with positive  $\Delta G_H$  or the ascending branch and the area on the top [7, 10].

On the descending branch, as we move away from the top,  $\Delta G_H$  becomes more negative and the rate of HER decreases. The lack of available sites for proton recombination, decreases the entropy term in (7), because adsorbed hydrogen binds strongly to catalyst surface, as  $\Delta E_H$  is negative [7].

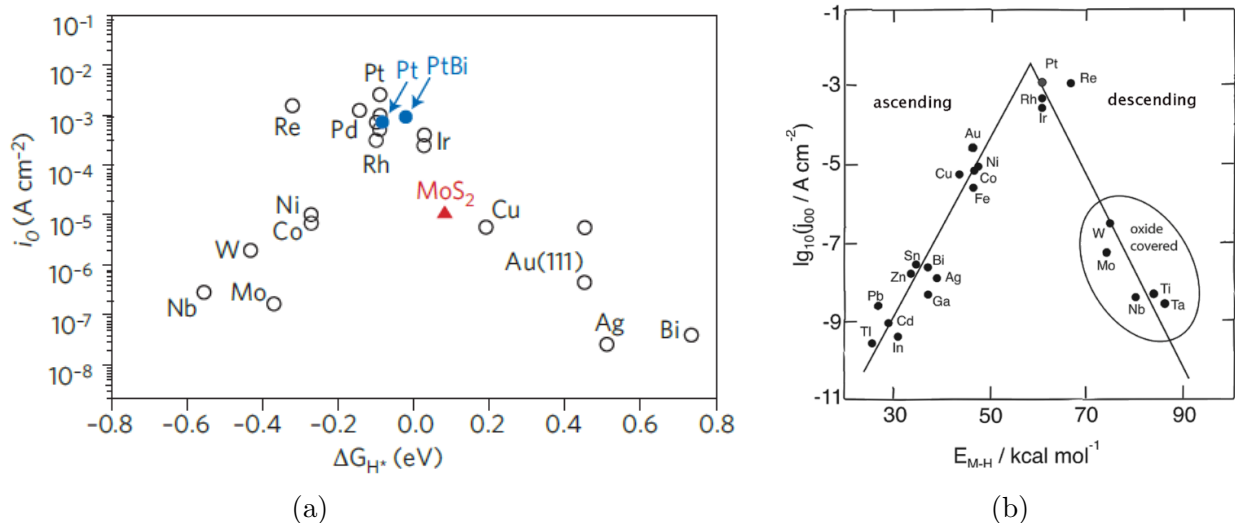


Figure 2: (a) Volcano plot for exchange current density versus hydrogen adsorption free energy for various transition metal surfaces [1,3,4,7], (b) The Trassati volcano curve. The circled area indicates the oxide covered metals that are not functional during the HER [15].

The ascending branch follows the same trend as the previous case, with the difference that  $\Delta G_H$  becomes more positive away from the top, decreasing the HER rate. This happens because the system of adsorbed hydrogen on catalyst surface is not stable. Thus, it has a positive  $\Delta E_H$  from (8). In addition, the entropy term increases due to the availability of hydrogen possible positions. So, from (7), we obtain a positive value that follows  $\Delta E_H$  increase, so that the rate of hydrogen adsorption at Volmer step is limited [7].

At the top of the volcano curve, where  $\Delta G_H \approx 0$ , catalysts with the maximum performance exist. For example, in Figure 2(a), Pt is at the top of the volcano curve, suggesting the most efficient catalyst. In the area near the top, while the majority of the metals are efficient, they are precious and scarce, so is not economically viable for industrial use [4, 7]. The Mo-edge of MoS<sub>2</sub> is close to the top in the ascending branch with a value around 0.08 eV [6]. Because, in the descending branch are mainly metal oxide metals, their efficiency during HER is questioned and consequently the existence of an actual volcano curve. These features will be discussed in next paragraphs of this work. Finally, the position of Ni metal surface in the descending branch, having good performance and not been oxidized during HER, in combination with its properties such as being earth abundant and low cost, makes it a promising material for designing high efficiency catalyst for HER [16].

The volcano relationships derived from the description of reaction rates and adsorption free energies have an important role in heterogeneous catalysis. They help identify the most suitable catalytic materials, especially those at the maximum of the volcano, for the selected descriptors [1,2].

They reveal which surfaces can be poisoned due to the strong binding of adsorbate and which have a high dissociation barrier [2]. The design of new catalysts can also be based on volcano relationships. For example, it can determine the alloying components needed for an increase in the intrinsic activity of a material. From the position of the metals in the volcano curve, a prediction for a possible efficient combination of two metals can be made for a reaction. For example, according to Figure 2(a), PtBi alloy was produced, having a greater activity than Pt surface [4] and greater stability than Bi supported on Pt [14] [1,2].

It has to be mentioned that before the development of DFT calculations, thermodynamic data such as heat of formation was used as activity descriptor [1, 15, 16]. For example the Trascatti Volcano Curve (Figure 2(b)) was the first volcano curve for the HER, expressing the exchange current density in regards to the energy of hydride formation. However, its descending branch has only oxide covered metals (W, Mo, Nb, Ti and Ta) that are not functional during HER, raising a controversy around the actual existence of volcano relationships [15, 16].

From a different point of view, there is a similarity in the idea of the volcano plots in catalysis and the outer sphere electron transfer reactions. Based on Marcus' theory a plot of the reaction rate in regards to the free energy  $\Delta G$  should reach its maximum value when  $\Delta G = -\lambda$ , where  $\lambda$  is the energy of solvent reorganisation. The descending branch with  $\Delta G < 0$  is the inverted region. The negative energy value suggests that no energy is needed for the reaction (exergonic reaction) [16, 17]. However, for the ascending branch with positive energy values, energy is needed and the reaction cannot occur spontaneously (endergonic reaction). From the study of volcano curves, there is need for metals with  $\Delta G < 0$  near Marcus' inverted region. Also, from studies of HER in alkaline and acidic media, only Ni metal is a promising candidate, as the other metals in the descendent branch are precious metals [16].

## 2.2 Efficient HER Catalysts

### 2.2.1 Pt-based catalysts

As we mentioned before, the Pt(111) surface is one of the most efficient catalyst for HER [7]. It has a  $\Delta G_H$  value close to zero for hydrogen coverage  $\theta_H = 1$  ML. This means that despite having excellent activity, it is highly dependent on hydrogen coverage, so that it requires a great amount of adsorbed hydrogen atoms in its surface to reach its high performance [3, 18-20].

There is need for efficient, earth abundant and low cost catalysts. The Mo-edge of MoS<sub>2</sub> is referred to have  $\Delta G_H = 0.08$  eV for  $\theta_H = 0.25$  ML, so that it needs only 1 of 4 adsorption edge sites to be efficient. If further activation of its edges is achieved, it can alter its performance by 4 times [3,6]. For example, various transition metal dopants as Mo substitutions at its edges were examined [21, 22]. Hence, for designing efficient catalysts, except from their activity, the hydrogen coverage effect needs to be considered [3, 10].

### 2.2.2 MoS<sub>2</sub> as a HER catalyst

Initially, MoS<sub>2</sub> was thought to be catalytically inert for HER [21]. Inspired by the enzymes in nature that produce hydrogen, nitrogenase and hydrogenase, that contain active areas for HER with non-precious metals such as Fe, Mo, Co, further research was conducted at the edges of MoS<sub>2</sub> that have a similar structure (Figure 3(a))[24]. From DFT calculations it was derived that for hydrogen coverage 0.25 ML the Mo-edge has a  $\Delta G_H = 0.08$  eV, close to zero [6]. However, the basal plane is catalytically inert with a  $\Delta G_H$  equal to 1.92 eV [25].

The first experiment that confirms MoS<sub>2</sub> edges activity was conducted on MoS<sub>2</sub> nanoparticles supported on graphite that generated an overpotential of 0.1-0.2 eV (Figure 3(b)) [6]. Studies on MoS<sub>2</sub> nanoparticles on Au(111) with size as an adjustable parameter were conducted and reveal a linear response between the number of edge sites on MoS<sub>2</sub> catalyst and HER activity. Moreover, the surface area does not have any impact to its performance (Figure 3(c))[3]. These theoretical and experimental results led to a design strategy of nanostructured materials with exposed edge sites in order to increase their HER performance [10].

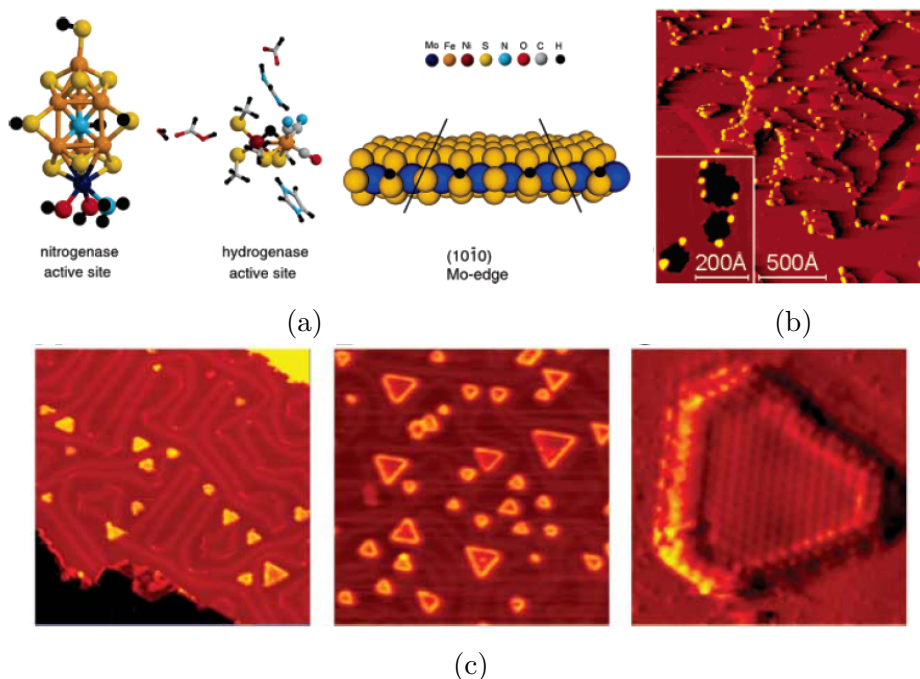


Figure 3: (a) Hydrogen producing enzyme's active sites and Mo edge of MoS<sub>2</sub> with sulphur coverage  $\theta_S=0.5$  ML and hydrogen coverage  $\theta_H=0.5$  ML [6, 24], (b) Representative STM images of MoS<sub>2</sub> nanoparticles on graphite [6] and (c) STM images of MoS<sub>2</sub> nanoparticles on Au(111) [3].

## 2.3 Molybdenum Disulfide Catalysts

In the following section we try to provide an overview of the most important current developments on Molybdenum Disulfide Catalysts for HER developed from the two main strategies mentioned before.

### 2.3.1 MoS<sub>2</sub> mesoporous

Nanostructured MoS<sub>2</sub> catalysts were synthesized following the strategy to increase the active sites of the catalytic material. The mesoporous double gyroid MoS<sub>2</sub> is a representative example (Figure 4(a)). Its high curvature is responsible for the mitigation of the formation of large basal planes and the increase in the density of edge sites [24]. The main disadvantage of this material is the existence of resistivity losses. This is because the electron mobility perpendicular to MoS<sub>2</sub> basal plane is lower than in-plane, so there is a decrease in the electron transport distance between the active site to the conductive substrate [9, 10].

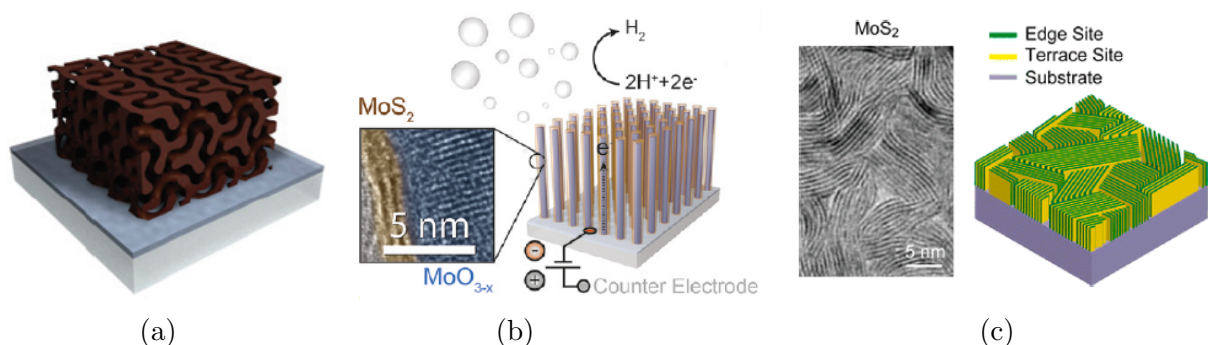


Figure 4: (a) Three dimensional model of MoS<sub>2</sub> double gyroid mesoporous structure [9, 26]. (b) Core-shell MoO<sub>3</sub>-MoS<sub>2</sub> nanowires. The MoS<sub>2</sub> is responsible for the HER activity and MoO<sub>3</sub> for the electron transport [9, 27]. (c) (Left) TEM image of vertically aligned MoS<sub>2</sub> sheets and (right) illustration of the edge sites and sheets on a substrate.[9, 28]

Another catalytic material that provides a high number of active sites is core-shell MoO<sub>3</sub>-MoS<sub>2</sub> nanowires (Figure 4(b)). It is a combination of the MoO<sub>3</sub> core that enables the charge transport through the nanowire and MoS<sub>2</sub> shell, having a high catalytic activity and protecting the structure from corrosion in acidic environments [27].

In order to cease the resistivity losses, vertically aligned MoS<sub>2</sub> thin films were designed (Figure 4(c)). They possess a large amount of active sites and they are capable, via a high speed electron transfer, to minimize the resistivity losses of electron transport from the single MoS<sub>2</sub> film to the conductive substrate [28, 29].

### 2.3.2 Hybrid MoS<sub>2</sub>/graphene nanostructures

The combination of nanoparticles and supports of large surface area is another way to design efficient catalytic materials [10]. The MoS<sub>2</sub> nanoparticles on reduced graphene oxide (RGO) nanosheets were derived from this method. Because of their distribution on RGO substrate, changes in the morphology of MoS<sub>2</sub> nanoparticles appear that increase the number of active edge sites. In addition, the electronic coupling with graphene alters the charge transfer [30].

DFT calculations on hybrid MoS<sub>2</sub>/graphene nanoparticles and free-standing ones, reveal that the existence of a support triggers a strain effect, which can have a great impact in the adsorption of hydrogen on MoS<sub>2</sub> nanostructures [31].

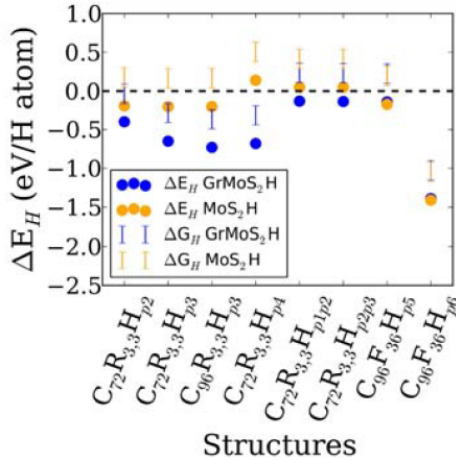


Figure 5: Hydrogen adsorption free energy ( $\Delta G_H$ ) and hydrogen binding energy ( $\Delta E_H$ ) of MoS<sub>2</sub>/graphene nanostructures in comparison with the respective free standing ones [31].

### 2.3.3 Lithium ion intercalation

Lithium ion intercalation is used to chemically exfoliate MoS<sub>2</sub> into metallic 1T-MoS<sub>2</sub> nanosheets. The introduction of Li ions into van der Waals gaps of 2H-MoS<sub>2</sub> applies in this method [10, 32-34].

It has three crucial effects in the electronic structure of MoS<sub>2</sub>. The Li ions are responsible for increasing the distance between the layers, so that they separate them. Also, they change the filling of d-band states and the oxidation state of Mo decreases. Consequently, an improvement in the interaction with the hydrogen and HER activity and can be achieved. Finally, when Li ions concentration is high, a phase transition from semiconducting 2H-MoS<sub>2</sub> to metallic 1T-MoS<sub>2</sub> is achieved. In this case, the conductivity increases, so the basal plane is active for HER [9, 29].

An important consequence of the intercalation is that the produced 1T-MoS<sub>2</sub> has, except from its edges, an active basal plane for HER. According to Figure 6, for 2H-MoS<sub>2</sub>, its activity is significantly reduced after oxidation, while 1T-MoS<sub>2</sub> is not affected [33]. This confirms that 1T-MoS<sub>2</sub> has an active basal plane, so the focus of research moved to this metallic polymorph of MoS<sub>2</sub>.

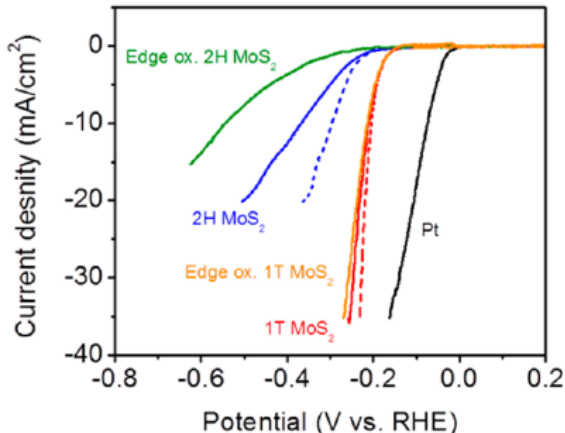


Figure 6: Polarization curves of 2H and 1T-MoS<sub>2</sub> nanosheet electrodes before and after edge oxidation. The dashed lines represent the iR-corrected polarization curves [33].

### 2.3.4 1T-MoS<sub>2</sub>

As we mentioned before the edges of 1T-MoS<sub>2</sub> are not the only active sites, but also it is its basal plane [33]. The catalytic mechanism was also investigated for 1T-MoS<sub>2</sub>. It was found that the Volmer-Heyrovsky mechanism is kinetically preferred. The hydrogen coverage has an impact on the catalyst functionality [35]. Further enhancement in HER activity can be achieved with metal doping [35, 37].

### 2.3.5 Amorphous molybdenum sulfides

Amorphous molybdenum sulfides (MoS<sub>x</sub>) are one of the most active non-precious HER catalysts, mainly due to their large surface area morphologies [38, 41]. They are synthesized with processes that do not involve thermal sulfidation treatment, such as electrodeposition or wet chemical reactions [9, 10, 37, 38]. They find applications both for electrochemical and photocatalytic water splitting devices [39, 40].

From their physical and chemical characterization, their active surface composition is closer to MoS<sub>3</sub>. However, under reducing potentials, it resembles more MoS<sub>2</sub>. In addition, it is difficult to identify the specific active edges [9, 10, 38, 41]. The introduction of dopants such as Fe, Co and Ni can alter their HER performance [10, 42].

### 2.3.6 Molybdenum sulphide molecular clusters

Another interesting category is Molybdenum Sulphide Molecular Clusters supported on electrode substrates. Inspired by enzymes in nature that produce hydrogen, with an active center containing metal atoms such as Fe, Ni and Mo binding to sulphur [6], biomimetic electrocatalysts are synthesized with low cost and earth abundant metals. Their activity derives from the high density of active sites with intrinsic tunability of edge sulphur atoms [43].

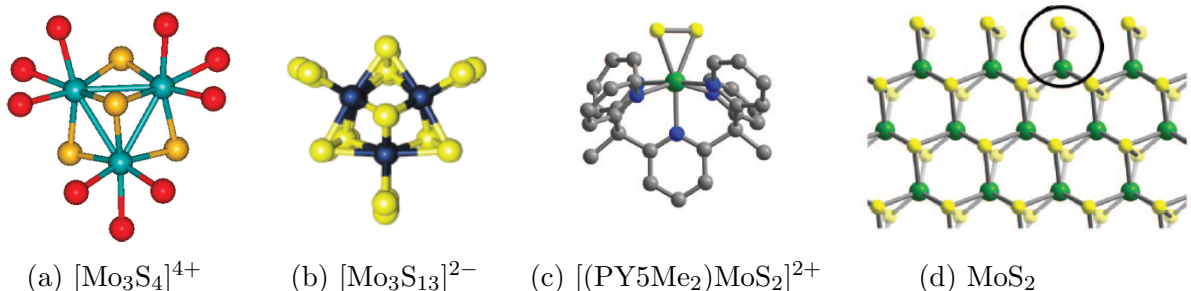


Figure 7: Structural models of (a) cubane- $[\text{Mo}_3\text{S}_4]^{4+}$  [43, 44], (b)  $[\text{Mo}_3\text{S}_{13}]^{2-}$  complex [10, 47]. Blue : Mo, yellow : S and red : O (from water ligand), (c)  $[(\text{PY5Me}_2)\text{MoS}_2]^{2+}$  with  $\text{Mo}^{IV}$ -disulfide complex and (d)  $\text{MoS}_2$ , adapted from [46, 43]. The molecular clusters are designed to mimic  $\text{MoS}_2$  edge (cycled area). Green : Mo, yellow : S, blue : N and gray : C.

The Molybdenum Sulphide Molecular clusters are a combination of molecular and solid state electrocatalysts. Small molecular units of molybdenum sulfide are connected with undercoordinated sulphur atoms. In many cases their structure mimics  $\text{MoS}_2$  edge sites (Figure 7(d)), so that their performances are equal [9, 10, 43]. Some representative examples are cubane-type  $[\text{Mo}_3\text{S}_4]^{4+}$  [44, 45] (Figure 7(a)), thiomolybdate  $[\text{Mo}_3\text{S}_{13}]^{2-}$  clusters [47] (Figure 7(b)) and  $\text{Mo}^{IV}$ -disulfide complex [46] (Figure 7(c)).

### 2.3.7 Doping at the edges of $\text{MoS}_2$

Initially, DFT calculations were performed to examine the promoted and unpromoted  $\text{MoS}_2$  hydrosulfurization catalysts. It was found that the promoter atoms (Co, Ni and Fe) prefer to locate at S-edge of  $\text{MoS}_2$  [46].

Later, DFT calculations were performed to examine the hydrogen adsorption ability of  $\text{MoS}_2$  edges under the substitution of Mo at S-edge with various transition metals (TM) [21, 22]. In addition, the sulphur and hydrogen coverages at their edges have an important role to their activity. The Ru, Rh, Co, Fe, Mn and Ta dopants are possible candidates. The introduction of TM modifies the strength of sulphur binding on the edges, so that the more reactive is the TM dopant, the weaker is the hydrogen binding. This is expressed with a negative linear relationship between a stability descriptor  $\Delta G_S$  and hydrogen adsorption descriptor  $\Delta G_H$  [21].

### 2.3.8 Activation of the basal plane via sulphur vacancy formation

The first activation of HER for monolayer 2H-MoS<sub>2</sub> basal plane was conducted with the formation of sulphur vacancies. The existence of new gap states around the Fermi level (Figure 8) are responsible for the hydrogen binding to Mo atoms of the active area. Strain engineering on the sulphur vacancy sites can tune the electronic band structure, so an optimization of  $\Delta G_H \approx 0$  eV can be achieved [49].

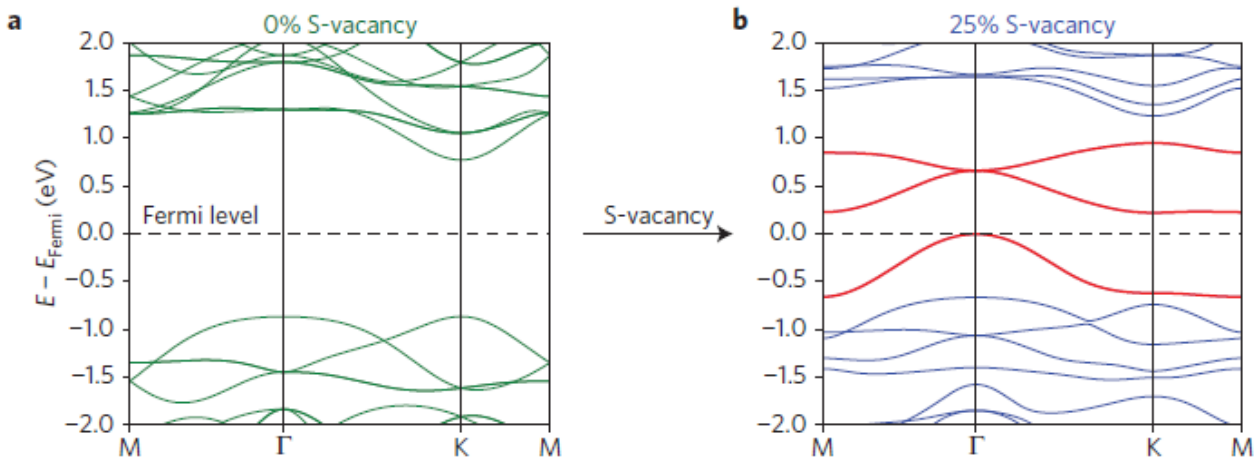


Figure 8: Electronic band structure of monolayer 2H-MoS<sub>2</sub> (a) without and (b) with sulphur vacancies concentration. New gap states (red color) appear near the Fermi level for the S-vacancies case [49].

Argon plasma desulfurization is a process for sulphur vacancy creation [50]. However, it is not an industrially viable process, so an electrochemical desulfurization method was developed by Tsai et al [51].

### 2.3.9 Activation of the basal plane via metal atom doping

Single atom doping can trigger the catalytic activity of MoS<sub>2</sub> basal plane. Substitution of Mo with a Pt dopant in MoS<sub>2</sub> basal plane produces a highly active and stable system. The Pt dopant is able to modify the adsorption ability of its neighbour sulphur atoms. A volcano plot was constructed for various TM-doped MoS<sub>2</sub> systems to find the trends of the activation of MoS<sub>2</sub> basal plane [52]. Similar results were produced by Hakala et al, using a machine learning model, especially for Fe, Co, Ni, Cu and Pt doped systems [22]. It was found that Co is the most favourable non-precious metal dopant [22, 52, 53].

According to the latest experimental and theoretical study, the combination of a transition metal dopant and a sulphur vacancy has a different response. Under these circumstances, the Co dopant deactivates the sulphur defects in the basal plane. Instead, the Ni dopant is able to alter their HER activity [54]. A physical model for the activation of sulphur atoms of the basal plane for MoS<sub>2</sub> systems was proposed by Liu et al. that we will present in detail in another section [55].

## 2.4 Theoretical Models for Heterogeneous Catalysis

In the next sections the d-band model and a physical model especially for MoS<sub>2</sub> catalysts are reviewed. The first one was developed by Nørskov et al. and have been applied in various systems [56,58], while the other one has been proposed recently [55].

### 2.4.1 The d-band model

In the pursuit of explaining the behaviour of bonding between surfaces and molecules various models were proposed. In the paragraphs below the d-band model is explained. It derives from the study of the nobleness, the inability of a metal to form or break bonds, for transition metal surfaces in regard to hydrogen. Some interesting findings occur that can apply to other surfaces and molecules [56, 57].

A model of two factors was introduced to explain the overlapping of two atoms based on quantum mechanics theory. Due to orthogonalization of their orbitals, there is a repulsion between the two atoms. However, the hybridization between them is responsible for the bonding and antibonding states that are introduced [56].

The degree of filling of antibonding adsorbate-metal states contributes to the degree of bonding formation. Moreover, the orbital overlap with the adsorbate, which is expressed by the coupling matrix element, is also responsible for the interaction [56].

If both bonding and antibonding states are occupied, there is no gain of hybridization and repulsion happens between the adsorbate and the surface. In case that only bonding states are filled, the attraction is greater than the repulsion from orthogonalization, so the surface is reactive for adsorption [56].

Variations among the different transition metals occurs due to the coupling matrix element [56, 57]. It expresses the orthogonalization of the orbitals, so that for higher values the overlap between adsorbate and surface is smaller. It is increased from top to bottom for atoms within the same group of periodic table and from right to left for atoms of the same row.

For example, it explains the greater nobleness of Au compared to Cu. Both belong to the same group, but Au is in the top of the group, so that the overlap with hydrogen is smaller and Au is less reactive [56].

An application of this model is the explanation of the nobleness of Au(111) and Cu(111) surface to hydrogen molecule, in contrast to the high active Ni(111) and Pt(111) surfaces. Figure 9 illustrates their Density of States (DOS) for the surface-H systems [56].

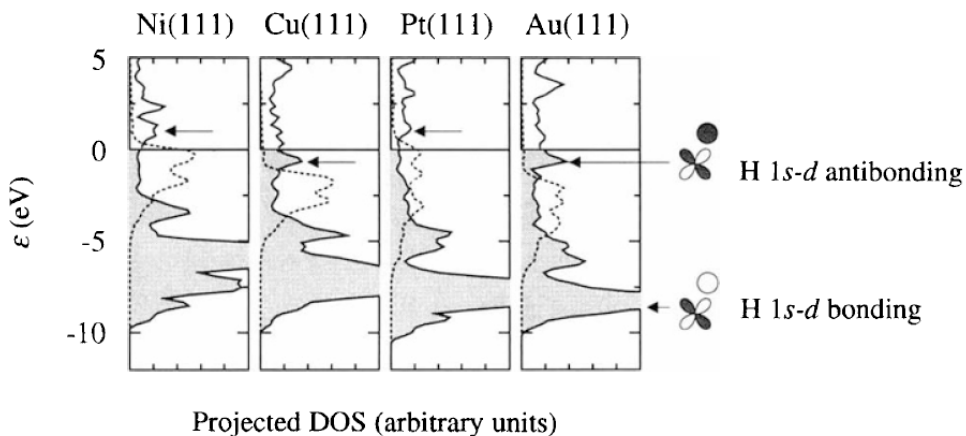


Figure 9: DOS of H interacting with Ni, Cu, Pt and Au (111) surfaces. The solid line indicates the H 1s state and the dashed one the d states of the metal surface. The areas with grey color show that these states are filled. The arrow shows the peak of antibonding states for each DOS [56].

The peaks of DOS close to the Fermi level, in Figure 9, are responsible for their behaviour towards hydrogen. For Cu(111) and Au(111), they are located below Fermi level, suggesting filled antibonding states, so the repulsion is stronger and the bond formation with hydrogen is weaker. In contrast, Ni(111) and Pt(111) have peaks above the Fermi level, so that there are empty states and the bonding with hydrogen is stronger [56].

The d-band model can apply to other surfaces-molecules systems. For example, based on this model the shift of metal d-band energy from the Fermi level is used to explain the hydrogen evolution performance of TMDs edges, such as MoSe<sub>2</sub> and WSe<sub>2</sub> [58]. Thus, we have to consider that the metal d band energy is also a descriptor of the activity of transition metal surfaces [1, 57].

#### 2.4.2 A physical model of MoS<sub>2</sub> basal plane activation

A model for understanding the behaviour of sulphur atoms of MoS<sub>2</sub> basal plane for the HER was proposed recently by M.Liu et al [55]. Due to the fact that sulphur atoms of MoS<sub>2</sub> basal plane have full valence shells, they are not able to bind hydrogen. However, the transition metal doping can activate the basal plane to bind hydrogen [22, 52-54]. The activation of the basal plane can be achieved with the partial opening of the valence shell of the electronic state of S atom. Then, it is able to bond with a hydrogen atom.

They propose a theoretical model of a two step process. As it is described in Figure 10(a), in the first step, we have the electron transfer from a S atom of the basal plane to the surrounding metals. In the second step, a hydrogen atom binds with the sulphur atom to fill the open cell.

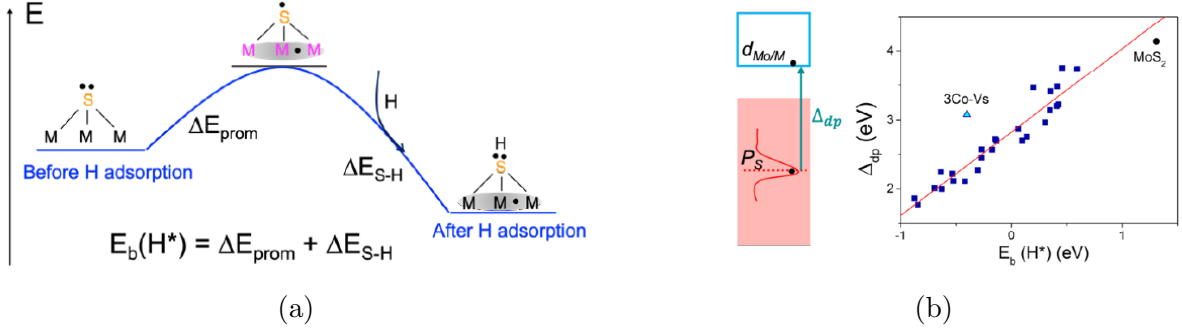


Figure 10: (a) Physical model of H-S bond formation. (b) (Left) The interband distance,  $\Delta_{dp}$  between the S-p and M-d states. (Right) Linear relationship between  $\Delta_{dp}$  and  $E_b(H^*)$  adapted from [55].

Because the first step is an endothermic reaction, it requires energy to promote S into an open state valence shell. This energy is denoted as  $\Delta E_{prom}$ . Then, the formation of H-S is an exothermic reaction, so energy  $\Delta E_{S-H}$  is produced. The sum of these two energies is the H-S binding energy  $E_b(H^*)$ .

$$E_b(H^*) = \Delta E_{prom} + \Delta E_{S-H} \quad (11)$$

To describe the H-S bonding, an electronic structure based descriptor is introduced, the interband distance  $\Delta_{dp}$ . It refers to the distance between occupied S-p states and unoccupied M-d states of the neighbour three metal atoms to sulphur.

$$\Delta_{dp} = \epsilon_d - \epsilon_p = \frac{\int_{E_f}^{1e} \epsilon n_d}{\int_{E_f}^{1e} n_d} - \frac{\int_{-\infty}^{E_f} \epsilon n_p}{\int_{-\infty}^{E_f} n_p} \quad (12)$$

where  $\epsilon_p$  is the p-band center and it is integrated from the occupied p band to the Fermi level. The  $\epsilon_d$  is the d-band center for the neighbour M-d states integrated over unoccupied d orbitals, from  $E_f$  to the state where one extra electron is added.

From DFT calculations on many different systems with different dopant elements, dopants concentrations and sulphur vacancies, they found a linear relation between  $\Delta_{dp}$  and  $E_b(H^*)$ , as it is depicted in Figure 10(b). The positive slope suggests that the smaller the interband distance (S-p and M-d), the stronger is the binding of hydrogen. Consequently, it can be a guideline for the designing of HER catalytic materials, especially for the transition metal doped and pure TMDs systems for various chalcogen atoms of their basal plane.

## 2.5 DFT in Heterogeneous Catalysis and Future Challenges

The aforementioned chapters present an insight into the important developments of MoS<sub>2</sub> catalysts for Hydrogen Evolution Reaction using theory, and more specifically Density Functional Theory, in the field of Heterogeneous Catalysis. The main strategies for designing efficient catalysts were explored as well as the importance of descriptors and features of an efficient catalyst. In the following paragraphs directions for the future of theoretical calculations based on DFT for heterogeneous catalysis will be discussed.

There are plenty of future challenges for the surface chemistry science to overpass in order to describe the complexity of heterogeneous catalysis reactions. For instance, there is need for examination of more complex reactions and catalysts, inclusion of van der Waal interactions, examination of the electron transfer at the interface of the metal-molecule, studying materials beyond transition metals, overcoming DFT limitations (band gap underestimation and excited electronic states), achieving higher computational accuracy and performance through the development of better codes and methods, development of descriptors that demand fewer information about the studied systems and description of electrocatalytic and photocatalytic processes [1,2].

Methods are developed in the pursuit of new efficient catalysts. For example, the creation of alloys, such as BiPt mentioned before [1,4]. With the help of volcano relationships between the descriptors and the rate of the reaction, a prediction on a possible efficient combination of two metals can be achieved. Another way is the inspiration by nature and especially from the observation of the active centres of enzymes [6]. Finally, the construction of a database with the already studied catalysts can contribute in the design of efficient catalysts [1,2].

The crucial challenge for DFT calculations is the design of catalysts industrial reaction conditions. An example is the ammonia synthesis, where the top of the maximum in its volcano curve is formed by the concentration of ammonia in the reaction environment, so that Fe can be used as catalyst in low concentrations or Ru in high concentrations [1,8].

Combination of Theory and Experiment has crucial importance, as Theory needs to follow and verify the experimental results, but also guide experimental predictions [2]. While computers speed increases with the development of technology, so that the computational methods become less expensive, for experimental methods the trend is to become more expensive with time. Hence, Density Functional Theory calculations will have a fundamental place in the design of catalysts in the future.

## 3 Theoretical and Computational Methods

### 3.1 The Many-Particle Problem and Density Functional Theory

In this study we perform calculations using Density Functional Theory (DFT). To begin with, in order to describe a system, we use the Schrödinger equation :

$$\hat{H}\Psi = E\Psi \quad (13)$$

where,  $\hat{H}$  is the Hamiltonian operator,  $\Psi$  is the wavefunction and  $E$  is the energy of the system. For a many-particle system, where electrons interact with nuclei, the Hamiltonian is:

$$\begin{aligned} \hat{H} &= \hat{T}_e + \hat{T}_n + \hat{V}_{n-n} + \hat{V}_{e-e} + \hat{V}_{n-e} \\ &= \sum_A \left( \frac{-\hbar^2 \nabla_A^2}{2M_A} \right) + \sum_i \left( \frac{-\hbar^2 \nabla_i^2}{2m_i} \right) + \frac{1}{2} \frac{1}{4\pi\epsilon_o} \sum_{A \neq B} \frac{e^2 Z_A Z_B}{|\vec{R}_A - \vec{R}_B|} + \frac{1}{2} \frac{1}{4\pi\epsilon_o} \sum_{i \neq j} \frac{e^2}{|\vec{r}_i - \vec{r}_j|} - \frac{1}{4\pi\epsilon_o} \sum_{i,A} \frac{e(eZ_A)}{|\vec{r}_i - \vec{R}_A|} \end{aligned}$$

It consists of the kinetic energy of electrons ( $\hat{T}_e$ ), the kinetic energy of nuclei ( $\hat{T}_n$ ), the Coulomb interaction between nuclei ( $\hat{V}_{n-n}$ ), the Coulomb interaction between electrons ( $\hat{V}_{e-e}$ ) and the Coulomb interaction between electrons and nuclei ( $\hat{V}_{n-e}$ ). As we see this expression is quite complex. The Schrödinger Equation can be solved exactly for hydrogen atom and with some approximation for systems with a small number of electrons. However, limits appear for a many-particle system's solution [60, 66].

#### 3.1.1 Born-Oppenheimer approximation

The Born-Oppenheimer approximation or the adiabatic principle suggests that an object with great mass, moves slower than the one with smaller mass and its motion can be neglected. For the case of many-particle system, nuclei are moving slower than electrons ( $m_p \approx 1800 m_e$ ), so we can neglect their contribution on the kinetic energy term ( $\hat{T}_n$ ). Also, the positions of the nuclei are considered fixed compare to electrons position, so that the term of Coulomb interaction between nuclei is a constant. Consequently, the variables of the many-particle problem is reduced and we obtain a simplified Hamiltonian [60-63,65]:

$$\hat{H} = \sum_i \left( \frac{-\hbar^2 \nabla_i^2}{2m_i} \right) + \frac{1}{2} \frac{1}{4\pi\epsilon_o} \sum_{A \neq B} \frac{e^2 Z_A Z_B}{|\vec{R}_A - \vec{R}_B|} + \frac{1}{2} \frac{1}{4\pi\epsilon_o} \sum_{i \neq j} \frac{e^2}{|\vec{r}_i - \vec{r}_j|} - \frac{1}{4\pi\epsilon_o} \sum_{i,A} \frac{e(eZ_A)}{|\vec{r}_i - \vec{R}_A|} \quad (14)$$

### 3.1.2 External potential

At this point, we have to consider the parameters that distinguish a system from another. The number of electrons is an important factor. However, considering that many systems can have the same number of electrons and be different, for example H and  $\text{Li}^{2+}$ , we need another determinant factor. The position and kind of nucleus have equal importance. In Hamiltonian expression above, the kinetic energy of electron (first term), the Coulomb interaction between electrons (third term) and the Coulomb interaction between electrons and nuclei (last term) have information about the number of electrons. The Coulomb interaction between nuclei (second term) and the Coulomb interaction between electrons and nuclei refer to the positions ( $R_A$ ) and kind of nuclei ( $eZ_A$ ). However, the last term ( $V_{e-n}$ ) encloses both factors, so that it defines the energy of N electrons in an electric potential provided by a given amount of nuclei at position  $R_A$  [65].

The external potential is defined as the electric potential generated from this amount of nuclei:

$$V_{ext} = \frac{1}{4\pi\epsilon_0} \sum_A \frac{eZ_A}{|\vec{r}_i - \vec{R}_A|} \quad (15)$$

We use the term external, because from the electrons point of view is an applied potential. It defines the system that we study, as it is unique for each system in nature [60-63, 65].

### 3.1.3 Electron density of the ground state

Another key parameter for Density Functional Theory is the electron density of a system :

$$\hat{\rho} = \sum_{i=1}^N \delta(\vec{r} - \vec{r}_i) \quad (16)$$

It gives the probability to find any electron at space  $\vec{r}$ . It is independent from the amount and positions of the other electrons of the system [60-63, 65].

$$\rho = \langle \Psi | \hat{\rho} | \Psi \rangle = \sum_{i=1}^N |\Psi|^2 \quad (17)$$

### 3.1.4 First Hohenberg-Kohn theorem

The Hohenberg-Kohn (HK) Theorems are the fundamentals of the Density Functional Theory. According to the first Hohenberg-Kohn Theorem: *“For any system of interacting particles in an external potential  $V_{ext}(\vec{r})$ , the potential  $V_{ext}(\vec{r})$  is determined uniquely, except for a constant, by the ground state particle density  $\rho_0(\vec{r})$  [60, 62].”* This means that there is one to one correspondence between the ground state electron density of a many-particle system and the external potential [60-63, 65].

The electron density of the ground state is as important as the wavefunction of a system. Despite being mathematically a less complicated object, it contains the same information about the system as the wavefunction. The first HK theorem achieves to eradicate the number of variables. For example, in order to describe a N electron system, by using  $\rho_0(\vec{r})$  which depends only on the three spatial variables and not on the number of electrons, it needs only 3 variables, instead of using the wavefunction that requires 3N variables [60-63, 65].

Another consequence of this theorem is : *“Therefore all properties of the system are completely determined given only the ground state density  $\rho_0(\vec{r})$  [60, 62].”* So for a many-particle system, any property ( $\mathcal{O}$ ) can be expressed as a unique function of its ground state electron density.

$$\mathcal{O}[\rho_0(\vec{r})] = \langle \Psi(\rho_0(\vec{r})) | \mathcal{O} | \Psi(\rho_0(\vec{r})) \rangle \quad (18)$$

### 3.1.5 Second Hohenberg-Kohn theorem

The Second Hohenberg-Kohn Theorem states: *“A universal functional for the energy  $E[\rho]$  in terms of the density  $\rho$  can be defined, valid for any external potential  $V_{ext}(\vec{r})$ . For any particular  $V_{ext}(\vec{r})$ , the exact ground state energy of the system is the global minimum value of this functional, and the density that minimizes the functional is the exact ground state density  $\rho_0$  [60, 62].”* This theorem uses a constrained search method to minimize the total energy functional, in order to derive the correct ground state density [60].

$$E_{V_{ext}}[\rho] = \min_a (\Psi_\rho^\alpha, H \Psi_\rho^\alpha) = F_{HK}[\rho] + \int \rho(\vec{r}) V_{ext}(\vec{r}) d\vec{r} \quad (19)$$

where  $\Psi_\rho^\alpha$  is a trial function for the specific  $\rho(\vec{r})$  and the  $F_{HK}[\rho]$  is a functional that contains the kinetic and electron-electron interaction part of the total energy. The functional for the energy  $E_{V_{ext}}[\rho]$  is sufficient to describe the exact ground state energy and density. However, it implies a limitation for the excited states of the electrons, so that other means should be employed to describe them [60, 62].

### 3.1.6 The Kohn-Sham equation

Despite the simplifications that we mentioned above, the solution of the many-particle system is still a demanding task. For this reason, the Kohn–Sham approach uses an auxiliary system instead of the complicated many-body system. It is an ansatz, as there are no guidelines for selecting a simpler auxiliary system [62, 64].

The ansatz of Kohn and Sham suggests that the ground state density  $\rho_0(\vec{r})$  of the initial many-body system is similar to that of a selected non-interacting system. Hence, we obtain independent-particle equations for the non-interacting system that can be considered exactly soluble with all the complicated many-particle terms involved into an exchange–correlation

functional of the density. The solution accuracy is only restricted by the exchange-correlation functional [62, 64].

Consequently, given the ground state of a N-electron system :

$$\rho(\vec{r}) = \sum_{i=1} \phi_i^*(\vec{r})\phi_i(\vec{r}) \quad (20)$$

where  $\phi_i$  is the single-particle wave function for the N lowest energy solutions of the Kohn-Sham equation:

$$\hat{H}_{KS}\phi_i = \epsilon_i\phi_i \quad (21)$$

where the Kohn-Sham Hamiltonian is:

$$\hat{H}_{KS} = \hat{T} + \hat{V}_H + \hat{V}_{ext} + \hat{V}_{xc} = -\frac{\hbar\nabla_i^2}{2m} + \frac{e^2}{4\pi\epsilon} \int \frac{\rho(\vec{r}')}{|\vec{r} - \vec{r}'|} d\vec{r}' + \hat{V}_{ext} + \hat{V}_{xc} \quad (22)$$

The second term in the relationship above, the Hartree potential ( $\hat{V}_H$ ) expresses the Coulomb energy of the particle of the Kohn-Sham equation in the potential generated by the other particles of the system expressed through a total electron density. This term includes the self-interaction contribution due to the fact that the electron of the Kohn-Sham equation belongs also to the electron density [60-65].

The last term is the exchange correlation energy ( $\hat{V}_{xc}$ ). It is defined as a functional derivative of the exchange correlation functional.

$$\hat{V}_{xc} = \frac{\delta V_{xc}[\rho]}{\delta \rho} \quad (23)$$

Considering the above, the Schrödinger equation for a many-particle problem, with interacting electrons in an external ion potential, transforms to a non-interacting electrons problem with its electrons moving in an effective potential [67]. From relationship (22), we have two major contributions. The one has the terms that are easy to handle and known, such as kinetic energies ( $\hat{T}$ ), potential energies ( $\hat{V}_H$ ) and Coulomb interaction energies ( $\hat{V}_{ext}$ ). However, the other term, the exchange-correlation energy ( $\hat{V}_{xc}$ ) is sophisticated enclosing all the many-particle and quantum effects [66].

A (simplified) algorithm is implemented in order to obtain the solution of the Kohn-Sham equations [61]:

1. Define an initial density  $\rho(\vec{r})$ .
2. Find  $\phi_i(\vec{r})$  from the solution of Kohn-Sham equation.

3. Find a new electron density  $\rho_{KS}(\vec{r})$  from the previous wavefunction.
4. Compare  $\rho(\vec{r})$  and  $\rho_{KS}(\vec{r})$ . If they are equal, this is the ground state density. Otherwise, the process starts from step 2.

From this procedure the solution of the Kohn–Sham equations derives in a self-consistent way.

## 3.2 Exchange-Correlation Functionals

DFT ensures the existence of the exchange correlation functional  $V_{xc}[\rho]$ . However, its exact form is unknown. It should be an extremely complicated functional, so that it can explain all the chemistry and solid state physics. For this reason, we use approximations such as the Local Density Approximation (LDA) and Generalized Gradient Approximation (GGA-PBE).

### 3.2.1 Local Density Approximation

The Local Density Approximation (LDA) is an approximation for the exchange correlation energy functional that assumes that the XC energy at each point of space equals to the XC energy of the homogeneous system of density  $\rho$ ,  $\epsilon_{xc}(\rho)$ , so that:

$$E_{xc}^{LDA}[\rho] = \int \rho(\vec{r}) \epsilon_{xc}^{gas}(\rho(\vec{r})) d^3r \quad (24)$$

$\epsilon_{xc}^{gas}$  is the exchange correlation energy per particle of a homogeneous electron gas with electron density of  $\rho(\vec{r})$  [67]. It employs only the electron density and it is efficient both for homogeneous electron gas and inhomogeneous systems [66, 67].

### 3.2.2 Generalized Gradient Approximation

Generalized Gradient Approximation (GGA) functional was developed later. It includes non-local effects and uses the gradient of the electron density for estimating a point’s contribution to the total exchange-correlation energy [64].

$$E_{xc}^{GGA}[\rho] = \int \rho(\vec{r}) \epsilon_{xc}^{GGA}(\rho, \nabla\rho) d^3r \quad (25)$$

The GGA functionals are more accurate for molecular systems [64].

Finally, PBE (Perdew–Burke–Ernzerhof) is a numerical approach to the general gradient approximation in which the exchange correlation energy is:

$$E_{xc}^{GGA-PBE}[\rho] = \int \rho(\vec{r}) \epsilon_{xc}^{unif} F_{xc}(\vec{r}_s, s) d^3r \quad (26)$$

where,  $\vec{r}_s$  is the Seitz radius  $\rho^{-1} = \frac{3}{4}\pi r_s^3$ ,  $s = \frac{\nabla\rho}{2\kappa_F\rho}$  is the dimensional density gradient with  $\kappa_F = (3\pi^2\rho)^{1/3}$  and  $F_{xc}$  is an enhancement factor.

In order to develop improved functionals, two methods are used, the “Jacob’s ladder” and the development of hybrid functionals. The idea behind “Jacob’s ladder” is to maintain the functionals that work and try to enhance them. It is called a ladder because it consist of five steps-rungs that lead to the “divine” functional. The LDA is in the fist rung, because it employs only the electron density. The GGA functionals belong to the second rung and utilize the electron density and the gradient of electron density. Next, there are meta-GGAS, where the scientific community is currently working on. They also use the kinetic energy density. Then, there are functionals that treat exchange exactly and try to enhance correlation. The divine functional at the fifth step should have the exact exchange and correlation. The second method includes the use of hybrid functionals, that are constructed from the combination of exact results for the exchange and approximations for the correlation part, from ab initio or empirical sources. For example B3LYP is one of the most frequent used [61, 67].

With the development of materials research, the complexity of the studied systems by DFT increases, so that the selection of a suitable functional is not an easy task. The development of numerical techniques and faster algorithms have contributed to the accuracy of DFT calculations. However, more effort should be put in developing exchange correlation functionals to produce results in an excellent agreement with experiment [66].

### 3.3 The Pseudopotential Method

The single particle wavefunction can be expressed as a sum over basis functions:

$$\phi(\vec{r}) = \sum_{(\alpha=1)} c_{\alpha}^i \chi_{\alpha}^i(\vec{r}) \quad (27)$$

where  $\chi_{\alpha}^i(\vec{r})$  are the basis function and  $c_{\alpha}^i$  are the coefficients that we search and describe the system. The difference between the original function and the basis functions is important. If there is large deviation between them, more basis functions are required to describe the system. However, there is a limit to the number of the basis functions as the calculations become time consuming .

Figure 11 illustrates with blue color the wavefunction of a nucleus. The  $r_c$  is the cutoff radius. As we observe, close to nucleus ( $r < r_c$ ) the wavefunction oscillates rapidly with a  $Z/r$  dependence. Moving away from the nucleus region ( $r > r_c$ ), the wavefunction becomes smoother.

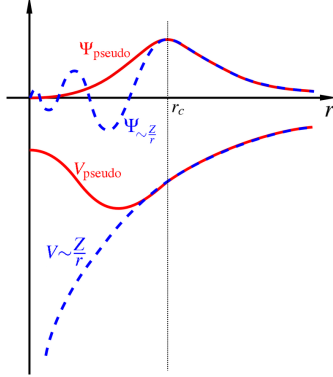


Figure 11: Wavefunction and potential of the nucleus (blue color) and in the pseudopotential method (red color) [68].

We use various numerical solution techniques, such as all-electron and pseudopotential methods to introduce a limited number of suitable basis functions that describe the system. All-electron method employs basis functions that look similar to the expected result. For pseudopotential methods, the basis set describes the wavefunction better in areas of interest.

Hence, all the interesting chemical properties derive from the valence electrons located in the region away from the nucleus, we use the pseudopotential method. It approximates the original wavefunction with another one, shown with red color in Figure 11, that close to the nucleus is smooth and loses in details, but away from it is identical to the wavefunction.

DFT codes such as VASP and Quantum Espresso are based on pseudopotential method. In this study we use Projector Augmented Wave Method (PAW), which belongs to the Pseudopotential methods, as implemented by VASP [62, 68, 69].

### 3.3.1 Projector augmented wave method

The Projector Augmented Wave Method (PAW) combines pseudopotential and linear augmented-plane-wave methods. It uses a linear transformation :

$$T = 1 + \sum_i (|\phi_i\rangle - |\tilde{\phi}_i\rangle)\langle\tilde{p}_i| \quad (28)$$

where  $|\phi_i\rangle$  are all-electron partial waves, defined inside the sphere of ions, expressing rapid oscillation,  $|\tilde{\phi}_i\rangle$  are pseudo partial waves, defined also inside the ions, but they have smooth wavefunctions and  $\langle\tilde{p}_i|$  are projector functions. The pseudowavefunction  $|\tilde{\Psi}\rangle$  changes to a single-particle Kohn-Sham  $|\Psi\rangle$  wavefunction by the action of the operator:

$$|\Psi\rangle = T|\tilde{\Psi}\rangle \quad (29)$$

The PAW method transforms the rapidly oscillating wavefunctions into smooth wavefunctions, requiring less computational effort for calculating properties of the systems [71].

### 3.4 Plane Wave Energy Cutoff

In crystals there is a periodic arrangement of ions and electrons. The Bloch's Theorem states that the electron wave functions in a crystal have a basis of Bloch wave energy eigenstates [60-73]:

$$\phi_{\vec{k}} = e^{i\vec{k}\cdot\vec{r}} u_{\vec{k}}(\vec{r}) \quad (30)$$

where  $u_{\vec{k}}(\vec{r})$  is a periodic function in space:

$$u_{\vec{k}}(\vec{r}) = \sum_{\vec{G}} c_{\vec{G}} e^{i\vec{G}\cdot\vec{r}} \quad (31)$$

where,  $\vec{G} = m_1 \vec{b}_1 + m_2 \vec{b}_2 + m_3 \vec{b}_3$ , with  $m_i$  an integer number. Considering that  $\vec{a}_i$  are real space lattice vectors, the  $\vec{G}$  is chosen, so that  $\vec{G} \cdot \vec{a}_1 = 2\pi m_1$ . Now combining (30) and (31) into the relationship below:

$$\phi_{\vec{k}}(\vec{r}) = \sum_{\vec{G}} c_{\vec{G}+\vec{k}} e^{i(\vec{G}+\vec{k})\cdot\vec{r}} \quad (32)$$

The sum in relationship (32) indicates that for every  $\vec{k}$  there is an infinite number of possible  $\vec{G}$  values. Considering that wavefunctions  $\phi_{\vec{k}}(\vec{r})$  are solutions of the Schrödinger equation, their kinetic energies are :

$$E = \frac{\hbar^2}{2m} |\vec{k} + \vec{G}|^2 \quad (33)$$

As we understand the DFT calculations in the  $\vec{k}$ -space makes it a demanding task. Considering that the solutions with lower energies have greater physical importance than the ones with higher energies, a truncation of the infinite sum can be made, so that an energy cutoff is defined:

$$E_{cut} = \frac{\hbar^2}{2m} \vec{G}_{cut}^2 \quad (34)$$

and the equation (32) changes to:

$$\phi_{\vec{k}}(\vec{r}) = \sum_{|\vec{G}+\vec{k}| < \vec{G}_{cut}} c_{\vec{k}+\vec{G}} e^{i(\vec{k}+\vec{G})\cdot\vec{r}} \quad (35)$$

### 3.5 K-point Grid

The Bloch's Theorem suggests that an electron wavefunction can be expressed as a basis of plane waves (equation (30)), so it is possible to solve the Schrödinger equation for each  $k$  independently.

We refer to plane waves calculations, because the  $e^{(i\vec{k}\cdot\vec{r})}$  is a plane wave term. The space vector  $\vec{r}$  is in the real space with lattice vectors  $\vec{a}_i$ , while  $\vec{k}$  belongs to the reciprocal space. Reciprocal lattice vectors  $\vec{b}_j$  are defined to fulfil the relationship :

$$\vec{a}_i \cdot \vec{b}_j = \begin{cases} 2\pi, & i = j \\ 0, & i \neq j \end{cases} \quad (36)$$

So that the reciprocal lattice vectors are:

$$\vec{b}_1 = 2\pi \frac{\vec{a}_2 \times \vec{a}_3}{\vec{a}_1 \cdot (\vec{a}_2 \times \vec{a}_3)}, \quad \vec{b}_2 = 2\pi \frac{\vec{a}_3 \times \vec{a}_1}{\vec{a}_2 \cdot (\vec{a}_3 \times \vec{a}_1)}, \quad \vec{b}_3 = 2\pi \frac{\vec{a}_1 \times \vec{a}_2}{\vec{a}_3 \cdot (\vec{a}_1 \times \vec{a}_2)} \quad (37)$$

The primitive cell in the reciprocal space is called the Brillouin zone. It is important, because it has significant symmetry points in space, such as  $\Gamma$ -point that refers to  $\vec{k} = 0$  and are used for electronic band structure of materials.

The DFT calculations involve integration in a large area of  $k$ -points. For less computational expensive calculations, a  $k$ -point grid needs to be selected. If the supercell has the same dimensions in each direction in the real space, so it has in the reciprocal space, the number of  $k$ -points should be equal for every direction. For this reason, we use a  $k$ -point grid ( $N \times N \times N$ ) that contains a sufficient amount of  $k$ -points  $N^3$  for energy convergence. Symmetries in the crystal benefit the calculations, as their integrals can be calculated exactly in a smaller area of the Brillouin zone. This region is referred as the irreducible Brillouin zone and minimizes the number of  $k$ -points in a great degree [60-63].

### 3.6 Computational Parameters

All the calculations of this study were performed using Density Functional Theory implemented with Vienna *Ab initio* Simulation Package (VASP) [72-75]. The Projector Augmented Wave method (PAW) [71, 76, 77] with Perdew-Burke-Ernzerhof (PBE) [78] exchange correlation functional was used. Performing convergence tests, a plane wave energy cutoff of 500 eV and a  $\Gamma$ -centered 9x9x3 Monkhorst-Pack k-point mesh were selected for sampling the Brillouin zone. Atoms of the structure were relaxed using a conjugate-gradient method. A vacuum of at least 12 Å was used in the z direction to avoid interlayer interactions.

A MoS<sub>2</sub> primitive cell was used as a guideline for ab initio calculations. We performed calculation with LDA and PBE functionals and compare the energy and structural parameters with other computational works and found that they are in agreement. Comparing them with experimental data, we conclude that PBE describes better the interatomic distances. Then, we construct and study monolayer MoS<sub>2</sub> 3x3 supercell consisted of 9 Mo and 18 S atoms.

We study the pristine MoS<sub>2</sub> basal plane as a reference system for hydrogen adsorption ability. Then, on the geometry optimized monolayer MoS<sub>2</sub>, we introduce modifications on the basal plane, such as sulphur vacancy ( $V_S$ ) and Mo substitution with a Ni dopant. The combination of Ni-dopant and with a sulphur vacancy system (Ni-MoS<sub>2</sub>- $V_S$ ) was also examined, with the Mo atom neighbour to the  $V_S$  substituted by Ni. Finally, we examine the hydrogen evolution efficiency of several Transition Metal-doped, with a sulphur vacancy, systems.

## 4 Theoretical Study of Ni-MoS<sub>2</sub>-V<sub>S</sub>

### 4.1 MoS<sub>2</sub> Primitive Cell Convergence Calculations

We perform calculations on energy and structural parameters on primitive cell of MoS<sub>2</sub>. Results for LDA and PBE exchange correlation functionals were produced and compared in order to have the most appropriate functional for our study.

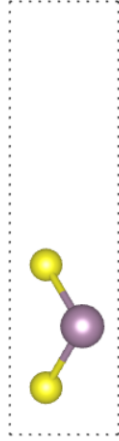


Figure 12: Primitive cell of MoS<sub>2</sub> consists of one Mo and two S atoms.

MoS<sub>2</sub> belongs to space group P6<sub>3</sub>/mmc, so that its primitive vectors are :

$$\mathbf{a}_1 = -\frac{1}{\sqrt{2}}ax + \frac{\sqrt{3}}{2}ay \quad (38)$$

$$\mathbf{a}_2 = ax \quad (39)$$

$$\mathbf{a}_3 = cz \quad (40)$$

where a is the lattice parameter and c is the hexagonal lattice parameter. Its basis set is :

$$\mathbf{b}_1 = \frac{1}{3}\mathbf{a}_1 + \frac{2}{3}\mathbf{a}_2 + \frac{1}{4}\mathbf{a}_3 \quad (41)$$

$$\mathbf{b}_2 = \frac{2}{3}\mathbf{a}_1 + \frac{1}{3}\mathbf{a}_2 + (1 - u)\mathbf{a}_3 \quad (42)$$

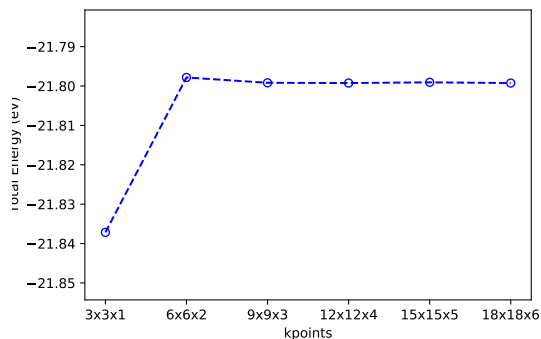
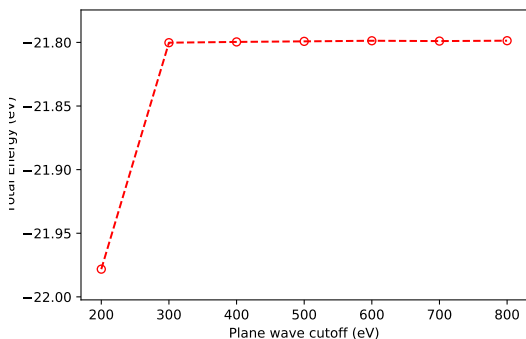
$$\mathbf{b}_3 = \frac{2}{3}\mathbf{a}_1 + \frac{1}{3}\mathbf{a}_2 + (u - \frac{1}{2})\mathbf{a}_3 \quad (43)$$

where u is an internal parameter, so that the half of distance between two sulphur atoms perpendicular to Mo plane is equal to  $d_{S-S}/2 = (3/4 - u)c$ .

Table 1 and Figure 13 show the calculations on convergence for MoS<sub>2</sub> primitive cell, when PBE exchange correlation functional is used. From the energy convergence calculations on plane wave energy cutoff, a  $\Gamma$ -center 9x9x3 kpoint-mesh was used, so the energy cutoff was found to be 500 eV. Then, using this value, we perform calculations for the kpoint-mesh and we found that 9x9x3 kpoint-mesh describes better the system.

Table 1: Results on the total energy for various plane wave energy cutoffs and kpoint mesh for MoS<sub>2</sub> primitive cell, with PBE functional.

Plane Wave Energy Cutoff (eV)	Energy (eV)	kpoint-mesh (NxNxN)	Energy (eV)
200	-21.97	3x3x1	-21.837
300	-21.800	6x6x2	-21.799
400	-21.800	9x9x3	-21.799
500	-21.799	12x12x4	-21.799
600	-21.799	15x15x5	-21.799
700	-21.799	18x18x6	-21.799
800	-21.799		



(a) Total energy versus plane wave energy cutoff for MoS<sub>2</sub>. (b) Total energy versus different kpoint-mesh for MoS<sub>2</sub> primitive cell.

Figure 13: Energy convergence calculations for MoS<sub>2</sub> using the primitive cell, with PBE as exchange correlation functional.

Hence, for the rest of the calculations for PBE, we used a 9x9x3 kpoint point mesh and a 500 eV plane wave energy cutoff. All the atoms of the structure were relaxed using a conjugate-gradient method.

The total density of states (TDOS) and the band structures are derived from the calculations. In Figure 14(a) the TDOS shows a band gap suggesting that MoS<sub>2</sub> is a semiconductor. The band structure is also in agreement with this result, with a direct band gap at K high

symmetry point, where the maximum of the valence band is located directly down from the minimum of the conduction band.

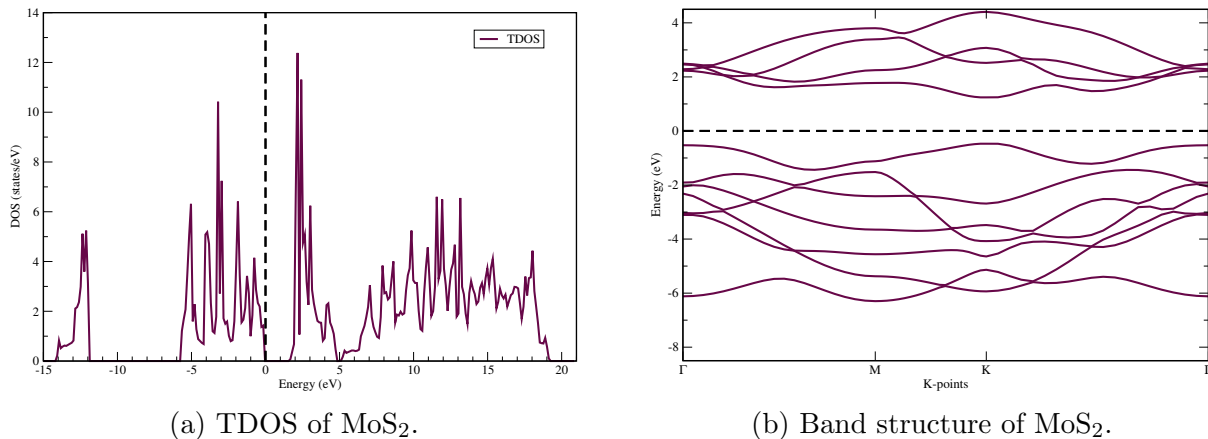
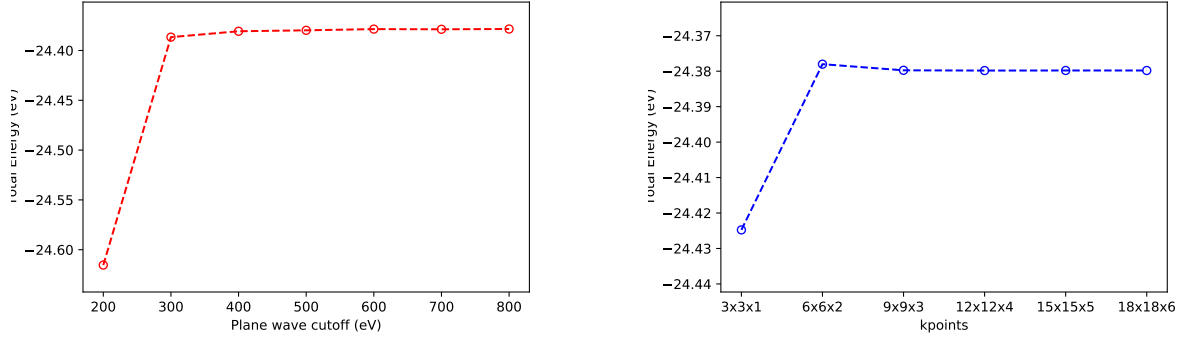


Figure 14: Electronic structure of MoS<sub>2</sub> calculating using the primitive cell with PBE exchange correlation functional.

In a similar way, we perform calculations using LDA exchange correlation functional on MoS<sub>2</sub> primitive cell. Initially, a 9x9x3 kpoint-mesh was employed for energy convergence of plane wave energy cutoff. After finding that energy converges at energy cutoff of 500 eV, we used it to examine the energy convergence of kpoint-mesh. It was found to be 9x9x3 kpoint-mesh.

Table 2: Results on the total energy for various plane wave energy cutoffs and kpoint mesh for MoS<sub>2</sub> primitive cell with LDA functional.

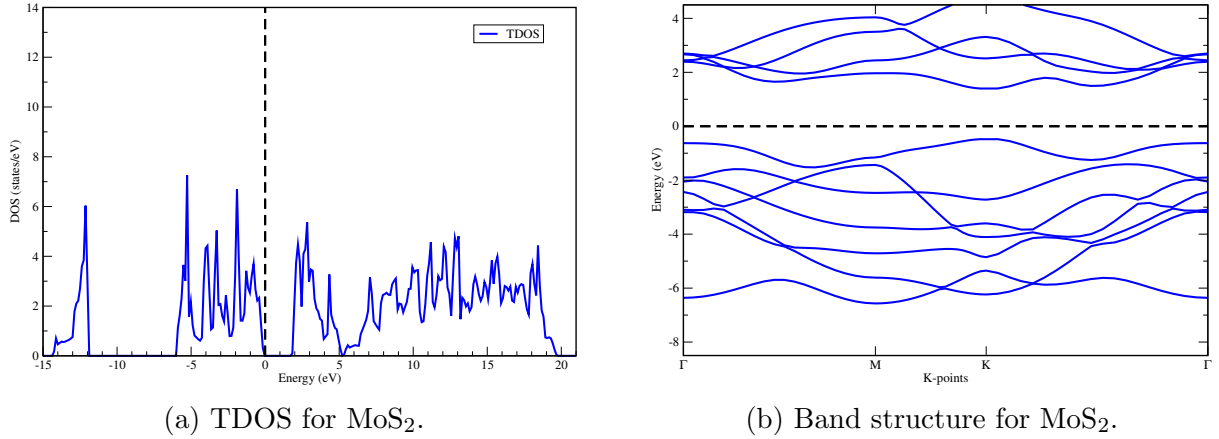
Plane Wave Energy Cutoff (eV)	Energy (eV)	kpoint-mesh (NxNxN)	Energy (eV)
200	-24.615	3x3x1	-24.425
300	-24.387	6x6x2	-24.378
400	-24.381	9x9x3	-24.380
500	-24.379	12x12x4	-24.380
600	-24.379	15x15x5	-24.380
700	-21.379	18x18x6	-24.380
800	-21.379		



(a) Total energy versus plane wave energy cutoff (b) Total energy versus kpoint-mesh for MoS<sub>2</sub>.  
for MoS<sub>2</sub>.

Figure 15: Energy convergence calculations on MoS<sub>2</sub> primitive cell

The TDOS and Band structure for LDA functional are depicted below. According to Figure 16(a) there is a band gap in accordance with the band structure (Figure 16(b)) that shows a direct band gap at K point. Both PBE and LDA electronic structures suggest that single layer MoS<sub>2</sub> is a direct band gap semiconductor.



(a) TDOS for MoS<sub>2</sub>.

(b) Band structure for MoS<sub>2</sub>.

Figure 16: Electronic structure of MoS<sub>2</sub> primitive cell with LDA exchange correlation functional.

Finally, the structural parameters of MoS<sub>2</sub> primitive cell for PBE and LDA calculations were obtained. According to Table 3, the lattice parameter ( $a$ ), the distance between Mo and S ( $d_{Mo-S}$ ), the S-Mo-S angle ( $\theta_{S-Mo-S}$ ), the distance between two sulphur atoms ( $d_{S-S}$ ) and the electronic band gap ( $E_g$ ) were derived from the calculations and compared with experimental results and other theoretical works.

Table 3: Structural parameters of MoS<sub>2</sub> primitive cell, calculated with LDA and PBE exchange correlation functionals. A comparison with other theoretical and experimental works was applied.

	current work		experimental values	theoretical works	
	LDA	PBE		LDA	PBE
a (Å)	3.12	3.18	3.16[79]	3.13[81],[82],[83] 3.12[31]	3.19[31] 3.20[84] 3.23[82]
d <sub>Mo-S</sub> (Å)	2.38	2.41	2.41[79]	2.39[81],[83]	2.45[81]
θ <sub>S-Mo-S</sub> (°)	81.50	80.97	81.30[79]	81.73[81]	80.88[81]
d <sub>S-S</sub>	3.11	3.13	3.19[79]	3.13[81],[83]	3.18[81],[83]
E <sub>g</sub>	1.87	1.61	1.80[80]	1.89[81],[82],[83]	1.69[84] 1.55[81]

All the parameters are in agreement with the experimental data for 3D MoS<sub>2</sub>. PBE describes better the interatomic distances of the system. Comparing these results with other theoretical works, we see that our LDA structural parameter values are consistent with other LDA theoretical works. The same applies for PBE functional.

In regard to the band gap, considering that the experimental value is the optical band gap and not the fundamental, it has a lower value. Both functionals have values close to the experimental, but both underestimate this parameter. In order to obtain an accurate value of the band gap, other methods involving hybrid functionals or GW approximation need to be employed, but these are not in the scope of this work. Also, other theoretical works employing LDA and PBE have similar values to our results for each functional used.

From the above results, we conclude that PBE exchange correlation functional, while it underestimates the band gap, it describes better the structural parameters of MoS<sub>2</sub> primitive cell and will be used for all the calculations in this study.

## 4.2 Hydrogen Adsorption on MoS<sub>2</sub> monolayer

Considering the results for the primitive cell, we continue our calculations for a 3x3 supercell MoS<sub>2</sub> monolayer (Figure 17), by using PBE exchange correlation functional.

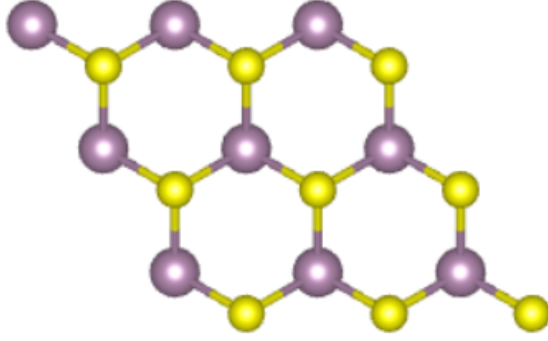


Figure 17: Top view of MoS<sub>2</sub> monolayer 3x3 supercell.

The structural and energetic parameters are presented in Table 4. In respect to the lattice distances, all are in agreement with the previous results on primitive cell. There is a difference in the S-Mo-S angle which is slightly smaller compared to the primitive cell. The optical band gap is in agreement within the error with the one of the primitive cell.

Table 4: Structural and electronic parameters of MoS<sub>2</sub> monolayer.

$a$ (Å)	3.18
$d_{Mo-S}$ (Å)	2.41
$\theta_{S-Mo-S}$ (°)	80.76
$d_{S-S}$ (Å)	3.13
$E_{gap}$ (eV)	1.59

The TDOS and band structure diagrams in Figure 18 are in agreement with the ones of the primitive cell. There is also a band gap in the TDOS (Figure 18(a)). However, the band structure (Figure 18(b)) is folded due to the dimensions of the supercell and we cannot identify the direct band gap in K high symmetry point. The absence of states between the valence and conduction band is consistent with the band gap in TDOS diagram.

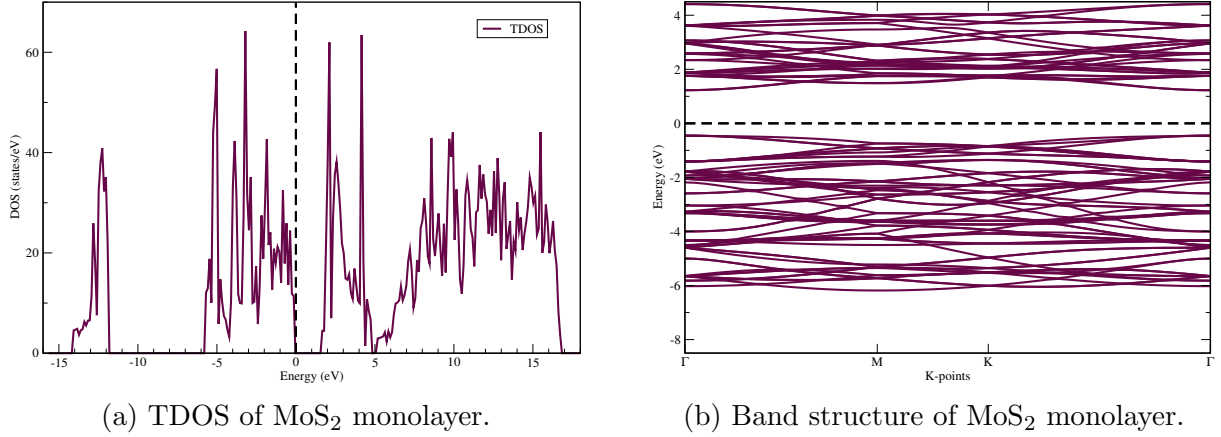


Figure 18: Electronic structure of MoS<sub>2</sub> monolayer

At this point, we investigate the hydrogen adsorption ability of the MoS<sub>2</sub> monolayer. We introduce a hydrogen atom in a distance of 1 Å above a sulphur atom of its basal plane. After geometry optimization calculations, we observe that hydrogen has increase its distance from sulphur, so that it is  $d_{H-S} = 1.36$  Å. The MoS<sub>2</sub> is unaffected by hydrogen, as no geometry change between S and Mo atoms occurs in its basal plane (Figure 19).

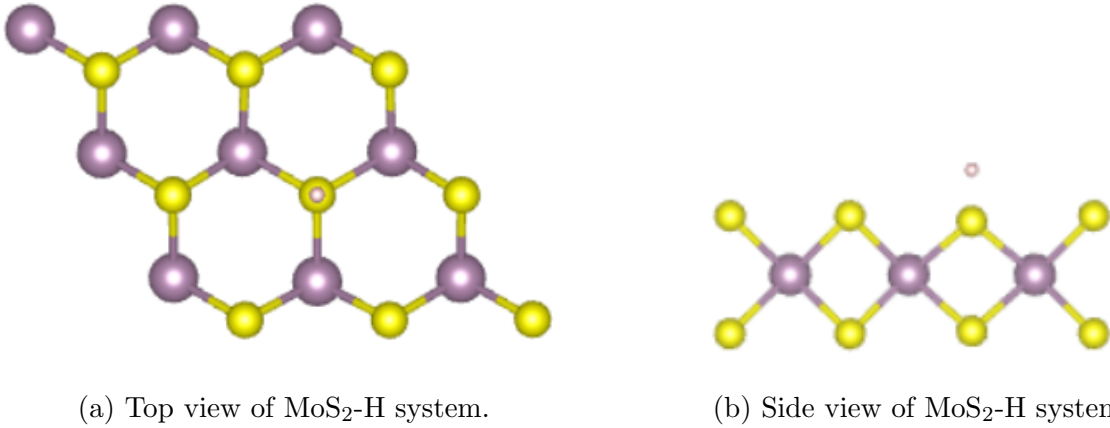


Figure 19: MoS<sub>2</sub>-H system geometry configuration after relaxation of its atoms.

Below, in Figure 20, we present the electronic structure analysis of MoS<sub>2</sub> monolayer with a hydrogen. As we see the Fermi level is located close to the conduction band, so that it behaves as a n-type semiconductor (Figure 20(a)).

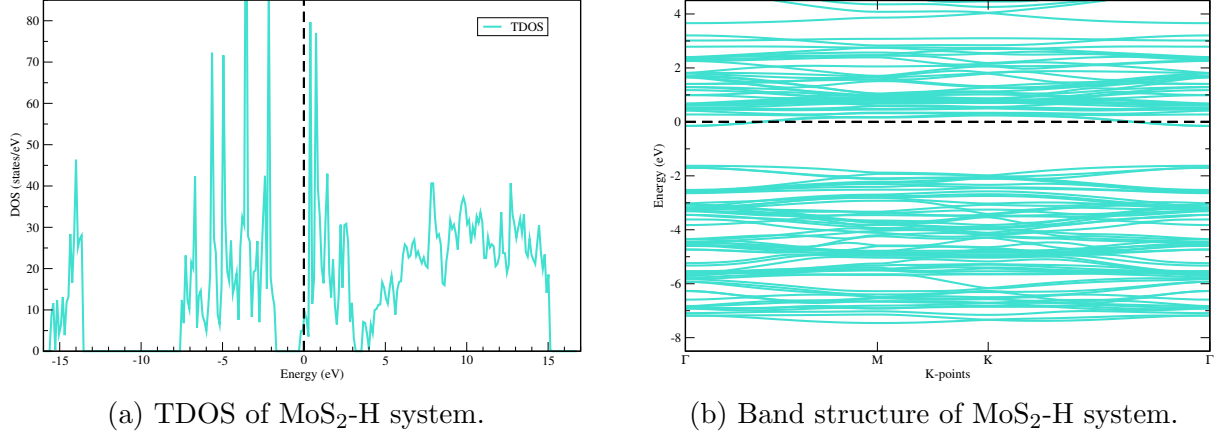


Figure 20: Electronic structure of MoS<sub>2</sub>-H system

By calculating the hydrogen adsorption free energy we obtain  $\Delta G_H$  equal to 2.08 eV (Table 3). This result is in agreement with other theoretical studies that suggest a value from 1.83 eV to 2.00 eV. Because this value is highly positive, MoS<sub>2</sub> basal plane is catalytically inactive for Hydrogen Evolution Reaction.

Table 5: Hydrogen binding energy  $\Delta E_H$  and hydrogen adsorption free energy  $\Delta G_H$  for MoS<sub>2</sub> monolayer.

	current work	other theoretical studies
$\Delta E_H$ (eV)	1.84	
$\Delta G_H$ (eV)	2.08	1.92[59],[25],[10],1.83[52], 2.00[49],[85], 1.88[22]

### 4.3 Hydrogen Adsorption on Ni-MoS<sub>2</sub>

We perform calculations for Ni-MoS<sub>2</sub> system. A Mo atom of its basal plane was substituted with a Ni dopant (Figure 21). After obtaining the geometry optimized structure, we introduce a hydrogen atom in a distance of 1 Å above a sulphur atom next to the Ni dopant.

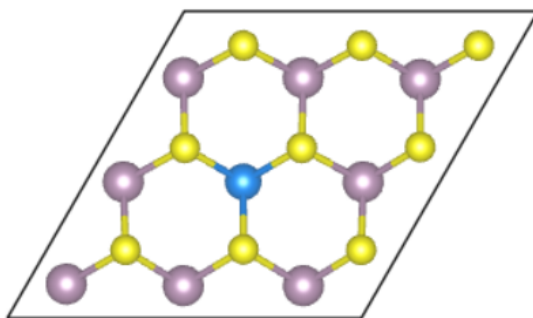


Figure 21: Top view of Ni-MoS<sub>2</sub> monolayer.

Figure 22 shows its geometry configuration after hydrogen adsorption. There is a bond break between Ni dopant and S atom that adsorbs hydrogen. The Ni atom changes position closer to one side. The effect of bond breaking is also discussed in studies [52] and [85]. Although in the first study, Ni has coordination four with its surrounding sulphur atoms, because the Ni-S bond below S adsorption site also breaks, in the second study, this bond remains, so that Ni has five neighbour S atoms, in agreement with our case.

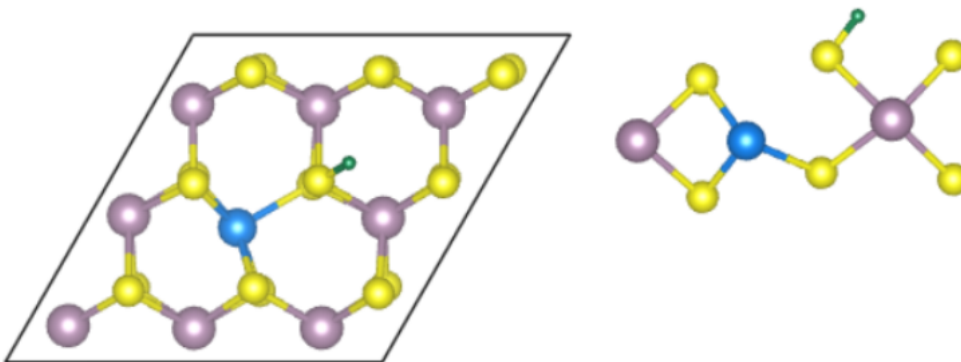


Figure 22: Top and side view of Ni-MoS<sub>2</sub> monolayer.

In the Table 6, the values for hydrogen binding energy and hydrogen adsorption free energy are presented. We find the value of  $-0.86$  eV for  $\Delta G_H$ . It is greater compared to the other two studies. However, we have to consider that they used different geometry configurations (such as 2H-MoS<sub>2</sub> with 3-4 slabs substrate) and computational methods. However, all these values suggest a strong interaction with hydrogen and are far from thermoneutral.

Table 6: Hydrogen binding energy  $\Delta E_H$  and hydrogen adsorption free energy  $\Delta G_H$  for Ni-MoS<sub>2</sub> monolayer.

	current work	other theoretical studies
$\Delta E_H$ (eV)	-1.10	
$\Delta G_H$ (eV)	-0.86	-0.28[1], -0.33[2]

We investigate further the Partial Density of States (PDOS) for Ni-MoS<sub>2</sub>. We use the Ni-d orbitals and S-p orbitals for the S atom that adsorbs hydrogen. Figure 23(a) shows the PDOS before hydrogen adsorption. In the Fermi level, there are new states produced mainly by Ni that hybridizes with S atom. There is also hybridization between them in the valence band.

After hydrogen adsorption, in Figure 23(b) there is hybridization with hydrogen and the other atoms, both in valence and conduction band (far from the Fermi level), suggesting a strong interaction.

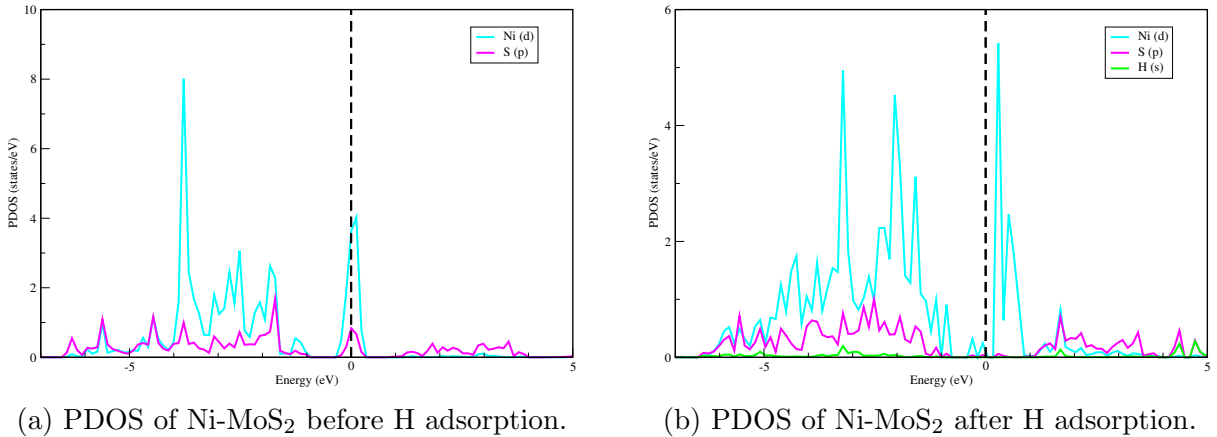


Figure 23: Partial Density of States of Ni-MoS<sub>2</sub> system before and after H adsorption.

#### 4.4 Hydrogen Adsorption on MoS<sub>2</sub>-V<sub>S</sub>

Then, we examine the hydrogen adsorption ability of MoS<sub>2</sub>-V<sub>S</sub> system. A sulphur atom was removed from its basal plane, so that a sulphur vacancy (V<sub>S</sub>) is formed. After geometry optimization, the Mo atom next to the V<sub>S</sub> is located in a similar position as in pristine MoS<sub>2</sub> (Figure 24).

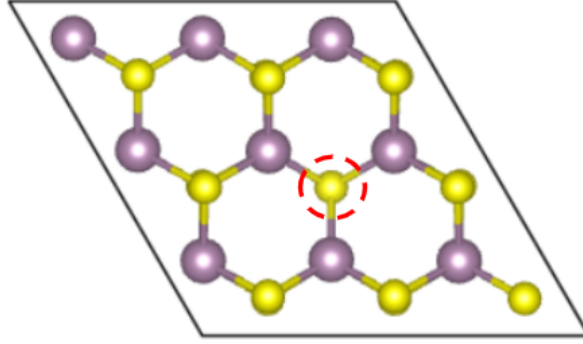


Figure 24: Top view of MoS<sub>2</sub>-V<sub>S</sub> monolayer.

Then, we introduce a hydrogen atom close to the sulphur vacancy. We observe that it stays in a distance above the sulphur atom that is below V<sub>S</sub>. The position of Mo next to V<sub>S</sub> does not change (Figure 25).

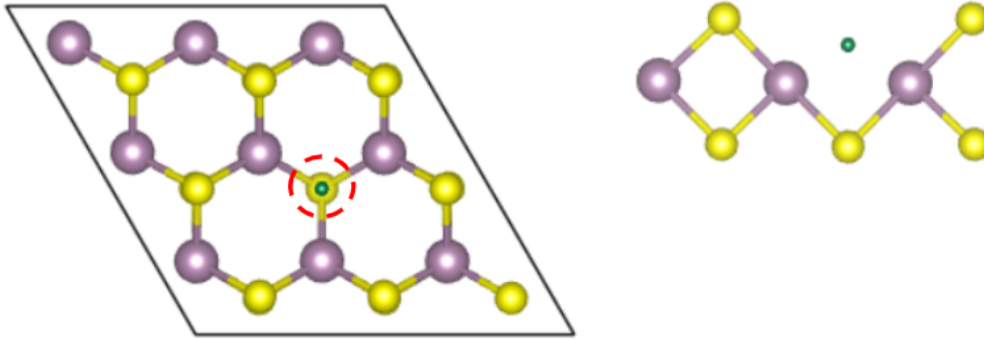


Figure 25: Top and side view of MoS<sub>2</sub>-V<sub>S</sub> monolayer after hydrogen adsorption.

The energies of this structure were also calculated and are presented in Table 7. The  $\Delta G_H$  is equal to 0.059 eV, close to 0, in agreement with other work [49].

Table 7: Hydrogen binding energy  $\Delta E_H$  and hydrogen adsorption free energy  $\Delta G_H$  for MoS<sub>2</sub>-V<sub>S</sub> monolayer.

	current work	other theoretical studies
$\Delta E_H$ (eV)	-0.181	
$\Delta G_H$ (eV)	0.059	0.000 [49]

Finally, we examine the PDOS for this system. As we see in Figure 26(a), before hydrogen adsorption, there is a new state introduced due to the Mo-d orbitals. It is also hybridized in a small degree with S-p orbitals. By introducing hydrogen, Figure 26(b), the state comes close to the Fermi level, and there is a down shift in the valence and conduction band. Hybridization with H is strong far from the Fermi level.

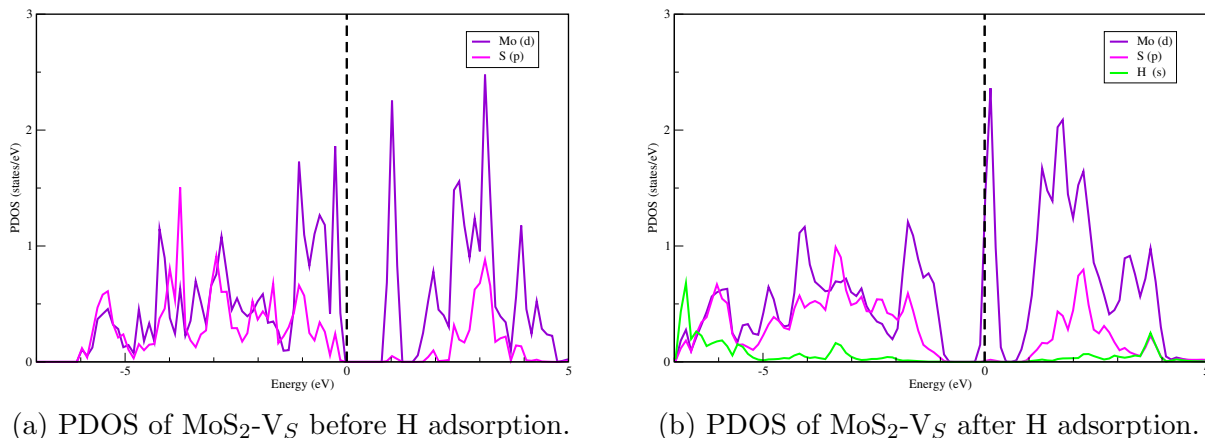


Figure 26: Partial Density of States of MoS<sub>2</sub>-V<sub>S</sub> system before and after H adsorption.

## 4.5 Hydrogen Adsorption on Ni-MoS<sub>2</sub>-V<sub>S</sub>

Then, we examine the hydrogen adsorption ability of Ni-MoS<sub>2</sub>-V<sub>S</sub> system. A sulphur atom was removed from its basal plane, so that a sulphur vacancy (V<sub>S</sub>) is formed and a Mo atom next to it was substituted with a Ni dopant. After geometry optimization, the Ni atom changes its position closer to the one side, away from the sulphur vacancy (Figure 27).

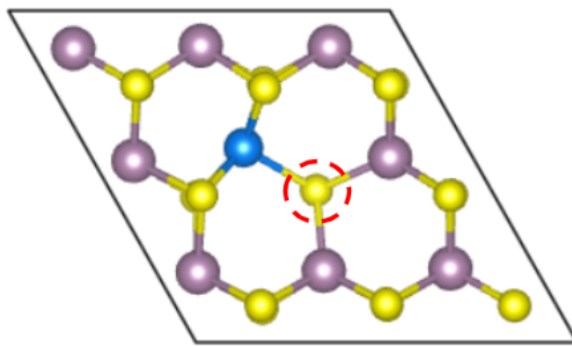


Figure 27: Top view of Ni-MoS<sub>2</sub>-V<sub>S</sub> monolayer.

Then, we introduce a hydrogen atom close to the sulphur vacancy. We observe that it stays in a distance above and away from the center of the sulphur atom that is below V<sub>S</sub> (Figure 28).

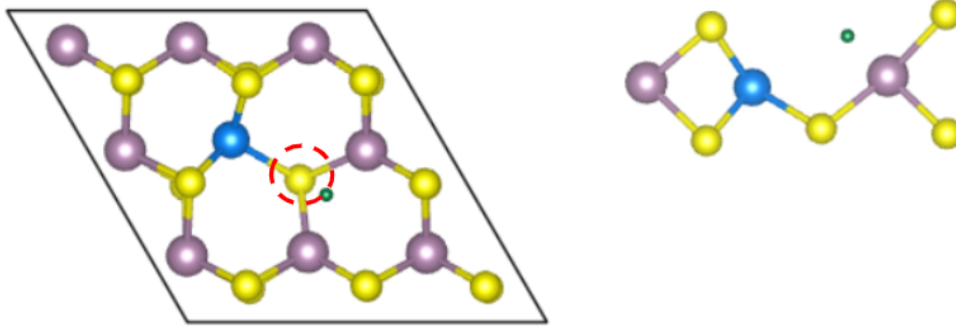


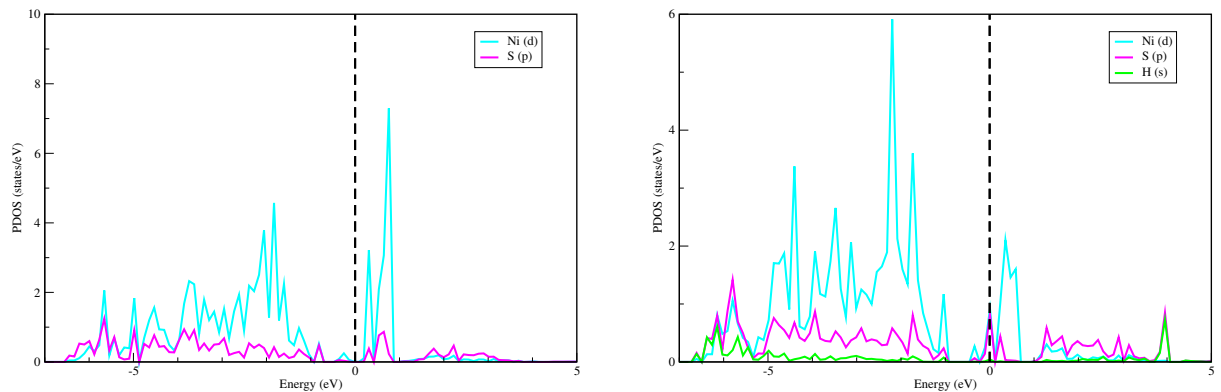
Figure 28: Top and side view of Ni-MoS<sub>2</sub>-V<sub>S</sub> monolayer after hydrogen adsorption.

The energies of this structure were also calculated and are presented in Table 8. The  $\Delta G_H$  is equal to 0.007 eV, close to 0 eV derived in another work [54].

Table 8: Hydrogen binding energy  $\Delta E_H$  and hydrogen adsorption free energy  $\Delta G_H$  for Ni-MoS<sub>2</sub>-V<sub>S</sub> monolayer.

	current work	other theoretical studies
$\Delta E_H$ (eV)	-0.233	
$\Delta G_H$ (eV)	0.007	$\simeq 0.000$ [52]

Finally, we examine the PDOS for this system. As we see in Figure 29(a), before hydrogen adsorption, there are new states introduced due to the Ni-d orbitals. They are also hybridized in a small degree with S-p orbitals. By introducing hydrogen, Figure 29(b), these states decrease their densities and there is a down shift in the valence and conduction band. Hydrogen hybridization is strong far from the Fermi level.



(a) PDOS of Ni-MoS<sub>2</sub>-V<sub>S</sub> before H adsorption. (b) PDOS of Ni-MoS<sub>2</sub>-V<sub>S</sub> after H adsorption.

Figure 29: Partial Density of States of MoS<sub>2</sub>-V<sub>S</sub> system before and after H adsorption.

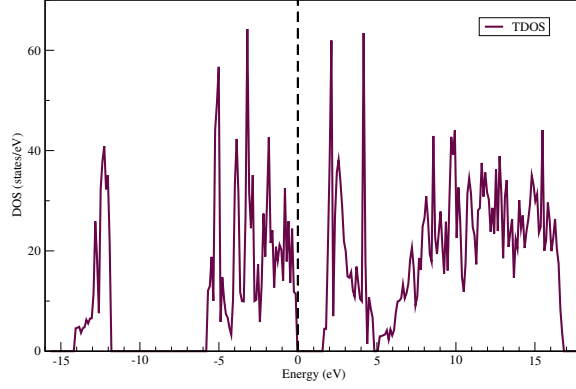
## 4.6 Comparisons on the Total Electronic Density of States

In this chapter, we discuss the Total Density of States of  $\text{MoS}_2\text{-V}_S$ ,  $\text{Ni-MoS}_2$  and  $\text{Ni-MoS}_2\text{-V}_S$ , before and after hydrogen adsorption, in comparison between them and with  $\text{MoS}_2$ . In Figure 30, we compare the  $\text{MoS}_2\text{-V}_S$  system, before and after hydrogen adsorption, with pristine  $\text{MoS}_2$ .

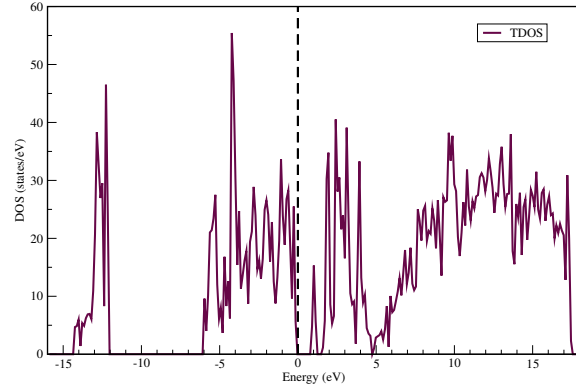
In Figure 30(a), we have the TDOS of  $\text{MoS}_2$  that shows a semiconductor with a band gap. Figure 30(b) shows that the introduction of a sulphur vacancy contributes to gap states closer to the conduction band. The system remains a semiconductor, with defect states in the band gap.

Then, in Figure 30(c), the total DOS of  $\text{MoS}_2\text{-V}_S$  after hydrogen adsorption is presented. We see that the new states change position closer to the Fermi level. The valence and conduction band have shifted down and there is a decrease in the band gap.

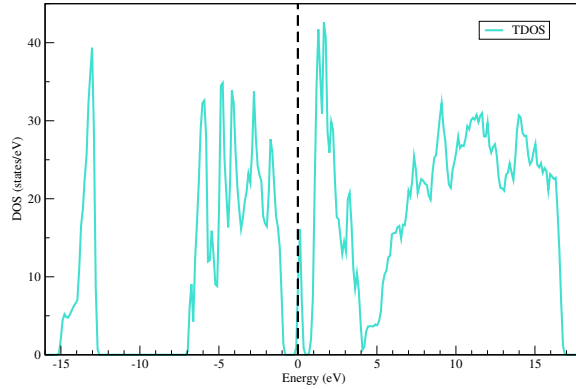
These results are in agreement with the study by Hong Li et al. [52], where the formation of a sulphur vacancy is responsible for the new states near the Fermi level that are depicted in  $\text{MoS}_2\text{-V}_S$  band structure. Tuning of HER activity can be achieved either by changing the concentration of the sulphur vacancies or by applying strain to it.



(a) Total DOS of MoS<sub>2</sub>.



(b) Total DOS of MoS<sub>2</sub>-V<sub>S</sub> before hydrogen adsorption.

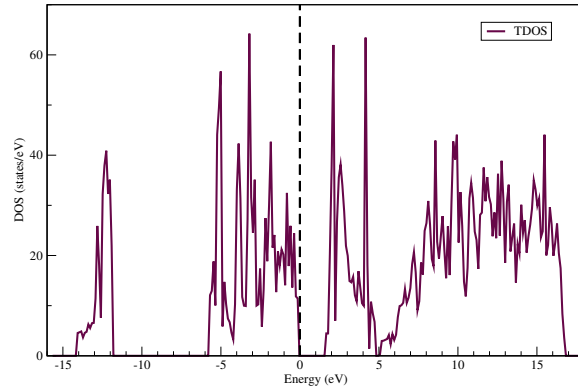


(c) Total DOS of MoS<sub>2</sub>-V<sub>S</sub> after hydrogen adsorption.

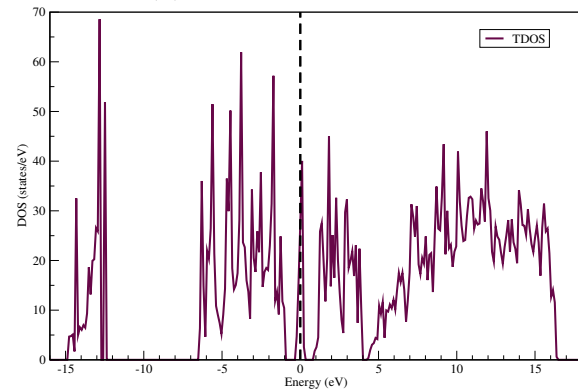
Figure 30: Total Density of States for MoS<sub>2</sub> and MoS<sub>2</sub>-V<sub>S</sub>, before and after hydrogen adsorption.

In Figure 31, the TDOS of MoS<sub>2</sub> and Ni-MoS<sub>2</sub> before and after hydrogen adsorption are presented. In Figure 31(b) that describes the Ni-MoS<sub>2</sub> TDOS before hydrogen adsorption, we observe that there is a down shift of the valence and conduction band. Also, new states are introduced near the Fermi level. The system changes to metallic from semiconducting.

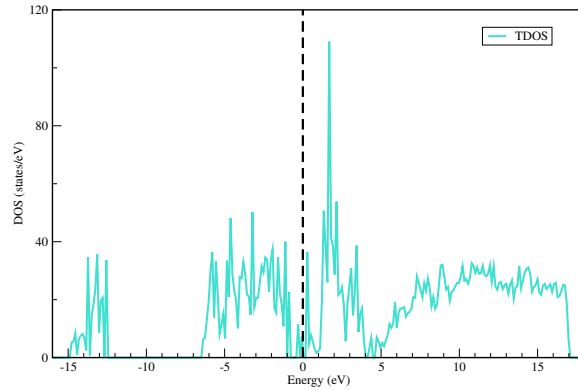
After hydrogen adsorption in Figure 31(c), the system is still metallic, with its states localized closer to the Fermi level.



(a) Total DOS of MoS<sub>2</sub>.



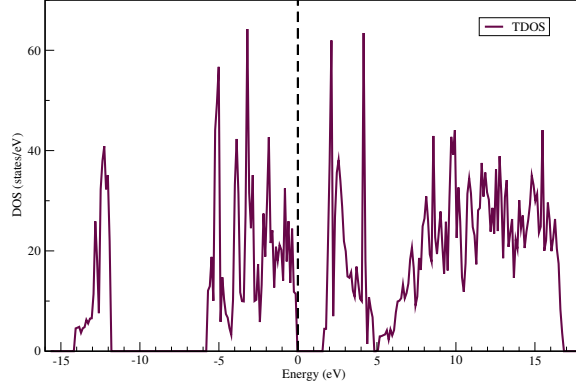
(b) Total DOS of Ni-MoS<sub>2</sub>.



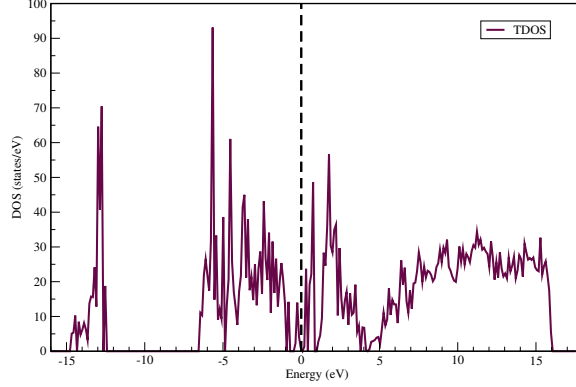
(c) Total DOS of Ni-MoS<sub>2</sub>.

Figure 31: Total Density of States for MoS<sub>2</sub> and Ni-MoS<sub>2</sub> before and after hydrogen adsorption.

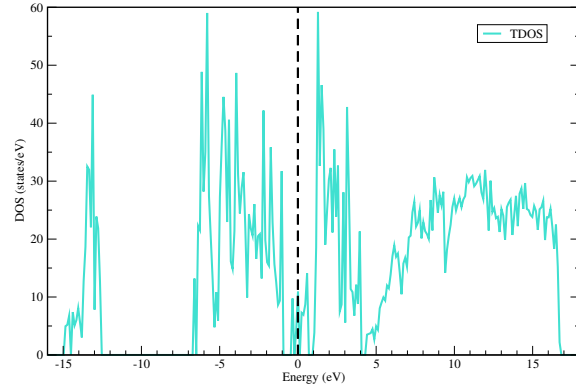
Figure 32 compares the Ni-MoS<sub>2</sub>-V<sub>S</sub>, before and after hydrogen adsorption with MoS<sub>2</sub>.



(a) Total DOS of  $\text{MoS}_2$ .



(b) Total DOS of  $\text{Ni-MoS}_2\text{-V}_S$ .



(c) Total DOS of  $\text{Ni-MoS}_2\text{-V}_S$  after hydrogen adsorption.

Figure 32: Total Density of States for  $\text{MoS}_2$  and  $\text{Ni-MoS}_2\text{-V}_S$  before and after hydrogen adsorption.

According to Figure 32(b) for TDOS of  $\text{Ni-MoS}_2\text{-V}_S$ , more states are introduced near the Fermi level than in the case of  $\text{Ni-MoS}_2$ . Its density distortion near the Fermi level, opens up a small gap. There is also a shift in the valence and conduction band. After hydrogen adsorption in Figure 32(c), the system remains metallic and its states are localized closer to the Fermi level.

The existence of metallic states and the down shift of valence band have also been discussed by J.Deng et al. [52] for hydrogen adsorption on Pt-MoS<sub>2</sub>. This system shows an efficient performance close to thermoneutral for HER reaction and suggests that the hybridized states of the metal dopant with Mo and S atoms of the basal plane are responsible for enhancing HER activity. In our study, for the case of Ni-doped and with a sulphur vacancy system (Ni-MoS<sub>2</sub>-V<sub>S</sub>), we observe the most efficient hydrogen adsorption ability compared to the other ones. Also, there are more states near the Fermi level for Ni-MoS<sub>2</sub>-V<sub>S</sub> system in resemblance with the Pt-MoS<sub>2</sub> which is an efficient catalyst.

Figure 33 shows the Partial Density of States (PDOS) of MoS<sub>2</sub>-V<sub>S</sub>, Ni-MoS<sub>2</sub> and Ni-MoS<sub>2</sub>-V<sub>S</sub>. We examine the hybridization between their atoms.

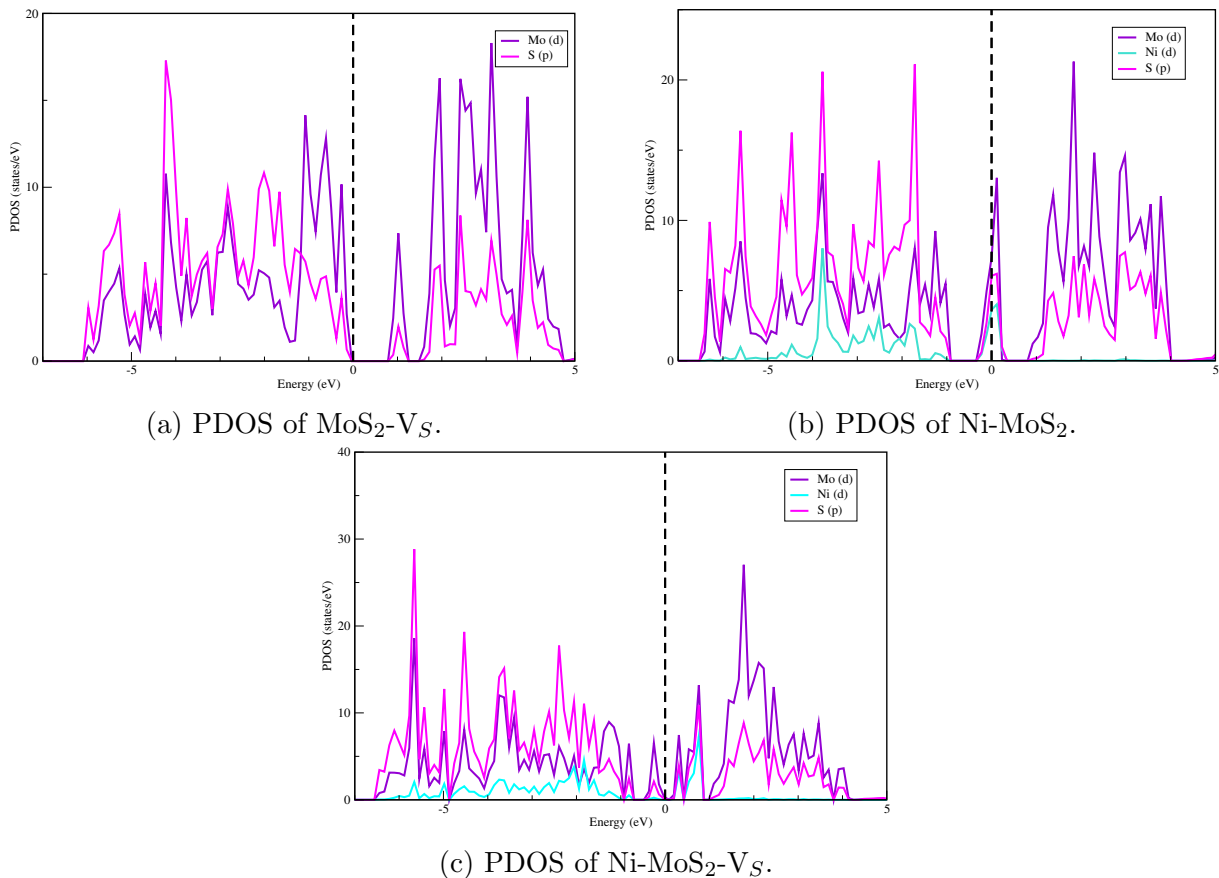


Figure 33: Partial Density of States of MoS<sub>2</sub>-V<sub>S</sub>, Ni-MoS<sub>2</sub> and Ni-MoS<sub>2</sub>-V<sub>S</sub>.

In Figure 33(a), that shows PDOS of  $\text{MoS}_2\text{-V}_S$ , the state in the band gap occurs due to the hybridization between Mo-d and S-p orbitals. The contribution of S-p orbitals is smaller compare to Mo-d orbitals. Also, they are hybridized along valence and conduction band.

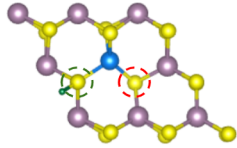
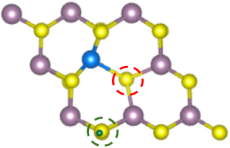
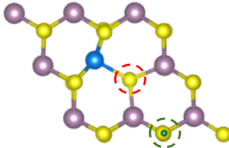
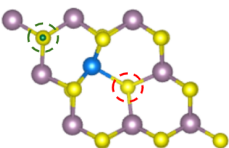
For Ni- $\text{MoS}_2$  system in Figure 33(b), there is hybridization especially in the new states located at the Fermi level, between Mo-d , Ni-d and S-p orbitals. In addition, Ni dopant hybridizes along the valence band with the other two metals. However, Ni dopant states disappear in the conduction band.

Finally, for Ni- $\text{MoS}_2\text{-V}_S$ , there is hybridization in the states near the Fermi level. Between Fermi level and conduction band there is strong hybridization of Ni dopant and S atoms. In the area below Fermi level, Ni-dopant hybridizes with the other atoms in a smaller degree. There is no density of states for Ni-dopant in the conduction band.

#### 4.7 Adsorption Sites of Ni- $\text{MoS}_2\text{-V}_S$

We examine different adsorption sites of sulphur atoms of Ni- $\text{MoS}_2\text{-V}_S$  basal plane. These sites labelled S1, S2, S3 and S4 are presented in Table 9. We start with S1 adsorption site, which is the closest neighbour to Ni dopant and also close to sulphur vacancy. In a longer distance from Ni dopant is S2 site that is also direct neighbour to  $\text{V}_S$ . Then, S3 has a position close to  $\text{V}_S$ , but is not a direct neighbour to Ni. In contrast, S4 adsorption site is close to Ni, but not direct neighbour to  $\text{V}_S$ .

Table 9: Structural configurations and hydrogen adsorption free energies ( $\Delta G_H$ ) for different adsorption sites of sulphur atoms of the basal plane of Ni- $\text{MoS}_2\text{-V}_S$ .

Ni- $\text{MoS}_2\text{-V}_S$	S1	S2	S3	S4
				
$\Delta E_H$ (eV)	0.25	1.03	1.02	0.98
$\Delta G_H$ (eV)	0.49	1.27	1.26	1.22

We place a hydrogen atom on top and in a distance of 1 Å from the sulphur atom of the basal plane. After geometry optimization calculations, we obtain the configurations of Table 9. In S1 adsorption site, we have the lowest  $\Delta G_H$  value. As we choose an adsorption site away from Ni- $\text{V}_S$ , we see that the binding of hydrogen becomes weaker. The S2 and S3 positions have quite similar  $\Delta G_H$  values so that when the sulphur adsorption site is closer to  $\text{V}_S$  the interaction with hydrogen becomes weaker. For S4 site, we have a  $\Delta G_H$  value close to S2 and S3, but slightly smaller. This suggest that Ni dopant has an attractive effect to hydrogen in this system.

We also investigate the geometry configurations of these adsorption sites. We observe that S1 site differs in the position of Ni dopant compared to the others. Ni is closer to the sulphur vacancy and the bond between S at S1 and Ni atom breaks. For the other adsorption sites Ni moves to the side away from sulphur vacancy and there is no bond break.

We compare hydrogen adsorption energies for MoS<sub>2</sub>, MoS<sub>2</sub>-V<sub>S</sub>, Ni-MoS<sub>2</sub> and Ni-MoS<sub>2</sub>-V<sub>S</sub> for the referred adsorption sites. As we see in Figure 34, MoS<sub>2</sub>-V<sub>S</sub> and Ni-MoS<sub>2</sub>-V<sub>S</sub> have lower  $\Delta G_H$  values for all adsorption sites compared to 2.08 eV of MoS<sub>2</sub> basal plane. Consequently, the sulphur vacancy contributes to hydrogen adsorption energy being closer to zero. The Ni-MoS<sub>2</sub> system has more negative energy values for V<sub>S</sub> and S1 sites far from thermoneutral, but for S3 and S4 sites they become highly positive (7.21 eV and 7.18 eV respectively) (Table 24 in the Appendix).

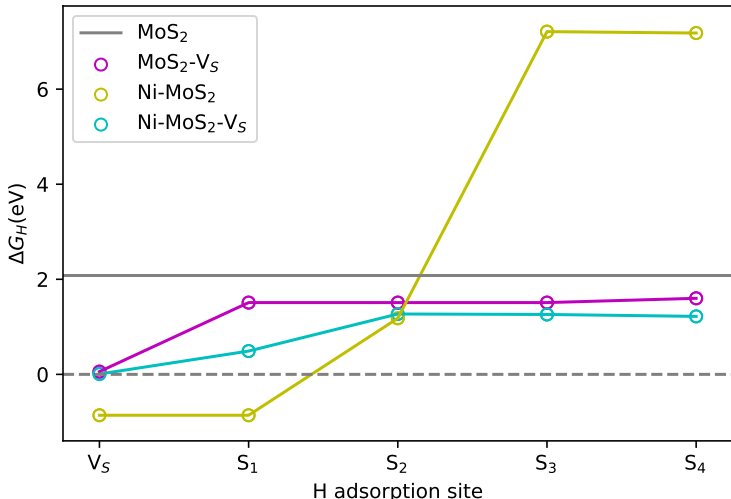


Figure 34: Hydrogen adsorption free energy of different adsorption sites of sulphur atoms in the basal plane of MoS<sub>2</sub>, MoS<sub>2</sub>-V<sub>S</sub>, Ni-MoS<sub>2</sub> and Ni-MoS<sub>2</sub>-V<sub>S</sub>.

From the figure above, MoS<sub>2</sub>-V<sub>S</sub> has only hydrogen adsorption ability near the sulphur vacancy site. In the other hydrogen adsorption positions, the energies differ slightly and are highly positive, suggesting a weak interaction with hydrogen. Ni-MoS<sub>2</sub> has negative energy values at V<sub>S</sub> and S1 sites. Then, at S2 site, the energy changes to positive sign. These adsorption sites indicate a local effect of Ni dopant on the system, so that there is a strong hydrogen binding to the direct neighbour S atoms of the Ni dopant. However, we have to mention that in both cases with positive and negative adsorption energy, the energy values are far from thermoneutral, as the binding with hydrogen is too strong in one case and too weak in the other. As we move away from Ni dopant, the energy becomes even more positive, especially at S3 and S4 sites. This suggests that the binding energy  $\Delta E_H$  takes high values, so that the binding with hydrogen is not energetically favourable and energy is demanded for further changes in their geometry configurations.

For Ni-MoS<sub>2</sub>-V<sub>S</sub> system at sulphur vacancy site, hydrogen adsorption free energy is close to thermoneutral. In addition, for S1 site, it has a better performance compare to the other systems. Its hydrogen adsorption ability at S2 site is quite similar to Ni-MoS<sub>2</sub>. However, its performance for S3 and S4 is better compared to the other system, but still interacts weakly with hydrogen.

Comparing their configurations with the other systems (Table 24 in the Appendix), we observe that for S1 site, Ni-MoS<sub>2</sub>-V<sub>S</sub> is an intermediate state between MoS<sub>2</sub>-V<sub>S</sub>, where Mo near V<sub>S</sub> is in the center of the structure and Ni-MoS<sub>2</sub> system, where Ni dopant has a bond break between S at S1 and Ni and is closer to one side. The bond break might create more dangling states so that hydrogen is attracted stronger by sulphur for Ni-MoS<sub>2</sub>. At S2 site for Ni-MoS<sub>2</sub> there is no bond break in the structure and Ni is closer to the center. Its configuration is quite similar to MoS<sub>2</sub>-V<sub>S</sub>, but it has better performance. However, the introduction of a V<sub>S</sub> changes the position of Ni dopant closer to the one side in Ni-MoS<sub>2</sub>-V<sub>S</sub>, so that  $\Delta G_H$  becomes slightly higher.

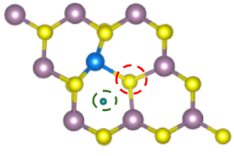
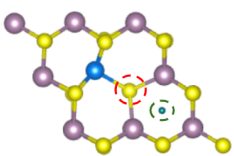
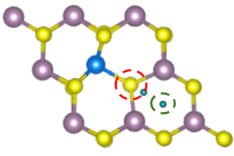
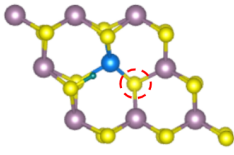
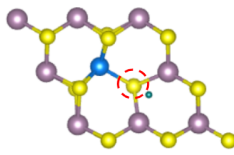
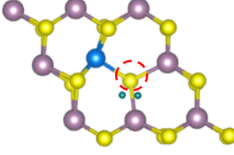
In S3 adsorption site, for Ni-MoS<sub>2</sub>, a bond breaks between Ni and neighbour S, so that Ni is in a position closer to hydrogen adsorption site. In the case of Ni-MoS<sub>2</sub>-V<sub>S</sub>, the sulphur vacancy makes Ni to be also in one side but away from hydrogen. Thus, the configuration for the first case needs more energy for the bond break and change of Ni position than its initial state, so that  $\Delta G_H$  has a high positive value. Finally, for S4 adsorption site, we have a similar situation for Ni-MoS<sub>2</sub>, but Ni atom changes position to a different side, as hydrogen is closer to a different direction than before. Also, a bond between Ni and S atom breaks. For Ni-MoS<sub>2</sub>-V<sub>S</sub> the existence of sulphur vacancy does not demand more energy for bond break, but only Ni dopant changes its position closer to the adsorption site.

From the above observations, we can conclude to results about the role of V<sub>S</sub>, Ni dopant and the combination of them. The V<sub>S</sub> formation activates the basal plane of MoS<sub>2</sub> in its neighbourhood, in agreement with latest studies [49, 51]. The metal dopant enhances the hydrogen adsorption ability of the basal plane in its local area. However, it has a stronger effect compared to V<sub>S</sub> formation. The combination of Ni dopant and V<sub>S</sub> makes the system closer to thermoneutral for adsorption sites near the sulphur vacancy. Also, it lowers the demand for energy needed for system reorganisation at S3 and S4 sites, compared to the Ni-MoS<sub>2</sub> case.

## 4.8 Hydrogen Adsorption Site on the Ring of Basal Plane

We studied the hydrogen adsorption ability on the ring of MoS<sub>2</sub>. In Table 10 below, systems with different adsorption sites and coverage effect for c2 system are presented.

Table 10: Structural configurations before and after hydrogen adsorption. Hydrogen adsorption free energies ( $\Delta G_H$ ) and differential hydrogen adsorption free energy ( $\Delta G_H^{diff}$ ) for different adsorption sites of Ni-MoS<sub>2</sub>-V<sub>S</sub> ring of the basal plane.

	c1	c2	c2/2H
initial			
final			
$\Delta G_H$ (eV)	0.62	0.00	0.63

For the system with c1 adsorption site, where the ring contains both Ni dopant and sulphur vacancy, hydrogen relocates to a position between Ni atom and S1 adsorption site, breaking the bond between them. The  $\Delta G_H$  is positive suggesting a weak interaction.

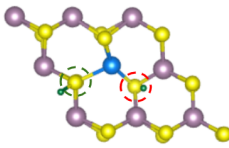
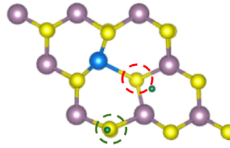
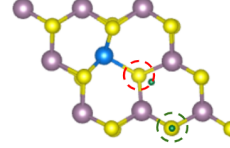
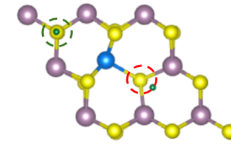
Hydrogen at c2 adsorption site changes its position closer to the sulphur vacancy, so it has the same configuration and energy 0.005 eV, in agreement within error with 0.007 eV that it was found previously for V<sub>S</sub> adsorption site. We have to note that the ring that surrounds c2 contains only the sulphur vacancy.

Then, we use the c2 configuration with one hydrogen already adsorbed and we introduce a second one at c2 adsorption site. The bond length between the two hydrogen atoms is 0.81 Å, so that they do not form a molecule. Also, the energy value is around 0.63 eV suggesting a weak interaction.

## 4.9 Hydrogen Coverage Effect on Ni-MoS<sub>2</sub>-V<sub>S</sub>

We perform calculations for the hydrogen coverage effect for Ni-MoS<sub>2</sub>-V<sub>S</sub> system. The adsorption sites are S1, S2, S3 and S4 that were examined previously (Table 11). A hydrogen atom is already adsorbed in the sulphur vacancy site and then a second one is introduced in a neighbour sulphur atom. We used the V<sub>S</sub> adsorption site for the first hydrogen adsorption, because it has the highest adsorption ability compared to the other ones for the studied systems, so that a hydrogen is more likely to be adsorbed in this position. Their structural configurations and differential hydrogen adsorption free energies are shown in the table below.

Table 11: Structural configurations and differential hydrogen adsorption free energies ( $\Delta G_H^{diff}$ ) for different adsorption sites of sulphur atoms of the basal plane of Ni-MoS<sub>2</sub>-V<sub>S</sub>.

Ni-MoS <sub>2</sub> -V <sub>S</sub>	S1	S2	S3	S4
				
$\Delta G_H$ (eV)	0.08	1.16	1.27	1.25

The S1 site has the lowest energy compared to the other ones that have more positive values. It has a value close to thermoneutral, so it is active for HER. In the other adsorption sites, we have a weaker interaction with hydrogen. Hence, the introduction of a hydrogen near the sulphur vacancy site alters the hydrogen adsorption ability of the neighbour sulphur atoms. The S1 site becomes active for HER and the S2 site, which it is in a longer distance from V<sub>S</sub>, it has a smaller energy value compared to the single hydrogen adsorption. Sites in a longer distance from V<sub>S</sub>, such as S3 and S4, have no difference in energy and the interaction with hydrogen remains weak.

Studying their structural configurations, we observe that for S1 site, Ni dopant is in a position closer to V<sub>S</sub> and the bond between S at S1 and Ni breaks. However, for the other cases, the position of Ni atom is away from V<sub>S</sub>, and no bond break happens. The same configurations were also observed for the adsorption of a single hydrogen in the system. So the existence of a hydrogen in the V<sub>S</sub> site has not a significant impact in the geometry of the structures.

Figure 35 shows the differential hydrogen adsorption free energy ( $\Delta G_H^{diff}$ ) for different adsorption sites of sulphur atoms in the basal plane of MoS<sub>2</sub>-V<sub>S</sub>, Ni-MoS<sub>2</sub> and Ni-MoS<sub>2</sub>-V<sub>S</sub>. MoS<sub>2</sub>-V<sub>S</sub> has high positive energy values for all of its adsorption sites. The adsorption of a hydrogen in the vacancy site lowers in a small degree the energy for the neighbour to V<sub>S</sub> sites, but they are not sufficient for HER activation.

The Ni-MoS<sub>2</sub> system has smaller positive  $\Delta G_H^{diff}$  values compared to MoS<sub>2</sub>-V<sub>S</sub>, but also far from thermoneutral. As we move away from the Ni dopant, there is a small increase in the energy value. Then, for Ni-MoS<sub>2</sub>-V<sub>S</sub>, we observe that S1 has the best performance compared to the other systems and close to thermoneutral. However, for S2, S3 and S4 sites, it has similar performance with Ni-MoS<sub>2</sub>. For Ni-MoS<sub>2</sub> the introduction of a hydrogen near Ni atom helps the system to reorganise, so that it needs less energy for a second hydrogen adsorption. Especially for S3 and S4 that have highly positive energies in the single hydrogen adsorption, we observe that the energy values decrease seriously and are similar to Ni-MoS<sub>2</sub>-V<sub>S</sub> (Table 25 in the Appendix).

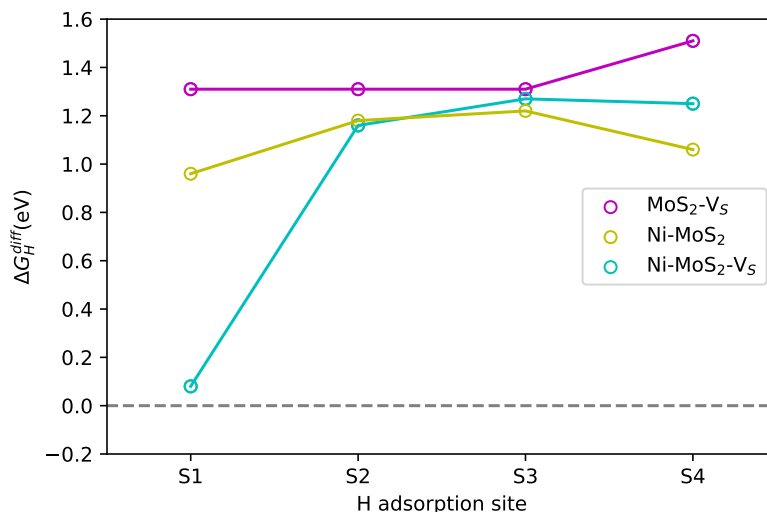


Figure 35: Differential hydrogen adsorption free energies ( $\Delta G_H^{diff}$ ) for different adsorption sites of sulphur atoms in the basal plane of MoS<sub>2</sub>-V<sub>S</sub>, Ni-MoS<sub>2</sub> and Ni-MoS<sub>2</sub>-V<sub>S</sub>.

For MoS<sub>2</sub>-V<sub>S</sub>, there are no significant changes in its structure after adding a second hydrogen for the different adsorption sites. For S1 site in Ni-MoS<sub>2</sub> we see that Ni occupies a position away from the adsorption site of the first hydrogen, so that the bond between Ni and S breaks. However for Ni-MoS<sub>2</sub>-V<sub>S</sub>, Ni dopant moves closer to sulphur vacancy site, without breaking a bond. The position of the Ni atom for all the other adsorption sites both for Ni-MoS<sub>2</sub> and Ni-MoS<sub>2</sub>-V<sub>S</sub> is similar (Table 25 in the Appendix).

Finally, we examine the increase in the hydrogen coverage for MoS<sub>2</sub>-V<sub>S</sub> and Ni-MoS<sub>2</sub>-V<sub>S</sub> systems. Initially hydrogen was introduced in the V<sub>S</sub> site. After geometry optimization, a second one was placed in S1 site. Then, in the remaining sulphur near the Mo or Ni, a hydrogen atom was introduced. In Table 12, their geometry configurations and differential hydrogen adsorption free energies are presented. The structure of MoS<sub>2</sub>-V<sub>S</sub> is not affected by the addition of hydrogen atoms, with Mo atom in its initial position as well as the neighbouring sulphur atoms. For Ni-MoS<sub>2</sub>-V<sub>S</sub>, the position of Ni is quite similar with S1 configuration. However, Ni has coordination three with the neighbouring sulphur atoms.

The differential hydrogen adsorption free energy for MoS<sub>2</sub>-V<sub>S</sub> is positive and greater than Ni-MoS<sub>2</sub>-V<sub>S</sub>. Both systems interact weakly with the third hydrogen, suggesting a decrease in their activities.

Table 12: Structural configurations and differential hydrogen adsorption free energies ( $\Delta G_H^{diff}$ ) for  $\text{MoS}_2\text{-V}_S$  and  $\text{Ni-MoS}_2\text{-V}_S$  with three adsorbed hydrogen atoms.

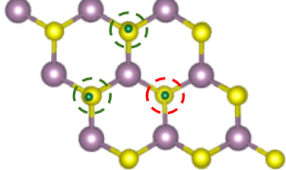
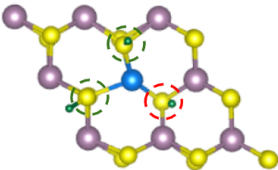
	$\text{MoS}_2\text{-V}_S$	$\text{Ni-MoS}_2\text{-V}_S$
		
$\Delta G_H^{diff}$ (eV)	1.60	1.01

Figure 36 shows the differential hydrogen adsorption free energy versus the hydrogen coverage ( $\theta_H$ ). A comparison of the Ni-doped and undoped system is presented. Despite the fact that both systems have close to zero values at  $\text{V}_S$  site, they behave differently when other hydrogen atom are introduced in the system.  $\text{MoS}_2\text{-V}_S$  is inactive after the first hydrogen adsorption. The sulphur vacancy achieves to activate the basal plane, but has an effect only to the local area of  $\text{V}_S$ . For the Ni-doped system, Ni achieves to enhance the performance of the neighbour sulphur atoms. It is easier to add a second hydrogen at S1 site, when one is already adsorbed on the  $\text{V}_S$  site. After adding a third hydrogen, its hydrogen adsorption ability declines, but its energy value is smaller than the undoped system.

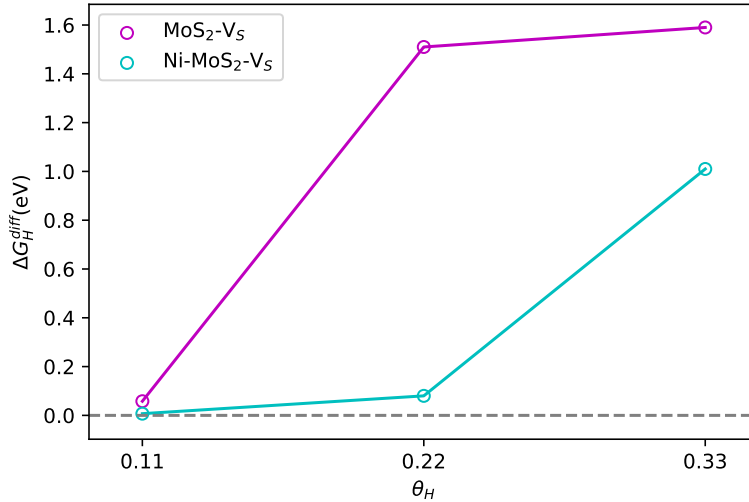


Figure 36: Differential hydrogen adsorption free energy ( $\Delta G_H^{diff}$ ) versus hydrogen adsorption coverage ( $\theta_H$ ) for  $\text{MoS}_2\text{-V}_S$  and  $\text{Ni-MoS}_2\text{-V}_S$ .

As we see from the previous results, for all the structures when introducing a single hydrogen in the system, their hydrogen adsorption ability is lower than the one in the  $\text{V}_S$

site. The existence of an already adsorbed hydrogen alters the system HER performance, especially at the neighbour adsorption sites, by tuning the hydrogen adsorption free energy of the system closer to zero. Also, a Ni dopant can create a similar effect to the  $V_S$ . However, the combination of the two, can have a greater effect in the adsorption sites near the Ni dopant.

The hydrogen coverage effect has an important role for HER. The existence of active adsorption sites within range can adjust the rate of the reaction. For example, Tafel step requires two adsorption sites for hydrogen molecule formation. On the one hand, it is necessary that hydrogen binds not too strongly to the catalyst surface, to avoid occupation of the available adsorption sites and poisoning of the catalyst. On the other hand, the interaction with hydrogen should not be weak, as then the material has only one adsorption site and the chance of hydrogen to bind with catalyst surface decreases. Thus, other adsorption sites close to thermoneutral are required to increase the chance of hydrogen formation and the efficiency of the catalyst.

#### 4.10 The Heyrovsky step

We perform calculations in order to examine the desorption step of HER reaction for Ni-MoS<sub>2</sub>- $V_S$ . Considering that other sulphur adsorption sites which are in a distance from  $V_S$  adsorption site are less active for HER, the Tafel mechanism is not suitable, as it demands two neighbouring adsorbed hydrogen atoms. Therefore, Heyrovsky mechanism needs to be investigated. When a hydrogen is already adsorbed on the catalyst surface, a second proton from the solution binds with it, so that a hydrogen molecule is formed and released from its surface.

For Ni-MoS<sub>2</sub>- $V_S$ , we choose the  $V_S$  adsorption site that has the best HER performance and after having a hydrogen adsorbed, we introduce a second one in a distance of 1 Å above the first one. We compare this system with the undoped one (Figure 37).

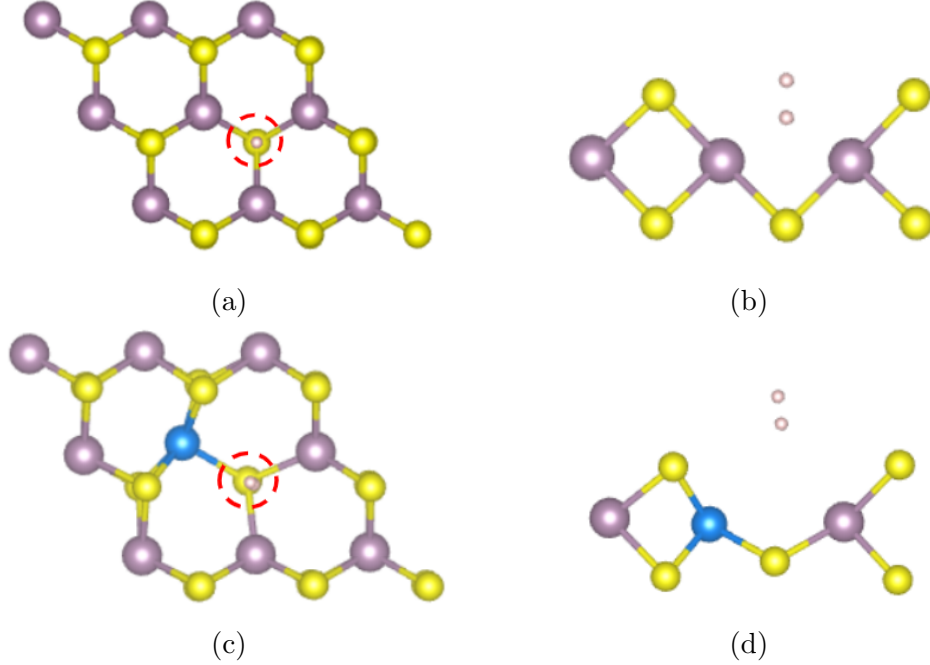


Figure 37: Top view ((a), (c)) and side view ((b),(d)) of  $\text{MoS}_2\text{-V}_S\text{-H}_2$  and  $\text{Ni-MoS}_2\text{-V}_S\text{-H}_2$  respectively.

In the following Table 13, the structural parameters for  $\text{MoS}_2\text{-V}_S\text{-H}_2$  and  $\text{Ni-MoS}_2\text{-V}_S\text{-H}_2$  are shown. For the case of the undoped system the distance between Mo and S atom below the hydrogen is 2.41 Å. Previous calculations on single hydrogen adsorption on  $\text{V}_S$  site, suggest this distance to be 2.38 Å and 2.40 Å before and after hydrogen adsorption. So,  $\text{MoS}_2\text{-V}_S\text{-H}_2$  has a structure closer to  $\text{MoS}_2\text{-V}_S\text{-H}$ . However, for  $\text{Ni-MoS}_2\text{-V}_S\text{-H}_2$ , this value is 2.32 Å, which is closer to 2.33 Å that refers to the system without H and smaller than the one with hydrogen (2.37 Å). The distance between hydrogen molecule and sulphur ( $d_{\text{H}_2\text{-S}}$ ) is greater for the Ni-doped system. Finally, according to the distance between the two hydrogen atoms,  $\text{MoS}_2\text{-V}_S\text{-H}_2$  has a longer distance, while Ni-doped one is in accordance with the experimental value of 0.75 Å. Thus, a hydrogen molecule is formed and is in a distance from the adsorption site of the catalyst surface for the Ni-doped system.

Table 13: Structural parameters for  $\text{MoS}_2\text{-V}_S\text{-H}_2$  and  $\text{Ni-MoS}_2\text{-V}_S\text{-H}_2$ .

	$d_{\text{TM-S}}(\text{Å})$	$d_{\text{H}_2\text{-S}}(\text{Å})$	$d_{\text{H-H}}(\text{Å})$
$\text{MoS}_2\text{-V}_S\text{-H}_2$	2.41	2.63	0.91
$\text{Ni-MoS}_2\text{-V}_S\text{-H}_2$	2.32	3.78	0.75

In Table 14, the values of the differential hydrogen adsorption free energy ( $\Delta G_H^{diff}$ ) and hydrogen molecule adsorption free energy ( $\Delta G_{H_2}$ ) are given. For the case of MoS<sub>2</sub>-V<sub>S</sub>,  $\Delta G_H^{diff}$  is highly positive, so that the second hydrogen is repulsed from the adsorption site. By estimating the  $\Delta G_{H_2}$ , which is also highly positive, we observe that the two hydrogens do not bind to the catalyst surface. This also may explain the longer bond length between them. For Ni-MoS<sub>2</sub>-V<sub>S</sub>, the  $\Delta G_H^{diff}$  value is small positive, so that a second hydrogen comes close to its surface and binds weakly with the adsorbed one. For the hydrogen molecule,  $\Delta G_{H_2}$  has also a small positive value, but far from thermoneutral, so that a hydrogen molecule can be formed and stay close to the catalyst surface, without interacting with it.

Table 14: Differential Hydrogen adsorption free energy ( $\Delta G_H^{diff}$ ) and molecular hydrogen adsorption free energy ( $\Delta G_{H_2}$ ) for MoS<sub>2</sub>-V<sub>S</sub>-H<sub>2</sub> and Ni-MoS<sub>2</sub>-V<sub>S</sub>-H<sub>2</sub>.

	$\Delta G_H^{diff}$ (eV)	$\Delta G_{H_2}$ (eV)
MoS <sub>2</sub> -V <sub>S</sub> -H <sub>2</sub>	2.29	2.11
Ni-MoS <sub>2</sub> -V <sub>S</sub> -H <sub>2</sub>	0.49	0.25

Consequently, the Heyrovsky step is a potential mechanism for Ni-MoS<sub>2</sub>-V<sub>S</sub>, as a hydrogen molecule can be formed and released from the adsorption site. As we know, hydrogen adsorption free energy has to be close to zero, in order to have an efficient catalyst. A stronger binding of hydrogen to the catalyst surface, can lower the rate of desorption, and a weaker one does not favour hydrogen molecule formation. Hence, in order to have an efficient catalyst, a material should work efficiently in both conditions. The fact that Ni-MoS<sub>2</sub>-V<sub>S</sub> has a hydrogen adsorption free energy close to zero, so that hydrogen adsorption and desorption occurs in the most efficient way is in agreement with these results that suggest hydrogen molecule formation and release from the catalyst surface, via Heyrovsky mechanism.

#### 4.11 Formation Energy

In order to estimate the chemical potential of S atom ( $\mu_S$ ), we use the assumption that MoS<sub>2</sub> is in thermal equilibrium with Mo and S, according to Komsa and Krasheninnikov study on defects in monolayer MoS<sub>2</sub> [86]. Hence,  $\mu_{MoS_2} = \mu_{Mo} + 2\mu_S$ , so that :

$$\mu_S = \frac{\mu_{MoS_2} - \mu_{Mo}}{2} \tag{44}$$

In the Table 15 the total energies and chemical potentials of the studied systems are shown.

Table 15: Total energies ( $E_{tot}$ ) and chemical potentials ( $\mu$ ) for the studied systems.

System	Total energy (eV)	Chemical potential (eV)
MoS <sub>2</sub> (3x3)	-196.2140389	-21.8015600
Mo(bcc)(2)	-21.8864491	-10.9432246
Ni(fcc)(4)	-21.6932276	-5.4233069
S		-5.4291675
MoS <sub>2</sub> -V <sub>S</sub>	-189.4801425	
Ni-MoS <sub>2</sub>	-185.7687128	
Ni-MoS <sub>2</sub> -V <sub>S</sub>	-181.4232206	

At this point, the formation energy ( $E_{form}$ ) that is defined as the energy difference between the initial and final system, after adding modifications to the initial one is expressed by the relationship:

$$E_{form} = (E_{tot} + \sum_i N_i \mu_i)_{final} - (E_{tot} + \sum_j N_j \mu_j)_{initial} \quad (45)$$

The positive value of  $E_{form}$  suggests that the initial system is favoured energetically, so that energy is needed to produce the final system. In case that it is negative, the final system is preferred than the initial one and there is no demand for energy.

We examine the formation energy for a sulphur vacancy ( $E_{form}^{V_S}$ ), a Mo substitution with Ni ( $E_{form}^{Ni}$ ) and both defects occurring simultaneously on the MoS<sub>2</sub> basal plane ( $E_{form}^{Ni-V_S}$ ). Pristine MoS<sub>2</sub> is the initial system in for all cases. We also performed calculations for Mo substitution with Ni, with MoS<sub>2</sub>-V<sub>S</sub> as initial system.

The relationships below give the defect formation energies and their values are given in Table 16.

$$E_{form}^{V_S} = (E_{MoS_2-V_S} + \mu_S) - (E_{MoS_2}) \quad (46)$$

$$E_{form}^{Ni} = (E_{Ni-MoS_2} + \mu_{Mo}) - (E_{MoS_2} + \mu_{Ni}) \quad (47)$$

$$E_{form}^{Ni-V_S} = (E_{Ni-MoS_2-V_S} + \mu_{Mo} + \mu_S) - (E_{MoS_2} + \mu_{Ni}) \quad (48)$$

Table 16: Formation energy for S vacancy, Mo substitution with Ni and formation of both defects on MoS<sub>2</sub> basal plane.

Defect	Formation energy (eV)
V <sub>S</sub>	1.30
Ni	4.92
V <sub>S</sub> /Ni	3.84

The formation energy for a system that initially has a sulphur vacancy (MoS<sub>2</sub>-V<sub>S</sub>) and then a substitution of Mo atom with Ni happens (Ni-MoS<sub>2</sub>-V<sub>S</sub>), is given by the expression:

$$E_{form} = (E_{Ni-MoS_2-V_S} + \mu_{Mo}) - (E_{MoS_2-V_S} + \mu_{Ni}) \quad (49)$$

so that  $E_{form}$  is equal to 2.54 eV

From the above results, all the  $E_{form}$  values are positive meaning that the final system has higher energy compared to MoS<sub>2</sub> and energy is required to produce them. In case that the formation of the a sulphur vacancy and Ni dopant combination happens simultaneously the energy needed is lower than Ni doping.

However, having already a sulphur vacancy in the basal plane and then doping with Ni needs less energy. Considering that sulphur vacancy is a native defect and in abundance in MoS<sub>2</sub> basal plane [86] and their recent studies show that their production in stable MoS<sub>2</sub> configurations can be achieved experimentally, for example with electrochemical procedures [51], the existence of sulphur vacancy can minimize the amount of required energy for the doping procedure.

## 5 Rational Design of Metal-doped $\text{MoS}_2\text{-V}_S$

### 5.1 HER Activity on Metal doped $\text{MoS}_2\text{-V}_S$

Similar to Ni, we use various metal dopants to examine their hydrogen adsorption ability at the sulphur vacancy adsorption site for the  $\text{MoS}_2\text{-V}_S$  system. We employ transition metal dopants of 4-11 group of periodic table and also Pb that is a post transition-metal. Figure 38 presents their hydrogen adsorption energy  $\Delta G_H$  at  $V_S$ , for the various dopants.

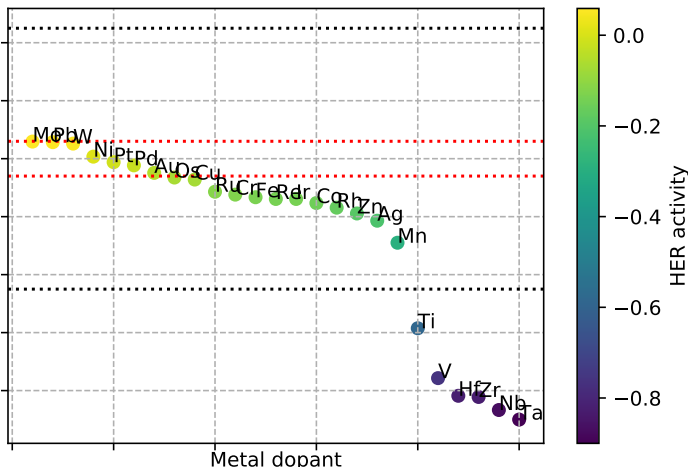


Figure 38: Hydrogen adsorption free energy ( $\Delta G_H$ ) at  $V_S$  adsorption site for Metal doped  $\text{MoS}_2\text{-V}_S$ .

The red lines at 0.06 eV and -0.06 eV denote the area where the dopants are the most sufficient for HER, close to thermoneutral. These values are used because  $\text{MoS}_2$  Mo-edge has  $\Delta G_H = 0.06$  eV. The black dotted lines indicate a larger HER active area from 0.45 eV to -0.45 eV, that derives from the  $\text{MoS}_2$  S-edge with  $\Delta G_H = -0.45$  eV [25]. With yellow color are the values for the dopants closer to zero, Mo, Pb, W, Ni, Pt, Pd and Au. Then there is an area, including Os, Cu, Ru, Cr, Fe, Re, Ir, Co, Rh, Zn, Ag and Mn, with doped systems with more negative energies, so that the binding with hydrogen is strong, but less efficient for HER. Finally there are Ti, V, Hf, Zr, Nb and Ta that belong to the 4 and 5 group and have strongly negative  $\Delta G_H$  values and are not suitable as dopants for the reaction.

Among the transition metal dopants the most efficient for HER are Mo, W, Ni, Pt, Pd and Au. However, despite having values close to zero they do not behave in the same way during HER. For example Mo and W have slightly positive values, so that they bind hydrogen weakly and the adsorption of hydrogen is more difficult. On the other hand, there are Pt and Pd, with slightly negative values, having a stronger interaction with hydrogen. This might make desorption difficult at the second step of HER and lowers the rate of the

reaction. Consequently, Ni that has the closest to zero value (Figure 39) is the most efficient dopant either in adsorption or desorption process.

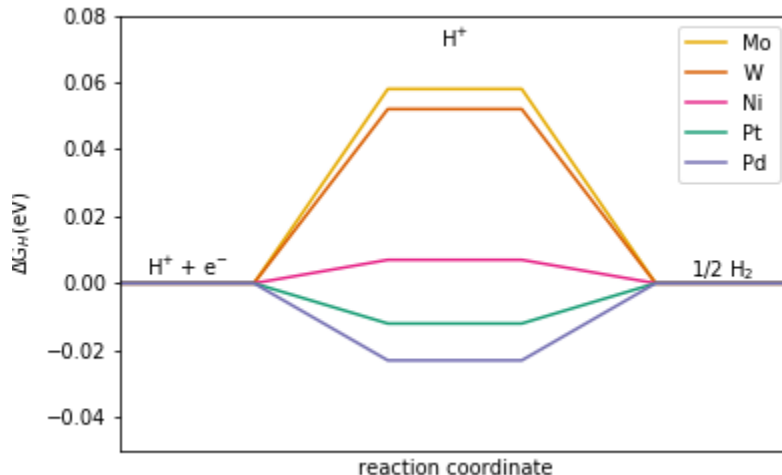


Figure 39: Hydrogen adsorption free energy in respect to the reaction coordinate of HER for Mo, W, Ni, Pt and Pd on TM-MoS<sub>2</sub>-V<sub>S</sub>.

Considering the transition metal dopants that belong within the area of 0.45 eV to -0.45 eV and using the equations (9) and (10), we construct a volcano curve that is in Figure 40. At the right branch there are the dopants with positive  $\Delta G_H$ . The more positive is  $\Delta G_H$ , the weaker is the interaction with hydrogen, so that adsorption is difficult. At the left branch, there are dopants, with negative  $\Delta G_H$  values. The more negative is  $\Delta G_H$ , the more difficult is hydrogen molecule desorption from the catalyst surface. For both cases, as we move away from the top, the rate of the reaction decreases. At the top of the volcano is Ni doped system that has the most efficient rate. Closer to it are Pt and Pd, however they are scarce and expensive metals to be used as catalysts. As, we move away from the top at the left branch, we see a small group consisted of Au, Os and Cu. In the other branch are W and Mo. These ones have better efficiency than S-edge of MoS<sub>2</sub>. Then in the left branch and in a further distance from the others there are metals from 6-9 group that have a smaller rate compared to the others. Finally, Ag and Mn dopants have the slowest rate.

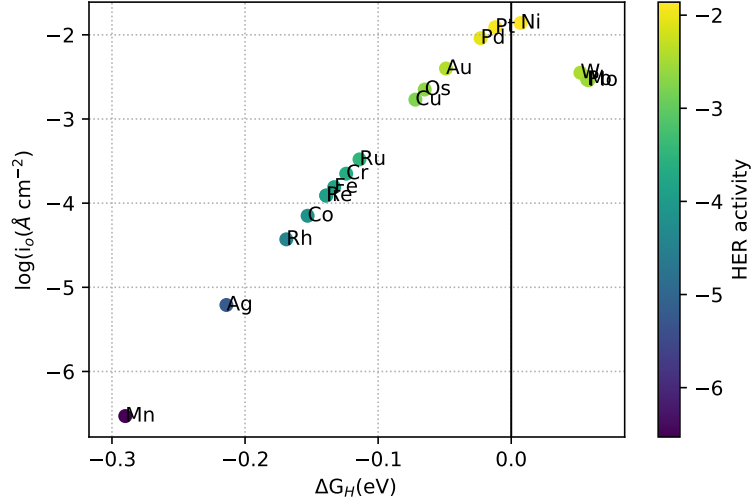


Figure 40: Exchange current density ( $i_0$ ) versus hydrogen adsorption free energy ( $\Delta G_H$ ) for TM-MoS<sub>2</sub>-V<sub>S</sub> with values close to thermoneutral.

In Table 17, the binding energy  $\Delta E_H$  and hydrogen adsorption free energy  $\Delta G_H$  for the referred transition metal dopants are presented.

Table 17: Hydrogen binding energy  $\Delta E_H$  and hydrogen adsorption free energy  $\Delta G_H$  for Ni-MoS<sub>2</sub> monolayer.

Metal dopant	$\Delta E_H$	$\Delta G_H$ (eV)
Ni	-0.233	0.007
Pt	-0.252	-0.012
Pd	-0.263	-0.023
Au	-0.289	-0.049
W	-0.188	0.052
Mo	-0.181	0.058
Os	-0.305	-0.065
Cu	-0.312	-0.072
Cr	-0.364	-0.124
Fe	-0.373	-0.133
Re	-0.379	-0.139
Ir	-0.379	-0.139
Co	-0.393	-0.153
Rh	-0.409	-0.169
Ag	-0.454	-0.214
Mn	-0.530	-0.290

## 5.2 Hydrogen Adsorption Sites of Metal-doped $\text{MoS}_2\text{-V}_S$

Similar to Ni, we examine the hydrogen adsorption ability of several Metal-doped  $\text{MoS}_2\text{-V}_S$  structures for various adsorption sites. We use as dopants transition metals of group 4 to 11 and also Pb that is a post transition metal. By studying their HER activity for different adsorption sites of their basal plane we try to categorize them into different groups. In Figure 41, with green circles indicate the adsorption sites. The S1, S2, S3, S4 and S5 sites are sulphur atoms of its basal plane. The S1 is the closest site both to the metal dopant at S0 and the  $\text{V}_S$  and then is S2 in a longer distance. S3 is close to  $\text{V}_S$ . Finally, S5 is in a direct distance with metal dopant.

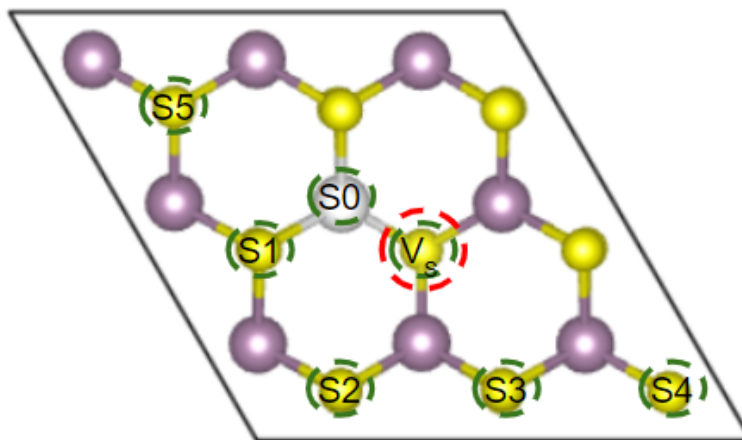


Figure 41: Adsorption sites of Metal-doped  $\text{MoS}_2\text{-V}_S$  basal plane.

From our calculations we construct diagrams that depict the hydrogen adsorption free energy for different adsorption sites of Metal-doped  $\text{MoS}_2\text{-V}_S$ . According to their similar behaviour for the different sites, we categorize them into three groups.

Figure 42 shows the dopants that belong to the metals of 4 and 5 groups of the periodic table (Nb, Zr, Ti, V, Ta and Hf) as well as Mo and Pt.

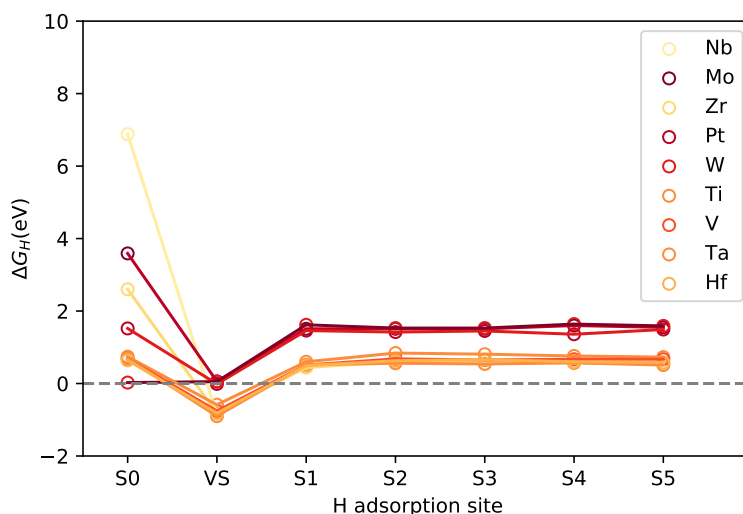


Figure 42: Hydrogen adsorption free energy ( $\Delta G_H$ ) for different adsorption sites for Metal (Nb, Mo, Zr, Pt, Ti, V, Ta and Hf)-doped  $\text{MoS}_2\text{-V}_S$  system.

The metal dopant adsorption site (S0) has the highest positive energy value, varying from 1 eV to 7 eV. However, for  $\text{V}_S$  site they have positive values and close to thermoneutral and highly negative. For the rest of sulphur adsorption sites of the basal plane, their energy values are quite stable and highly positive, suggesting a weak interaction (Table 26 in Appendix).

For  $\text{V}_S$  site they have the best performance, close to thermoneutral. For all the other adsorption sites, they have a weaker interaction with hydrogen. At S0 site, Nb dopant has the highest energy and Hf the smallest one. For Pt, Ti, V, Ta and Hf the energy values both for the metal dopant and sulphur atoms adsorption sites are the same. However, for Nb, Mo and Zr, the S0 site has higher energy values compared to sulphur adsorption sites of the basal plane. The Mo and Pt-doped systems have slightly similar energy values for all the sulphur adsorption sites. Especially for  $\text{V}_S$  site, their energy values are close to thermoneutral. The other metal dopants have similar energies for sulphur adsorption sites between them, but they bind hydrogen stronger at  $\text{V}_S$  site (Table 26 in Appendix). Generally, for all dopants, the most active site is  $\text{V}_S$  and the rest of the basal plane remains catalytically inactive after doping with the metal.

Then, we examine the hydrogen adsorption ability for metal dopants of the 6 to 8 group of the periodic table, except for Mo discussed previously and Ir that belongs to 9 group. Figure 43 shows their hydrogen adsorption ability for different adsorption sites. For all the metal dopants, S0 and  $\text{V}_S$  are active for HER, with values close to thermoneutral and quite similar. The other sulphur adsorption sites have higher positive values with energies of 1.50 eV to 1.75 eV (Table 26 in Appendix).

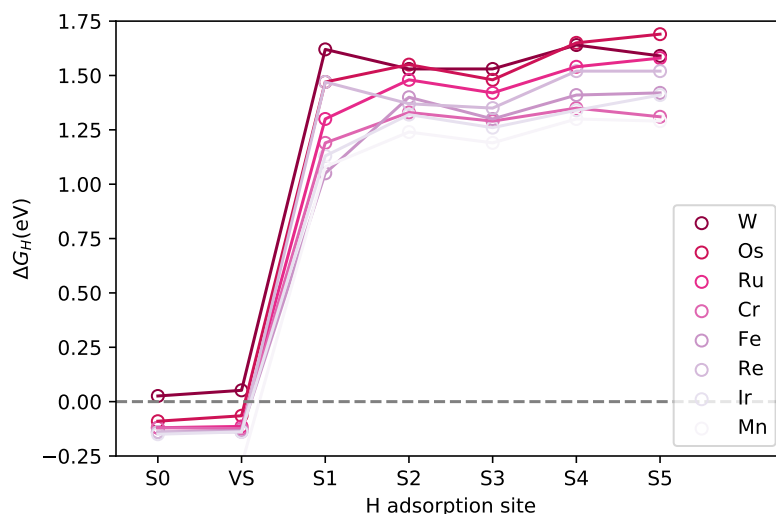


Figure 43: Hydrogen adsorption free energy ( $\Delta G_H$ ) for different adsorption sites for Metal (W, Os, Ru, Cr, Fe, Re, Ir and Mn)-doped  $\text{MoS}_2\text{-V}_S$  systems.

For each metal-doped system, there are small differences between the different sulphur adsorption sites of its basal plane, depending if they are closer to the metal dopant or to the sulphur vacancy. In addition, between the various metal dopants there are small deviations for the sulphur adsorption sites of the basal plane, so that the energy varies from 1.25 eV to 1.75 eV for the different sites.

The W dopant has activity closest to the thermoneutral both for S0 and  $V_S$  adsorption sites. For S0 site it has a slightly smaller value compared to  $V_S$ . The same applies for all the other metal dopants, but having values more negative, suggesting a stronger binding with hydrogen. The more negative value for S0 and  $V_S$ , the smaller positive energies for sulphur adsorption sites of their basal plane (Table 26 in Appendix).

Thus, we have an activation effect of the basal plane, not only in the sulphur vacancy site, but also to the metal dopant that has a similar hydrogen adsorption activity with  $V_S$ . The rest of the basal plane remains inactive. In comparison with the previous case of 4-5 group dopants the activation of the basal plane has a longer range impact. This might be crucial for the second step of hydrogen desorption that determines the reaction rate. Hence, in case that we have two adsorption sites in a short distance, the mechanism of the reaction can be Tafel. This mechanism should also be examined in future work. Last but not least, it is important for a catalytic material to possess more than one adsorption sites, so that it can produce higher amounts of hydrogen.

In addition, we investigate metal dopants of 9 to 11 group of periodic table and Pb dopant (except for Ir and Pt mentioned before). From Figure 44, Ni has the best performance for  $V_S$  site. For some other dopants, especially Cu and Zn, S1 site shows efficient hydrogen adsorption ability close to thermoneutral. The majority of the dopants have values around 0.50 eV at S1 site. For S0 site the energy values are far from thermoneutral, starting from 0.50 eV to 1.50 eV. For the other hydrogen adsorption sites, we have a weaker interaction with hydrogen, with small deviations depending if the adsorption site is closer to the metal dopant or to the sulphur vacancy. There is a difference between the energy values among the metal dopants for the different adsorption sites.

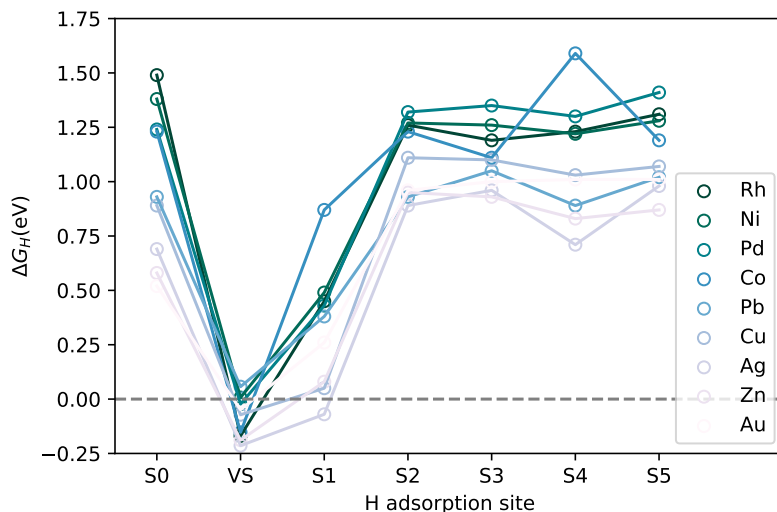


Figure 44: Hydrogen adsorption free energy ( $\Delta G_H$ ) for different adsorption sites for Metal (Rh, Ni, Pd, Co, Pb, Cu, Ag, Zn and Au)-doped  $\text{MoS}_2\text{-V}_S$  system.

For these metal-doped systems, the activation of the basal plane is close to the sulphur vacancy site and the closest sulphur adsorption site S1 of the basal plane. Especially at S1, their systems possess lower hydrogen adsorption free energies compared to the dopants of group 6-8 and 4-5 (Table 26 in Appendix).

### 5.2.1 Differential charge distribution

Considering as a reference system the  $\text{MoS}_2\text{-V}_S$ , we try to explain the charge contribution of each Mo substitution. In Appendix Table 23, we see the analysis on the differential charge distribution for the Metal-doped  $\text{MoS}_2\text{-V}_S$  systems. It is a quantitative way to express the charge distribution of the metal dopant within the structure. With blue and red color is the negative and positive charge respectively.

The metal dopants of group 4 and 5 (Nb, Mo, Zr, Pt, Ti, V, Ta and Hf) have a large charge distribution around the metal dopant, sulphur vacancy and neighbour sulphur atoms. The

negative charge is evident for these systems. The exceptions are Zr and Nb in which their charge is positive and localized in a spherical distribution around the metal dopant. These metals have quite similar hydrogen adsorption ability and values according to Figure 42. The sulphur site is active for them and the rest of the basal plane remains inert. Mo and Pt that are also referred in the same diagram, have values close to zero at  $V_S$ . Pt has a smaller charge distribution and there is more positive charge compared to the other structures.

For systems with metal dopants of group 6-8 of periodic table, we observe that for these metal dopants, the charge is smaller compared to the previous case and the distribution involves the metal dopant,  $V_S$  and the closest neighbour sulphur atoms. At the metal dopant we have a positive charge. In the center of the sulphur vacancy there is positive charge and around it is negative. This might explain the slightly less negative hydrogen adsorption free energy values at the  $V_S$  site in comparison to the previous cases. The neighbour sulphur sites S1 for all the cases have a negative charge. This might suggest the weaker interaction with hydrogen. The W dopant has a different charge distribution, a combination of the 4-5 group dopants with 6-8 ones, where the charge is located closer to the metal dopant and not on the sulphur atoms. As we move down on the same group the charge increases (Re, Ir, Os).

Finally, there are the systems with 9-11 group dopants. For the first and second row, the charge is located on metal dopant and sulphur vacancy site. The Ag and Au dopants have their main charge distribution at metal dopant and the closest neighbour sulphur atoms. Pt is an exception that has a charge distribution similar to 6-9 group metals, but an activity close to Mo. Pb has a wider charge distribution with more negative charge in its basal plane. Its activity for the different adsorption sites is close to the 9-11 group metals.

### 5.2.2 The $V_S$ adsorption site

We see that for this adsorption site 4 and 5 groups of periodic table as well as Mo, W and Pb the metal dopant locates in a position similar to Mo at pristine  $\text{MoS}_2$ . However, in all the other starting from 6 to 11 and Pb, the metal atom changes its position closer to one side (Table 28 in Appendix). For those from 6-8 group the reconstruction is in a smaller degree. Excepting M, W, Pb all the other systems possess negative hydrogen adsorption free energies (Table 26 in Appendix). Metals of 4 to 5 group that have  $\Delta G_H$  higher negative than required are not included in this trend, because they do not act as catalysts. These results are in agreement with Deng et al. [10] studies on metal doped 2H- $\text{MoS}_2$ . They observe that when hydrogen interacts weakly, the system has a small change in their structure and  $\Delta G_H$  is positive. Otherwise,  $\Delta G_H$  is negative and the metal dopant goes to one side away from the adsorption site.

### 5.2.3 The $S_0$ adsorption site

Considering their structural configurations after hydrogen adsorption in regards to their adsorption site, there are also some similarities between the metal dopants of each group.

Regarding to metal adsorption site (S0), (Table 29 in Appendix) we observe that for the metal dopants of 4 and 5 group of periodic table, hydrogen after its adsorption, prefers a position close to the metal dopant and away from the sulphur vacancy. There are no major changes in their structures, so that the metal dopant remains in a position similar to the Mo atom in pristine MoS<sub>2</sub> and each metal coordinates with 5 S atoms. There are some exceptions, so that Mo has its hydrogen in the V<sub>S</sub> adsorption site and Pt has a 3 fold symmetry. Especially for Pt, Ti, V, Ta and Hf their hydrogen adsorption free energy at this site is quite similar with their values at the sulphur sites, except V<sub>S</sub>. For Nb, Mo and Zr, the energy values are high positive, greater than the one of pristine MoS<sub>2</sub> of its basal plane, so that energy is needed to add hydrogen in the structure. This suggest that the metal attracts hydrogen strongly and locally.

For the metal dopants described on Figure 43, hydrogen changes position to the V<sub>S</sub> site and in a direction away from the metal dopant. The sulphur vacancy site has a greater effect on hydrogen, so that it changes position. A difference in the direction is observed on Re and W dopants, where hydrogen is still in V<sub>S</sub> adsorption site but towards the metal atom. The metal dopants position is slightly closer away from the V<sub>S</sub>, but there are not huge reconstructions. All the systems maintain the 5 fold symmetry of the metal dopants. Their hydrogen adsorption free energies are quite similar to V<sub>S</sub> adsorption sites (Table 26 in Appendix).

The metal dopants of 9-11 group and Pb of periodic table have the same hydrogen adsorption behaviour. Thus, hydrogen stays close to the metal dopant in a direction away from the V<sub>S</sub>. There are significant reconstructions to their systems, so that the metal dopant moves to a position towards one side, either away or close to V<sub>S</sub>. There is a change in coordination from 5 to 3 for Pd, Zn and Au dopants. All the other ones have a 5-fold symmetry. The hydrogen adsorption free energies are similar to those sulphur sites in a longer distance than S1 site. (Table 26 in Appendix)

#### 5.2.4 The S1 adsorption site

The metals of the first group (4-5 group of periodic table, Mo and Pt) have hydrogen on top and in a distance at S1 adsorption site. The metal remains in a position similar to Mo in pristine system, except from Pt, that it moves closer to S1 site. They maintain the 5 fold symmetry, as no bond breaks in their structures.

Then, there are the metal dopants from group 6 to 8 of periodic table. Hydrogen atom is on top of S1. There is no significant reconstruction, as the metal has a similar position to Mo in pristine system, however it is slightly moved toward S1 adsorption site. They also bond to five neighbour sulphur atoms.

Finally, 9-11 metals including Pb have a greater reconstructions compared to the previous cases. Hydrogen atom prefers a position above and in a distance away from S1 site. All systems have a 4 fold symmetry, breaking a bond between S1 and metal. The exceptions

are Co and Pd that maintain the 5 fold symmetry and Au with 3 neighbour S atoms. The metals change their position to one away from the S1 site (Table 30 in Appendix). This group has the lowest energy values. This might be explained as the bond breaking allows hydrogen to bond with sulphur with less energy needed (Table 26 in Appendix).

### 5.2.5 Hydrogen adsorption on $V_S$ and S1

In this case we have a similar effect as in single hydrogen adsorption at  $V_S$ . However, the reconstruction of the systems is in a greater degree for metals on 9-11 group of periodic table. The metal dopant moves to one side. In most systems it is away from the S1 adsorption site, changing its five-fold symmetry to four, except for Pt that moves closer to S1 and breaks the bond with  $V_S$  (Table 31 in Appendix).

We observe that for systems with a bond break and change of the metal position towards one side, the hydrogen adsorption ability becomes more efficient (Table 27 in Appendix). Theories suggest that because of the d-orbital nature of the metals and the dangling bonds appearance after breaking symmetry, hydrogen can bind better with the system [22]. Hence, further work needs to be done to explain the effect of bond breaking.

## 5.3 Hydrogen Coverage Effect for Metal-doped $\text{MoS}_2$ - $V_S$

We perform calculations to examine the hydrogen coverage effect for the Metal-doped  $\text{MoS}_2$ - $V_S$  system. Initially, a hydrogen atom was adsorbed in the  $V_S$  site. Then, we add a second one at S1 site (Table 31 in Appendix). The S1 site was preferred, because based on the previous calculations, it is the sulphur adsorption site with values close to thermoneutral for many metal-doped systems, especially the ones with similar behaviour to Ni dopant.

In Figure 45, the differential hydrogen adsorption free energies for S1 site are depicted (Table 27 in Appendix). Also, the hydrogen adsorption free energies for S1 and  $V_S$  are mentioned for comparison.

It derives that Ni dopant has the best performance compared to all the other dopants for  $V_S$  site ( $\Delta G_H = 0.007$  eV). In addition, when a second hydrogen is introduced at S1 site, it is easier to be adsorbed by the system when a first one has already been adsorbed at  $V_S$  ( $\Delta G_H^{diff} = 0.08$  eV). The hydrogen coverage effect has an important role for HER, because an efficient catalyst must remain active after the first hydrogen adsorption and have many adsorption sites to produce hydrogen. Thus, the second hydrogen can be used for the first step of the reaction or for hydrogen molecule desorption via Tafel mechanism in the second step of the reaction.

Moreover, Pd shows good performance for both mentioned cases. However, it is scarce and expensive for HER reaction, compare to the other metal dopants. For Cu, Ag and Zn that showed the best performance at S1 site,  $\Delta G_H^{diff}$  for S1 is more negative, so that hydrogen binds strongly in the catalyst surface and the system is no more efficient for HER.

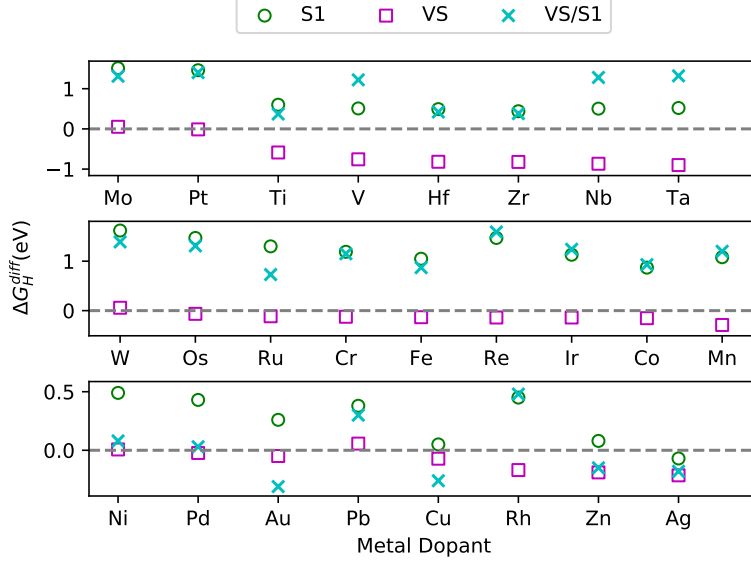


Figure 45: Differential hydrogen adsorption free energy ( $\Delta G_H^{diff}$ ) for S1 adsorption sites and hydrogen adsorption free energy ( $\Delta G_H$ ) for S1 and  $V_S$  sites of Metal-doped  $\text{MoS}_2\text{-}V_S$ .

For the 4-5 group metals of the periodic table, including Mo and Pt dopants, when we add a second hydrogen, the  $\Delta G_H^{diff}$  takes values slightly lower or the same with the energy needed to adsorb a single hydrogen at S1 site. This means that the existence of an adsorbed hydrogen, for these doped structures, does not have an important impact to the system. Exceptions are V, Nb and Ta that have higher  $\Delta G_H^{diff}$  values in comparison to  $\Delta G_H$  at S1. The adsorbed hydrogen has a repulsive effect, so that the system needs more energy to introduce a second hydrogen after hydrogen adsorption at  $V_S$  than in single hydrogen adsorption.

For the 6-8 group metals of the periodic table, for W, Os, Ru, Cr and Fe dopants,  $\Delta G_H^{diff}$  has slightly smaller values than  $\Delta G_H$  at S1. However, for Re, Ir, Co and Mn, it has slightly greater than  $\Delta G_H$  at S1. We can say that for these metal dopants, the existence of an adsorbed hydrogen does not affect the system hydrogen adsorption ability.

Finally, for 9-11 group metals, including Pb, we see that for all the cases the energies are closer to thermoneutral within the range of 0.5eV to -0.5eV. The existence of a hydrogen adsorbed at the  $V_S$  site benefits the introduction of a second one at S1 site, so that the needed energy is lower than  $\Delta G_H$  at S1 site and close to  $V_S$  for the most cases (Ni, Pd, Cu, Zn and Ag). Ni dopant is the most affected by the existence of an adsorbed hydrogen as the energy difference between  $\Delta G_H$  (0.49 eV) and  $\Delta G_H^{diff}$  (0.076) at S1 is great and is the most efficient one for both cases.

We have to conclude that hydrogen coverage effect is an important parameter for a catalyst. It defines the turnover frequency, the amount of hydrogen atoms interacting with catalyst per area and unit of time. For example, it is known that Pt(111) surface has  $\Delta G_H$  close to

zero up to 1 ML, while Mo-edge on MoS<sub>2</sub> has a  $\Delta G_H$  equal to 0.08 eV at 0.25 ML. So, Pt requires four times more adsorbed hydrogens in its surface in order to reach its high activity. The activation of other sites in MoS<sub>2</sub> can increase its hydrogen production. Consequently, Ni-MoS<sub>2</sub>-V<sub>S</sub> systems is the only one that has a value close to Pt(111) at  $\theta_H = 1$  ML, but being in a lower coverage of 0.11 ML. In addition, the introduction of a hydrogen in the sulphur vacancy site, activates the neighbouring S adsorption site, so more hydrogen can be produced. Especially, for basal plane systems there is space for further creation of defects combinations, so that a higher hydrogen production can be achieved.

## 5.4 Electronic Density of States for TM-MoS<sub>2</sub>-V<sub>S</sub>

The TDOS of undoped MoS<sub>2</sub>-V<sub>S</sub> (Figure 46(a)) and for W doped (Figure 46(b)) resemble. The defects states are introduced near the conduction band. The role of sulphur vacancy is prominent in their electronic structures as it is responsible for the gap states. Because Mo has a slightly greater size than W, its defect state is slightly closer to the Fermi level. This is also discussed in Li et al work considering strain application [49]. The band gap in both cases becomes more narrow and the semiconducting character is preserved.

Considering the d-band model [56], these new gap states above Fermi level are bonding states, so that hydrogen molecule is attracted by the system. However, they are in a distance from the Fermi level so that the interaction is weak, in agreement with the slightly positive  $\Delta G_H$  values.

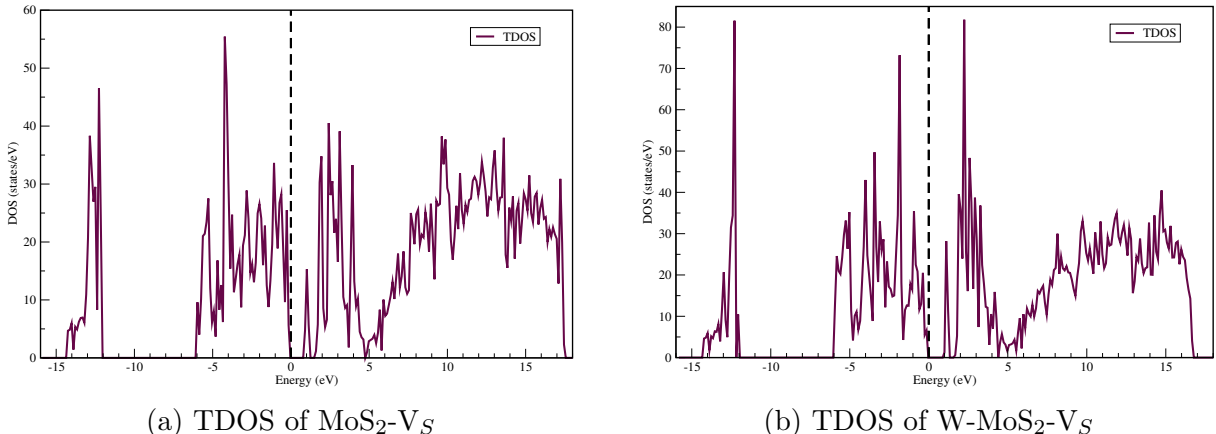


Figure 46: Electronic structures of TM-MoS<sub>2</sub>-V<sub>S</sub> before hydrogen adsorption.

Then, Ni, Pt, Pd and Au dopants have an excellent HER performance, with the first three having  $\Delta G_H$  close to zero. We observe a metallic character, with density of states filling the band gap. However, for Ni (Figure 47(a)), Pt (Figure 47(a)) and Pd (Figure 47(a)) doped systems, there are states below and above the Fermi level, equally in number for each side, leaving a small band gap. This might suggest that bonding and antibonding states counteract each other, so that  $\Delta G_H$  is close to thermoneutral. However, for Au dopant (Figure 47(d)),

the system possess a greater amount of peaks of bonding states, so the attraction is greater and  $\Delta G_H$  is slightly more negative.

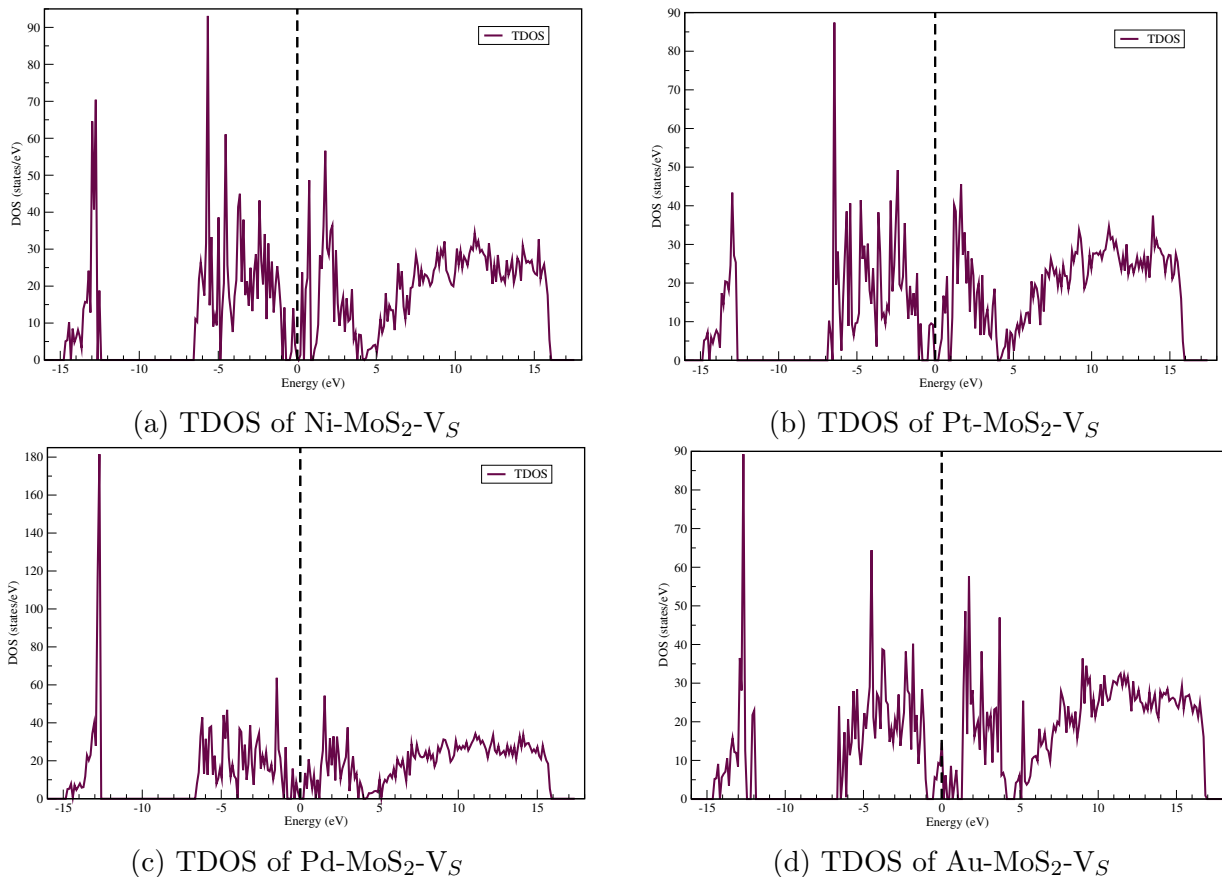
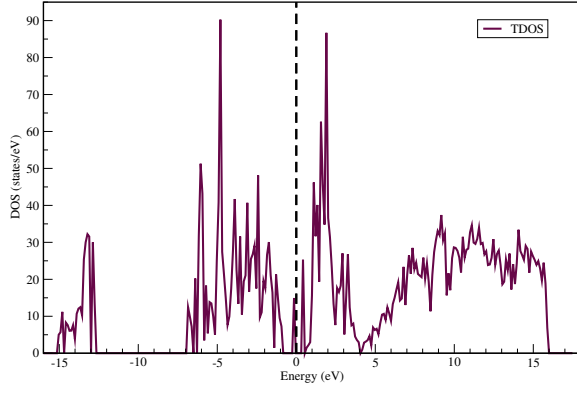


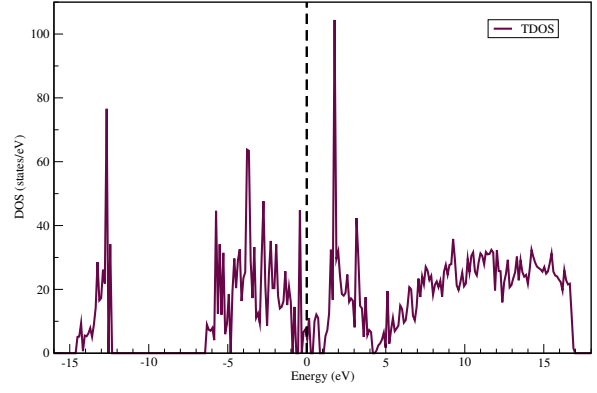
Figure 47: Electronic structures of TM-MoS<sub>2</sub>-V<sub>S</sub> before hydrogen adsorption, where TM is Ni, Pt, Pd and Au.

Figures 48, 49 and 50 show the electronic density of states of Os (Figure 48(a)), Cu (Figure 48(b)), Ru (Figure 48(c)), Cr (Figure 48(d)), Fe (Figure 49(a)), Re (Figure 49(b)), Ir (Figure 49(c)), Co (Figure 49(d)), Rh (Figure 50(a)), Ag (Figure 50(b)) and Mn (Figure 50(c)) dopants. Their hydrogen adsorption ability is better in regards to MoS<sub>2</sub> Mo-edge, but they bind hydrogen strongly to their adsorption sites. From their electronic structure, we observe that they have a metallic character and the band gap becomes even more narrow. The strain introduced by the dopants is enough to move the defect states close to Fermi level, so that there are states crossing it.

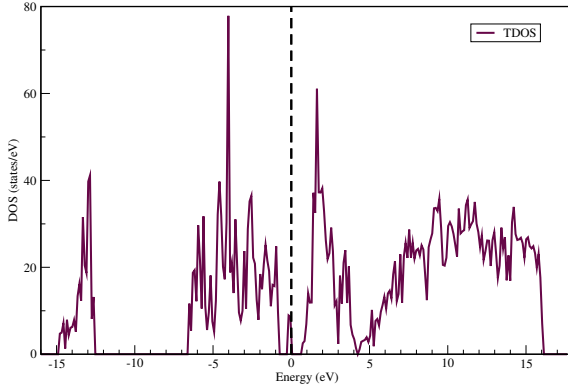
These doped systems have a great amount of states above Fermi level, so that hydrogen interacts strongly with them, based on the d-band model. Hence, they possess high negative energy values.



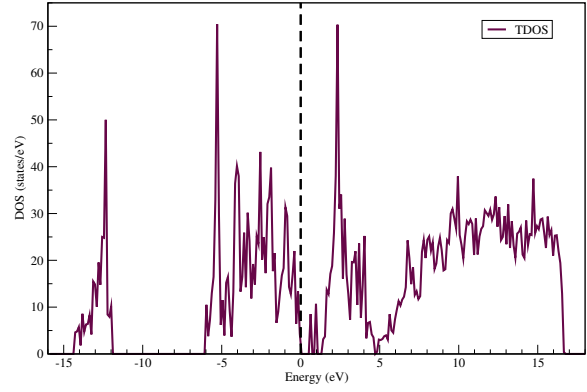
(a) TDOS of Os-MoS<sub>2</sub>-V<sub>S</sub>



(b) TDOS of Cu-MoS<sub>2</sub>-V<sub>S</sub>

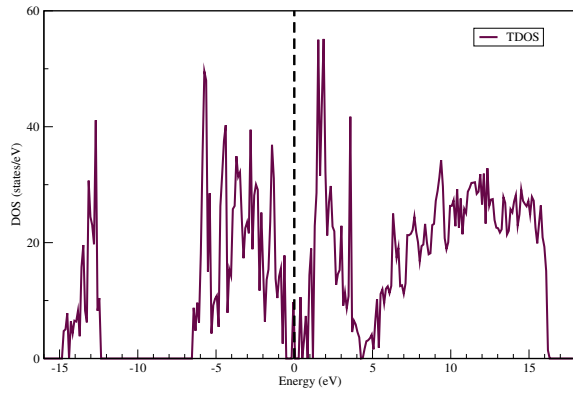


(c) TDOS of Ru-MoS<sub>2</sub>-V<sub>S</sub>

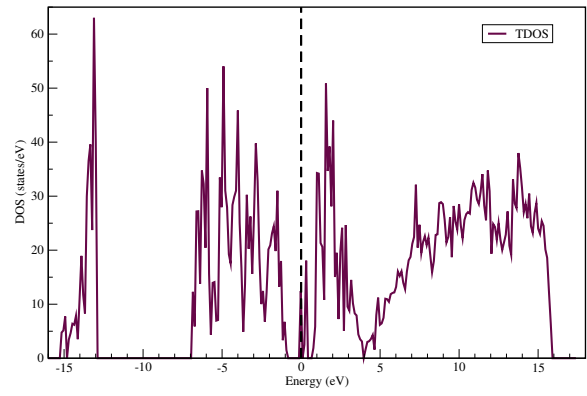


(d) TDOS of Cr-MoS<sub>2</sub>-V<sub>S</sub>

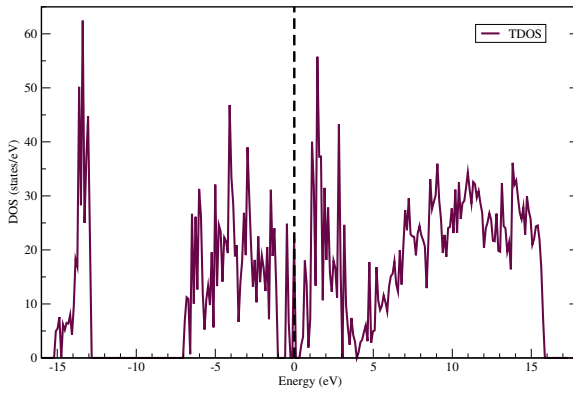
Figure 48: Electronic structures of TM-MoS<sub>2</sub>-V<sub>S</sub> before hydrogen adsorption, where TM is Os, Cu, Ru and Cr.



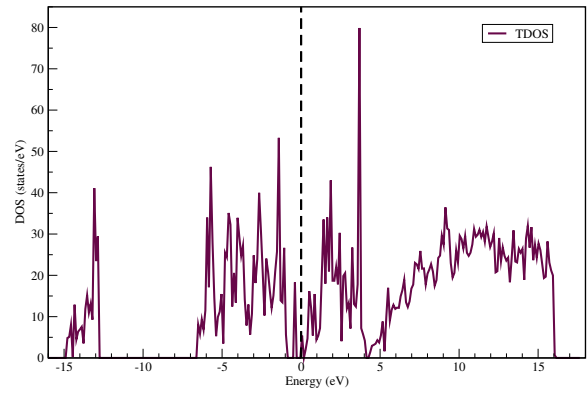
(a) TDOS of Fe-MoS<sub>2</sub>-V<sub>S</sub>



(b) TDOS of Re-MoS<sub>2</sub>-V<sub>S</sub>



(c) TDOS of Ir-MoS<sub>2</sub>-V<sub>S</sub>



(d) TDOS of Co-MoS<sub>2</sub>-V<sub>S</sub>

Figure 49: Electronic structures of TM-MoS<sub>2</sub>-V<sub>S</sub> before hydrogen adsorption, where TM is Fe, Re, Ir and Co.

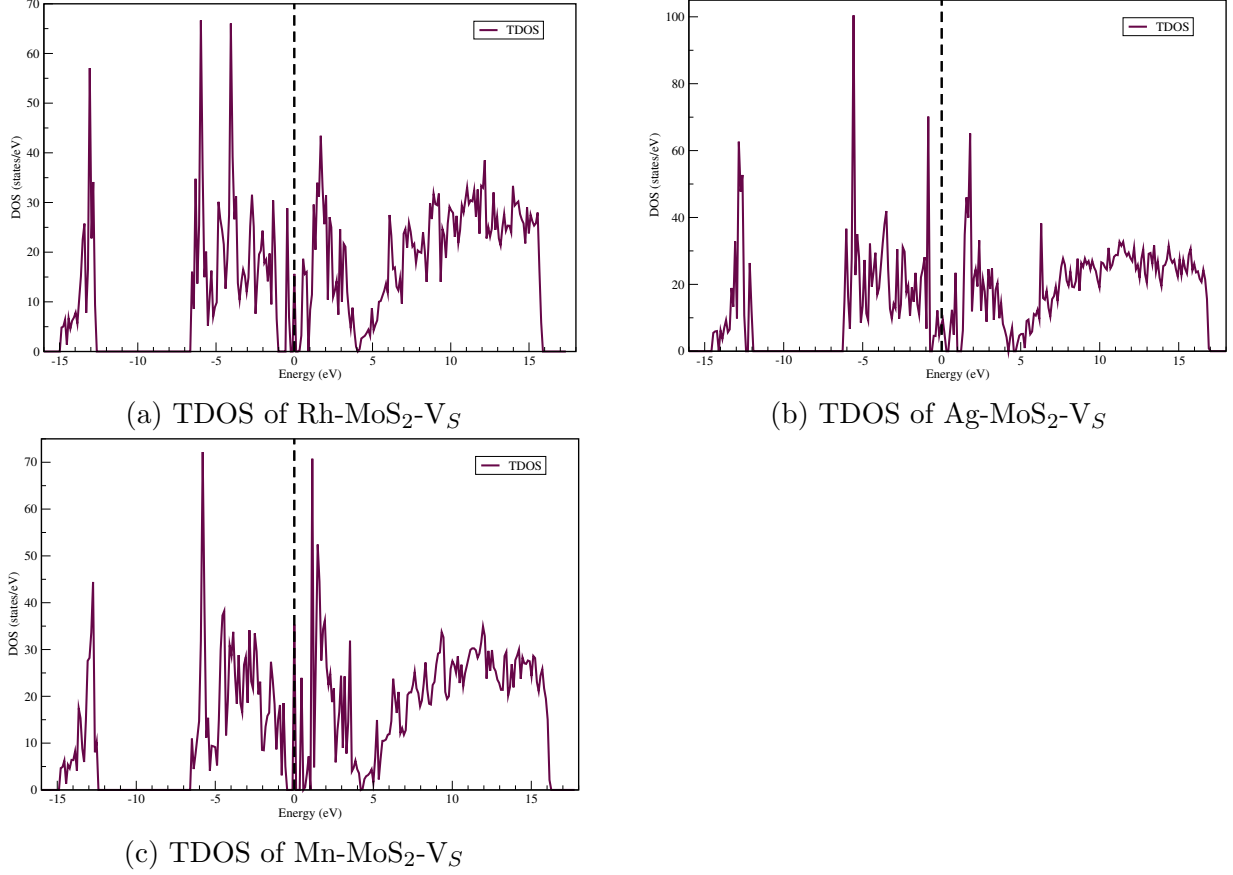


Figure 50: Electronic structures of TM-MoS<sub>2</sub>-V<sub>S</sub> before hydrogen adsorption, where TM is Rh, Ag and Mn.

## 5.5 Activity-Stability Relationship

Finally, we examine the relationship between the activity and stability descriptors. The hydrogen adsorption and H<sub>2</sub>S desorption compete each other during HER. When a proton is adsorbed by the catalyst surface, it can form either H<sub>2</sub> molecule that leaves the catalyst surface or a H<sub>2</sub>S molecule when the HS interaction with the system is weak. In the last case, catalyst starts to dissolve and it is no more efficient for the reaction.

The following equation is used to express the binding energy of HS,  $\Delta E_{HS}$

$$\Delta E_{HS} = E_{TM-MoS_2-V_S-HS} + E_{H_2}/2 - E_{TM-MoS_2-V_S} - E_{H_2S} \quad (50)$$

where:  $E_{TM-MoS_2-V_S-HS}$  is the total energy of TM-MoS<sub>2</sub>-V<sub>S</sub> system with a HS adsorbed,  $E_{H_2}$  is the total energy of H<sub>2</sub> molecule,  $E_{TM-MoS_2-V_S}$  is the total energy of TM-MoS<sub>2</sub>-V<sub>S</sub> system and  $E_{H_2S}$  is the total energy of H<sub>2</sub>S molecule (-11.195 eV).

For this reason, a stability descriptor, the HS free energy ( $\Delta G_{HS}$ ) is used. If it has a positive value, the system dissolves. Otherwise, for negative values, it is a robust material

[23].

The HS free energy ( $\Delta G_{HS}$ ) is defined as :

$$\Delta G_{HS} = \Delta E_{HS} + \Delta E_{ZP} - T\Delta S_H \quad (51)$$

where:  $\Delta E_{ZP}$  is the energy difference between the gas and adsorbed phase of hydrogen,  $T$  is temperature and  $\Delta S_H$  is the entropy difference between the gas and adsorbed phase of hydrogen. In the table below, there are the calculated values of the transition metals that have  $\Delta G_H$  between -0.45 eV and 0.45 eV, which is the upper limit area for an efficient catalyst in MoS<sub>2</sub> systems. We choose this value because it expresses the  $\Delta G_H$  value for S edge of MoS<sub>2</sub>, involving a greater amount of systems compared to the Mo edge of  $\Delta G_H$  equals to 0.06 eV, according to C. Tsai et al. work [25].

Table 18: Hydrogen adsorption free energy ( $\Delta G_H$ ) and HS free energy ( $\Delta G_{HS}$ ) for TM-MoS<sub>2</sub>-V<sub>S</sub> system.

Metal dopant	$\Delta G_H$	$\Delta G_{HS}$ (eV)
Ni	0.007	-1.65
Pt	-0.012	-1.35
Pd	-0.023	-1.46
Au	-0.049	-1.38
W	0.052	-2.05
Mo	0.058	-2.07
Os	-0.065	-2.04
Cu	-0.072	-1.74
Cr	-0.124	-2.30
Fe	-0.133	-2.28
Re	-0.139	-2.18
Ir	-0.139	-1.68
Co	-0.153	-1.90
Rh	-0.169	-1.77
Ag	-0.214	-1.51
Mn	-0.290	-2.50

For  $\Delta G_{HS}$ , when we move closer to zero the interaction between H and S in the adsorption site becomes weaker. When the system has  $\Delta G_{HS}$  equal or greater than zero, it starts to dissolve. In Table 18,  $\Delta G_{HS}$  values are negative suggesting robust materials for HER. Then, inspired by the analysis on the activity and stability descriptors on transition metal dichalcogenides for HER, according to studies [23], we construct the following plot of the the activity ( $\Delta G_H$ ) and stability ( $\Delta G_{HS}$ ) descriptors (Figure 51). As we move  $\Delta G_H$  towards zero, the more efficient the HER activity becomes.

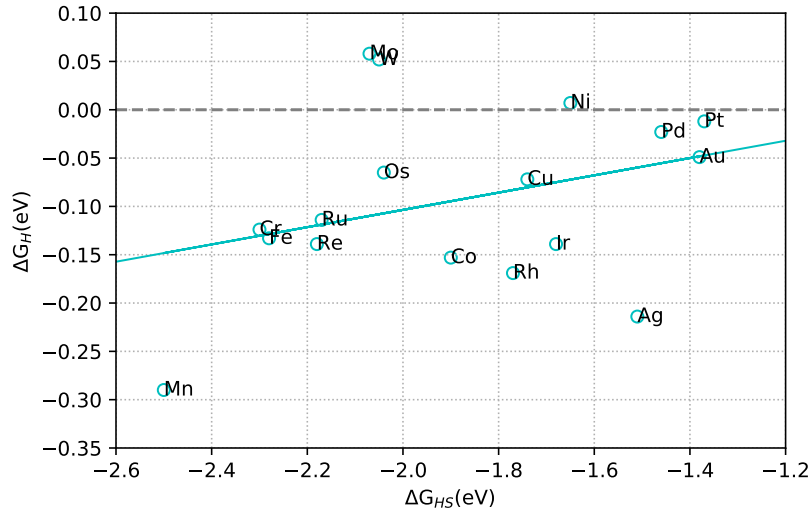


Figure 51: Hydrogen adsorption free energy ( $\Delta G_H$ ) versus HS free energy ( $\Delta G_{HS}$ ) for TM-MoS<sub>2</sub>-V<sub>S</sub> systems.

We observe a relationship between the two descriptors according to Figure 51. The Ni, Pt and Pd are close to zero, having one of the smallest  $\Delta G_{HS}$  values and be the most efficient for HER. Then, dopants with less efficient performance follow and at the end is Mn that has the stronger HS binding and the lowest HER performance. We can conclude that the weaker the HS binding of the system is, within a framework that the system does not dissolve, the more efficient for HER. This result is in agreement with an inverse linear relationship between  $\Delta G_H$  and  $\Delta G_{HS}$  that also appears for transition metal dichalcogenides MX<sub>2</sub> systems, where M is the transition metal and X the chalcogen atom. When replacing M with other transition metal dopants and keep the same X for all the system, we observe the same relationship between the descriptors [25].

## 6 Conclusions

We performed calculations using a geometry optimized monolayer MoS<sub>2</sub> supercell as a reference system to examine its hydrogen adsorption ability. Its basal plane was found to be catalytically inert. Then, we studied the impact on hydrogen adsorption ability after introducing defects and dopants on the basal plane of MoS<sub>2</sub>. Firstly, the single atom metal doping with Ni on MoS<sub>2</sub> basal plane was studied. A bond break happens between Ni and S atom that adsorbs hydrogen. The hydrogen adsorption free energy is negative and far from thermoneutral. The introduction of a sulphur vacancy on the basal plane can activate its hydrogen adsorption ability. The combination of a sulphur vacancy and a neighbour Ni dopant was the focus of this work. We observe a relocation of Ni atom towards one side and the hydrogen adsorption free energy has a value close to zero. The above results are in agreement with other theoretical works.

Studying the density of states of the aforementioned systems, we observe that for MoS<sub>2</sub>-V<sub>S</sub>, there are new gap states near the conduction band. After hydrogen adsorption, they move closer to the Fermi level. For Ni-MoS<sub>2</sub>, there are more gap states introduced near the Fermi level and with hydrogen adsorption they relocate closer to it. The combination of Ni and V<sub>S</sub> changes the system character to metallic. The distribution between bonding and antibonding states in the DOS, is similar in amount above and below the Fermi level, so that a  $\Delta G_H$  is close to zero. The appearance of metallic states around Fermi level has also been mentioned for other efficient HER catalysts and is responsible for their high performance.

The existence of other adsorption sites near the active V<sub>S</sub> site of the basal plane for Ni-MoS<sub>2</sub>-V<sub>S</sub> was searched. The areas closer to Ni have a stronger interaction with hydrogen, while those close to V<sub>S</sub> have a weaker interaction. However, the activation of the neighbour sulphur sites remains weak, except from the site (S1) closest to both Ni and V<sub>S</sub>. Comparing the Ni-MoS<sub>2</sub>-V<sub>S</sub> system with pristine, Ni-doped and with a V<sub>S</sub>, we see that it has the best performance at all of its sites and especially for S1. In regard to hydrogen coverage effect the S1 site has an energy value close to thermoneutral for Ni-MoS<sub>2</sub>-V<sub>S</sub>. So it is still active for HER after the first hydrogen adsorption on V<sub>S</sub> at S1. Hydrogen lowers the energy values closer to zero for all sulphur adsorption sites.

Then, we investigated the step of hydrogen desorption. Tafel mechanism might apply if the two hydrogen atoms adsorbed on V<sub>S</sub> and S1 are in a close distance. Future work needs to further investigate this. The Heyrovsky step is a potential mechanism for these systems. Our calculations suggest that a second hydrogen at V<sub>S</sub> site can bind with already adsorbed hydrogen and create a hydrogen molecule in a distance from the adsorption site. This also was compared with MoS<sub>2</sub>-V<sub>S</sub> that is an active HER catalyst according to the condition  $\Delta G_H \approx 0$ , but we found that the interaction is so weak that a hydrogen molecule is not formed. Nudged Elastic Band (NEB) method can be applied to further investigate this mechanism.

In regard to the formation of Ni-MoS<sub>2</sub>-V<sub>S</sub> system, a sulphur vacancy requires a small amount of energy to be formed and it is a common defect in MoS<sub>2</sub> systems. Considering that under industrial conditions other molecules from solution and intermediates can interact with S and isolated it from MoS<sub>2</sub>, the system employing this defect is closer to reality. The single atom doping with Ni requires more energy than the simultaneous creation of V<sub>S</sub> and Ni defects. The replacement of Mo with a Ni dopant when a V<sub>S</sub> already exists, requires even less energy than the previous two cases.

Comparisons with several metal dopants were performed. A volcano curve was constructed, where Ni-MoS<sub>2</sub>-V<sub>S</sub> is on top, having the highest reaction rate. Various sites of the basal plane were investigated for hydrogen adsorption ability.

For dopants of 4-5 group of the periodic table, the structure does not change after doping. Activity is limited to the V<sub>S</sub> adsorption site and its performance is poor. For the majority of metals group of 6-8, the reconstruction is limited to a small displacement of the metal dopant to one side. Their activity involves metal dopant at S0 and V<sub>S</sub> sites.

Most of the systems with metal dopants of 9-11 group experience high reconstruction, involving bond breaking between S atom that adsorbs hydrogen and metal dopant and change of the position of the metal. Basal plane is active both for V<sub>S</sub> and S1. These dopants tune the system to excellent HER activity.

The hydrogen coverage effect eliminates all metal dopants except for Ni and Pd. However, Pd despite being excellent as catalyst, is expensive for industrial use. The activation of other adsorption sites, especially in the presence of hydrogen, is vital for HER. The catalyst is not poisoned by the adsorbed reactant and the HER continues producing more hydrogen.

From the study of total DOS, the distribution and the amount of bonding and antibonding states has a key role. For the doped systems with excellent performance, DOS peaks below and above Fermi level exists, in a close distance and equal amount. The systems with DOS bonding states above the Fermi level show stronger interaction with hydrogen.

Finally, the stability of these systems was examined. We find that the TM-MoS<sub>2</sub>-V<sub>S</sub> systems are robust having negative  $\Delta G_{HS}$  values. A relationship was found between stability and activity descriptors, so that the weaker the HS binding to the MoS<sub>2</sub> system, the more active it is for HER, in agreement with other transition metal dichalcogenides studies.

Future research should examine the increase of metal doping and sulphur vacancies. Calculations with further replacements of neighbouring Mo atoms to the sulphur vacancy need to be explored.

To conclude, we confirm that  $V_S$  can activate the basal plane of  $\text{MoS}_2$ . Single atom doping with Ni can have the same results, however it results in a stronger interaction with hydrogen than needed. The combination of Ni dopant and  $V_S$  can tune the activity closer to thermoneutral. We confirm that  $\Delta G_H$  close to zero, is an essential condition, however it cannot determine alone the efficiency of a HER catalyst. Adsorption sites and hydrogen coverage effects have a key role. Other adsorption sites are required to continue the process either by combining with existing adsorbed hydrogen and form molecules or by new reactions that occur increasing the production of hydrogen. The hydrogen coverage effect determines if the catalyst will be poisoned by the adsorption of a hydrogen or if it will increase its activity in the neighbour sites. The dopants with poor HER performance are the metals of 4-5 group of periodic table, the metals of 6-8 group are mediocre and the majority of metals of 9-11 have an excellent performance. Comparing with Pt, Ni-MoS<sub>2</sub>- $V_S$  is equal in efficiency and functions in lower hydrogen coverages. The d-band model might explain the hydrogen adsorption ability of these systems, as the amount and location of bonding and antibonding states can tune the hydrogen binding in the catalyst adsorption site.

## 7 Appendix

### 7.1 H<sub>2</sub> Energy Convergence Calculations

We perform energy convergence calculations for H<sub>2</sub>. The plane wave cutoff was set to 250 eV and a 1x1x1 Monkhorst Pack k-point-mesh was used. We change the distance between the two hydrogen atoms ( $d_{H-H}$ ) from 0.67 Å to 0.83 Å.

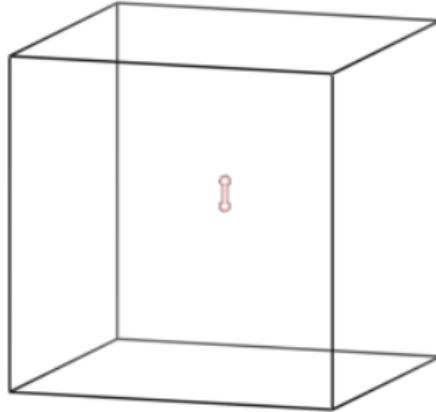


Figure 52: Geometry Optimized structure of H<sub>2</sub> in a box.

The Table 19 shows the total energy values for each distance parameter at 250 eV plane wave energy cutoff. A polynomial fit was used to calculate the bond length, which was found 0.759 Å, in agreement with the experimental value of 0.75 Å[87].

Table 19: Distance between the two hydrogen atoms and their estimated total energy.

$d_{H-H}$ (Å)	$E_{tot}$ (eV)
0.67	-6.696105
0.69	-6.696131
0.71	-6.696089
0.73	-6.696153
0.75	-6.696157
0.77	-6.696178
0.79	-6.696154
0.81	-6.696132
0.83	-6.696108

Using the bond length of 0.759 Å and the 250eV plane wave energy cutoff, the binding energy of H<sub>2</sub> molecule is -6.696 eV.

## 7.2 H<sub>2</sub>S Energy Convergence Calculations

We perform calculations for H<sub>2</sub>S. A plane wave energy cutoff of 400 eV and a 1x1x1 Monkhorst pack k-point-mesh were used. The geometry optimized structure is presented below in Figure 53. Its lattice parameters and total energy of the system are referred in Table 20. They are in agreement with experimental data with  $\theta_{H-S-H} = 92.11^\circ$  and  $d_{H-S} = 1.34 \text{ \AA}$ [87].

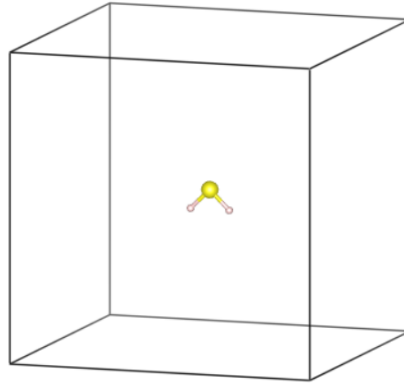


Figure 53: Geometry optimized structure of H<sub>2</sub>S molecule in a box.

Table 20: Structural and energetic parameters of H<sub>2</sub>S.

$d_{H-S} (\text{\AA})$	1.35
$\theta_{H-S-H} (^{\circ})$	91.62
$E_{tot} (\text{eV})$	-11.19461118

### 7.3 Mo(bcc) Energy Convergence Calculations

We performed energy convergence calculations for Mo body-centered cubic (bcc) system, which belongs to the  $Im\bar{3}m$  space group (Figure 54). Consequently, the positions of its atoms are defined by the following primitive vectors:

$$\mathbf{a}_1 = -\frac{1}{2}a\mathbf{x} + \frac{1}{2}a + \frac{1}{2}a\mathbf{z} \quad (52)$$

$$\mathbf{a}_2 = \frac{1}{2}a\mathbf{x} - \frac{1}{2}a\mathbf{y} + \frac{1}{2}a\mathbf{z} \quad (53)$$

$$\mathbf{a}_3 = \frac{1}{2}a\mathbf{x} + \frac{1}{2}a\mathbf{y} - \frac{1}{2}a\mathbf{z} \quad (54)$$

and the basis set is :

$$\mathbf{b}_1 = 0 \quad (55)$$

where  $a$  is the lattice parameter.

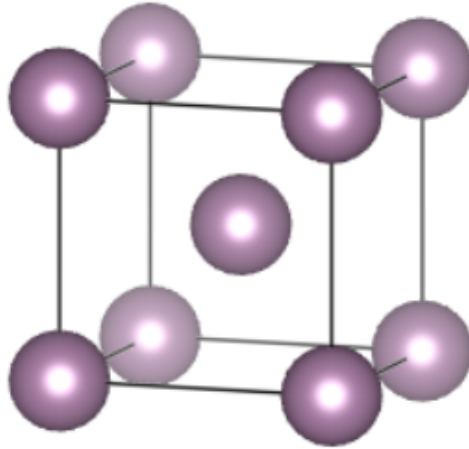
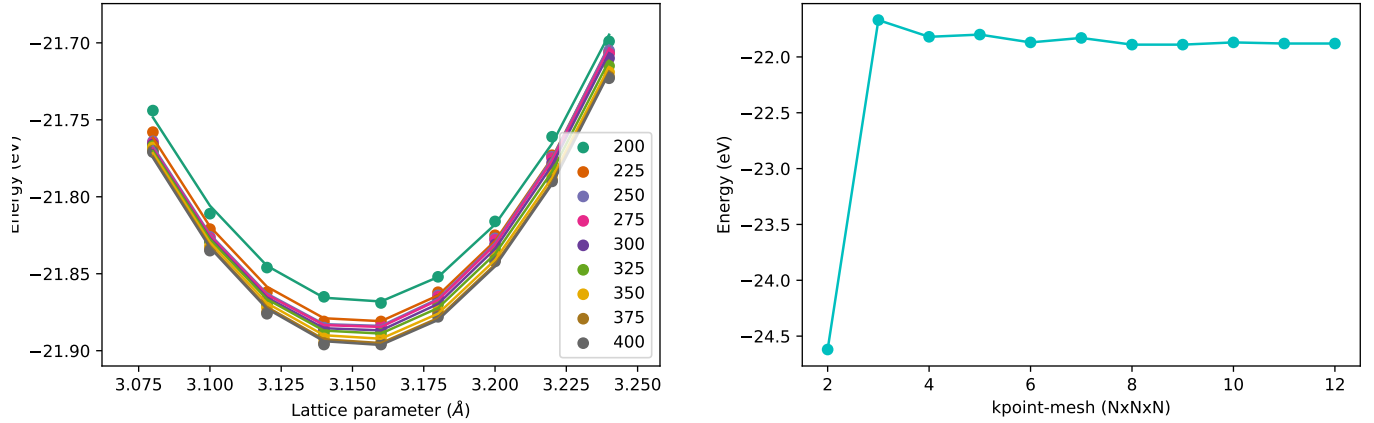


Figure 54: Primitive cell of Mo(bcc) consisted of two atoms

Firstly, we tested the total energy of Mo(bcc) primitive cell in regard to the lattice parameter  $a$ , for various plane wave energy cutoffs. The values of lattice parameter changed from  $3.08 \text{ \AA}$  to  $3.24 \text{ \AA}$ , with step  $0.02 \text{ \AA}$ . The Monkhorst-Pack kpoint-mesh was kept constant to  $9 \times 9 \times 9$ .

According to diagram 55(a), which depicts the total energy in respect to lattice parameter for different plane wave energy cutoffs, after  $250 \text{ eV}$  the total energy of Mo starts to converge.



(a) Total energy (eV) versus lattice parameter  $a$  ( $\text{\AA}$ ) for various plane wave energy cutoffs for Mo (bcc). (b) Total energy (eV) versus kpoint-mesh for 250 eV energy wave cutoff for Mo (bcc).

Figure 55: Energy convergence calculations for Mo(bcc) primitive cell.

By fitting a second degree polynomial ( $y = ax^2 + bx + c$ ), we calculated the lattice parameter for each plane wave energy cutoff. Then, considering the lattice parameter, we used the first derivative equal to zero ( $dy/dx = 0 \Rightarrow 2ax + b = 0$ ) to obtain the total energy. In the table below, the calculated lattice parameter and total energy for each plane wave energy cutoff are presented.

Table 21: Calculated values for the lattice parameter and total energy for each plane wave cutoff energy cutoff on Mo(bcc) system.

Plane wave energy cutoff (eV)	Lattice parameter ( $\text{\AA}$ )	Energy(eV)
200	3.153	-21.870
225	3.152	-21.882
250	3.151	-21.885
275	3.151	-21.886
300	3.151	-21.888
325	3.152	-21.891
350	3.152	-21.894
375	3.153	-21.896
400	3.153	-21.897

After 250 eV, the calculations start to converge at -21.89 eV, with a lattice parameter of 3.151  $\text{\AA}$ , in agreement with the experimental value of 3.15  $\text{\AA}$  [88]. Consequently, using these values for the lattice parameter and cutoff, we performed calculations and found the minimum energy -21.886 eV, so that the energy per atom is -10.943 eV in Mo(bcc) cell. Also,

performing kpoints convergence test, we see from Figure 55(b) that 9x9x9 kpoint-mesh is sufficient to describe the system.

## 7.4 Ni(fcc) Energy Convergence Calculations

We performed energy convergence calculations for Ni face-centered cubic (fcc) primitive cell, which belongs to the  $Fm\bar{3}m$  space group (Figure 56). Consequently, the positions of its atoms are defined by the following primitive vectors:

$$\mathbf{a}_1 = -\frac{1}{2}a\mathbf{x} + \frac{1}{2}a\mathbf{z} \quad (56)$$

$$\mathbf{a}_2 = \frac{1}{2}a\mathbf{x} + \frac{1}{2}a\mathbf{z} \quad (57)$$

$$\mathbf{a}_3 = \frac{1}{2}a\mathbf{x} + \frac{1}{2}a\mathbf{y} \quad (58)$$

and the basis set is :

$$\mathbf{b}_1 = 0 \quad (59)$$

where  $a$  is the lattice parameter.

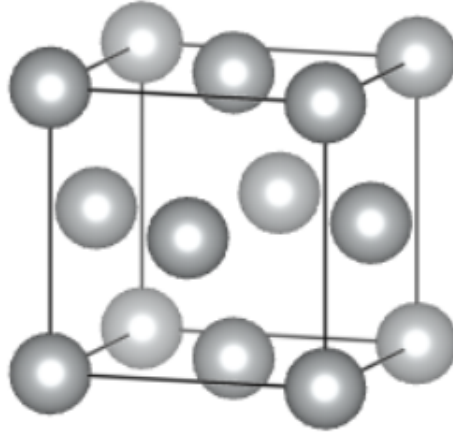
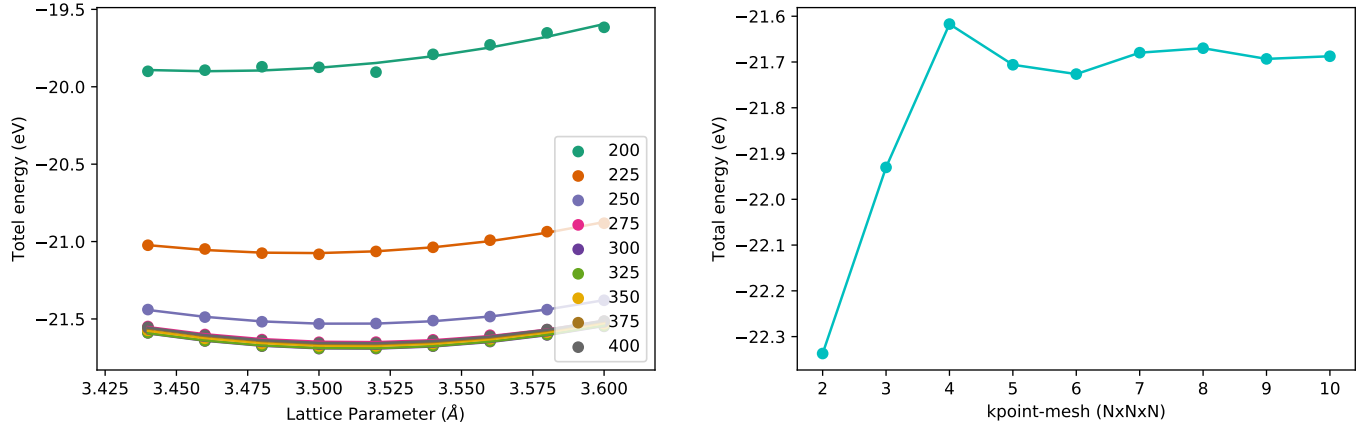


Figure 56: Primitive cell of Ni (fcc) consisted of four atoms

Then, in a similar way as before, we performed convergence test for Ni(fcc) primitive cell. This time the lattice parameter changed from 3.44 Å to 3.60 Å, with step 0.02 Å. The Monkhorst-Pack kpoint-mesh was kept constant to 9x9x9. From 300 eV the system starts to converge, according to Figure 57(a).



(a) Total energy (eV) versus lattice parameter  $a$  (Å) for various plane wave energy cutoffs for Ni(fcc). (b) Total energy (eV) versus kpoint-mesh for 300eV plane wave energy cutoff for Ni(fcc).

Figure 57: Energy convergence calculations for Ni(fcc) primitive cell.

Table 22: Calculated values for lattice parameter and total energy for each plane wave energy cutoff on Ni(fcc) system.

Plane wave energy cutoff(eV)	Lattice parameter (Å)	Energy(eV)
200	3.462	-19.900
225	3.494	-21.075
250	3.509	-21.532
275	3.513	-21.650
<b>300</b>	<b>3.512</b>	<b>-21.693</b>
325	3.512	-21.690
350	3.512	-21.675
375	3.513	-21.663
400	3.512	-21.657

Using 3.512 Å as lattice parameter for cutoff 300 eV, which is in agreement with the experimental value of 3.50 Å [88], we found the minimum energy -21.6936 eV, so that the energy per atom for Ni(fcc) primitive cell is -5.42 eV. Hence, from the optimized configuration for Ni(fcc), we performed kpoints convergence test and from Figure 57(b) we observe that 9x9x9 kpoint mesh is suitable to describe the Ni(fcc) system.

Table 23: Differential Charge Density for Metal-doped  $\text{MoS}_2\text{-V}_5$  system. With blue and red color are the negative and positive charges respectively.

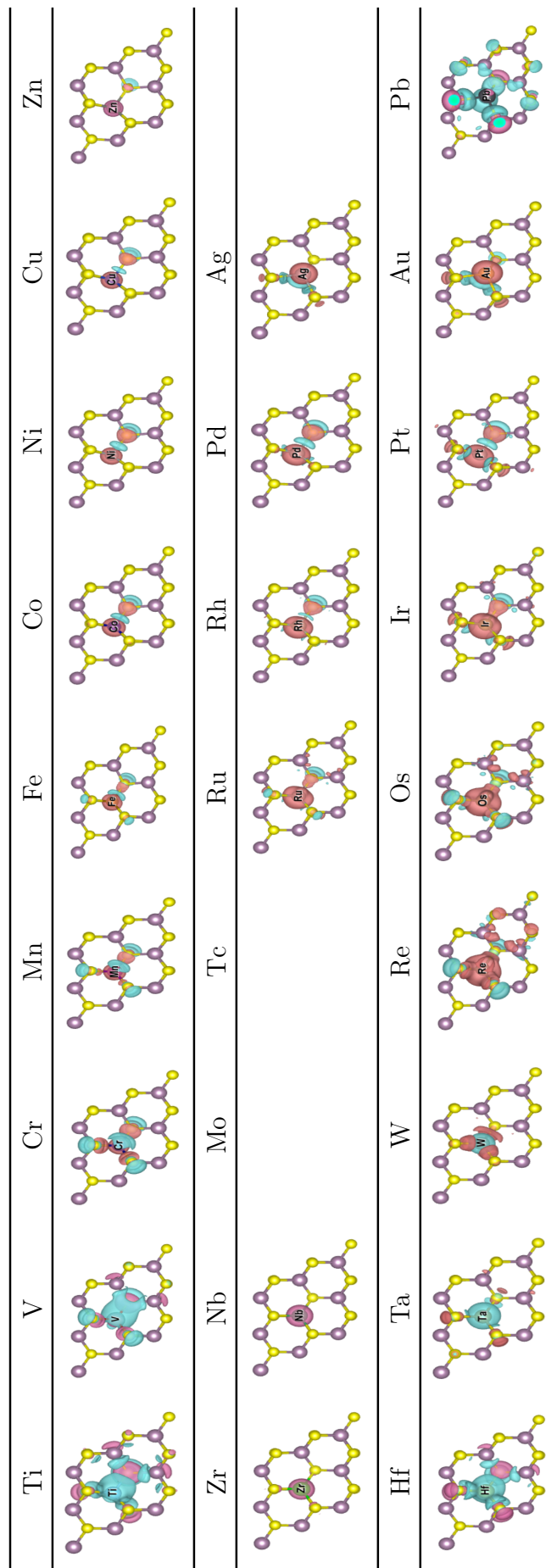


Table 24: Structural configurations and hydrogen adsorption free energies ( $\Delta G_H$ ) for different sulphur adsorption sites of the basal plane of MoS<sub>2</sub>-V<sub>S</sub>, Ni-MoS<sub>2</sub> and Ni-MoS<sub>2</sub>-V<sub>S</sub>.

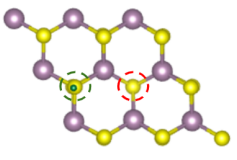
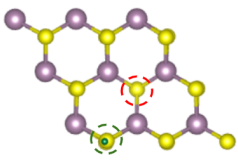
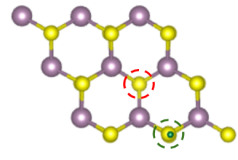
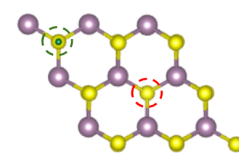
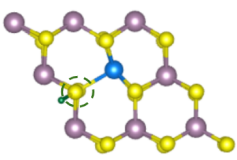
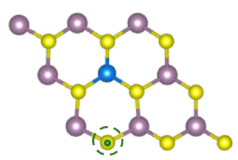
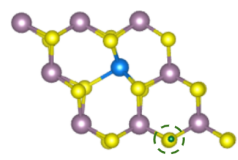
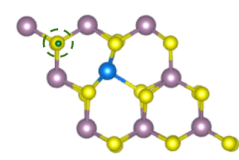
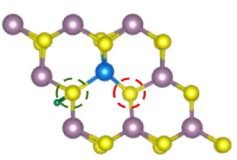
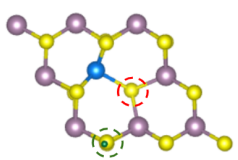
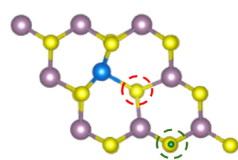
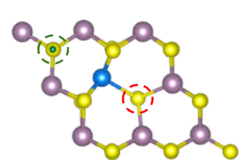
MoS <sub>2</sub> -V <sub>S</sub>	S1	S2	S3	S4
				
$\Delta G_H$ (eV)	1.51	1.51	1.51	1.60
Ni-MoS <sub>2</sub>	S1	S2	S3	S4
				
$\Delta G_H$ (eV)	-0.86	1.18	7.21	7.18
Ni-MoS <sub>2</sub> -V <sub>S</sub>	S1	S2	S3	S4
				
$\Delta G_H$ (eV)	0.49	1.27	1.26	1.22

Table 25: Structural configurations and differential hydrogen adsorption free energies ( $\Delta G_H^{diff}$ ) for different sulphur adsorption sites of the basal plane of MoS<sub>2</sub>-V<sub>S</sub>, Ni-MoS<sub>2</sub> and Ni-MoS<sub>2</sub>-V<sub>S</sub>.

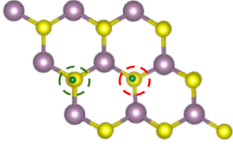
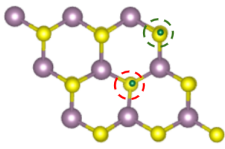
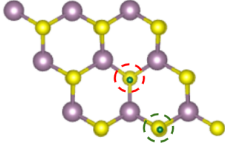
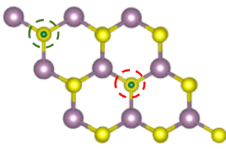
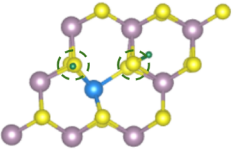
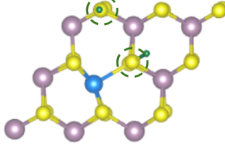
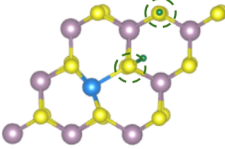
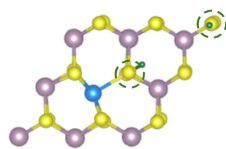
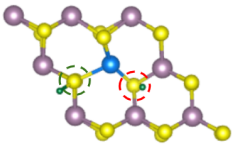
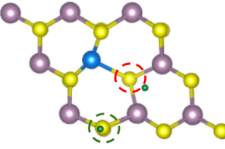
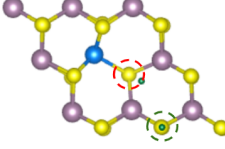
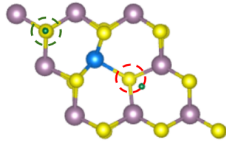
MoS <sub>2</sub> -V <sub>S</sub>	S1	S2	S3	S4
				
$\Delta G_H^{diff}$ (eV)	1.31	1.31	1.31	1.51
Ni-MoS <sub>2</sub>	S1	S2	S3	S4
				
$\Delta G_H^{diff}$ (eV)	0.96	1.18	1.22	1.06
Ni-MoS <sub>2</sub> -V <sub>S</sub>	S1	S2	S3	S4
				
$\Delta G_H^{diff}$ (eV)	0.08	1.16	1.27	1.25

Table 26: Hydrogen adsorption free energy  $\Delta G_H$  for Metal doped MoS<sub>2</sub>-V<sub>S</sub> for various adsorption sites of its basal plane.

Metal dopant	V <sub>S</sub>	$\Delta G_H$ (eV)					
		S0	S1	S2	S3	S4	S6
Ni	0.007	1.378	0.488	1.267	1.256	1.225	1.278
Pt	-0.012	1.517	1.461	1.416	1.447	1.359	1.488
Pd	-0.023	1.244	0.428	1.324	1.347	1.299	1.411
Au	-0.049	0.521	0.258	0.960	0.999	1.014	1.015
W	0.052	0.026	1.626	1.534	1.533	1.636	1.588
Pb	0.057	0.930	0.376	0.928	1.046	0.891	1.021
Mo	0.058	3.588	1.512	1.510	1.511	1.599	1.553
Os	-0.065	-0.086	1.473	1.546	1.480	1.651	1.690
Cu	-0.072	0.889	0.046	1.109	1.099	1.035	1.069
Ru	-0.114	-0.118	1.300	1.476	1.423	1.543	1.583
Cr	-0.124	-0.119	1.187	1.331	1.293	1.355	1.313
Fe	-0.133	-0.140	1.049	1.400	1.296	1.409	1.416
Re	-0.139	-0.140	1.473	1.366	1.351	1.517	1.517
Ir	-0.139	-0.148	1.135	1.317	1.260	1.336	1.414
Co	-0.153	1.234	0.867	1.234	1.111	1.590	1.188
Rh	-0.169	1.489	0.455	1.257	1.193	1.235	1.311
Zn	-0.189	0.585	0.084	0.953	0.927	0.834	0.875
Ag	-0.214	0.689	-0.072	0.890	0.959	0.706	0.980
Mn	-0.290	-0.296	1.081	1.245	1.192	1.296	1.291
Ti	-0.585	0.736	0.601	0.836	0.810	0.757	0.729
V	-0.757	0.687	0.509	0.678	0.646	0.671	0.671
Hf	-0.818	0.643	0.492	0.633	0.656	0.596	0.580
Zr	-0.822	2.603	0.440	0.599	0.648	0.568	0.556
Nb	-0.867	6.877	0.504	0.565	0.574	0.573	0.533
Ta	-0.900	0.693	0.520	0.557	0.543	0.568	0.515

Table 27: Differential hydrogen adsorption free energy  $\Delta G_H^{diff}$  for Metal-doped MoS<sub>2</sub>-V<sub>S</sub>.

Metal dopant	$\Delta G_H^{diff}$ (eV)
Ni	0.076
Pt	1.400
Pd	0.297
Au	-0.307
W	1.391
Pb	0.297
Mo	1.313
Os	1.312
Cu	-0.269
Ru	0.735
Cr	1.151
Fe	0.866
Re	1.590
Ir	1.244
Co	0.927
Rh	0.476
Zn	-0.154
Ag	-0.184
Mn	1.204
Ti	0.372
V	1.216
Hf	0.422
Zr	0.382
Nb	1.283
Ta	1.317

Table 28: Structural configurations for  $V_S$  adsorption site after hydrogen adsorption on Metal-doped  $MoS_2-V_S$  systems. Red cycle denotes the sulphur vacancy.

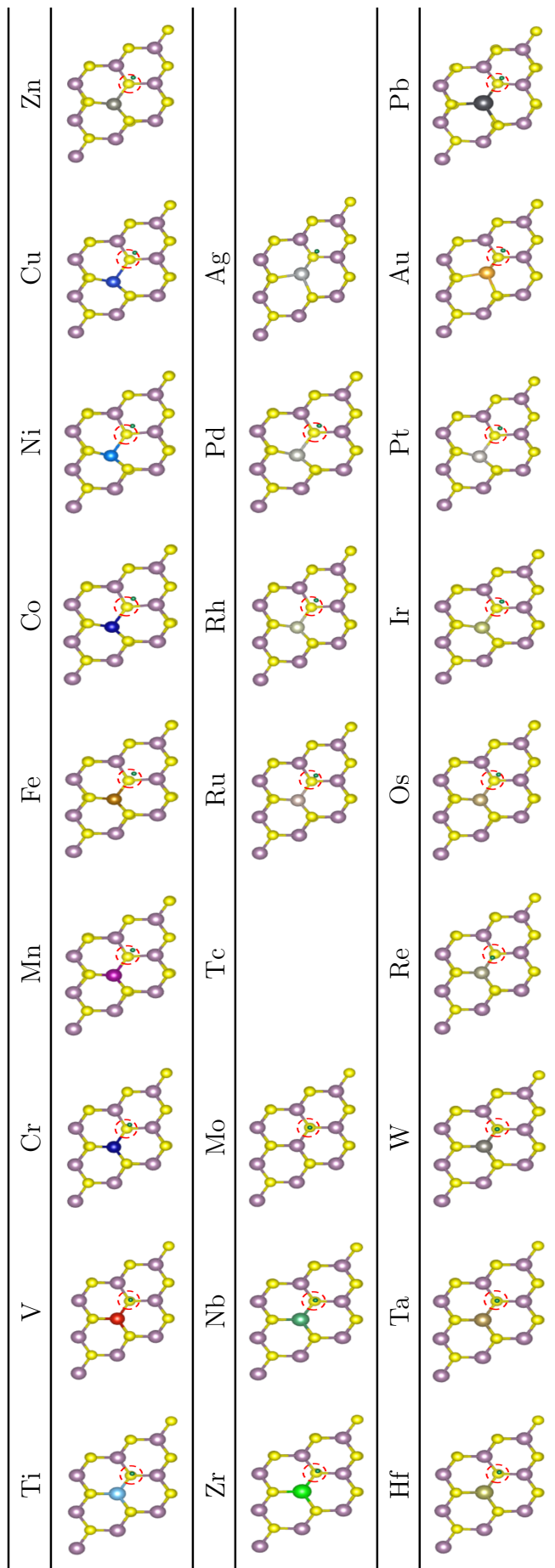


Table 29: Structural configurations for S0 adsorption site after hydrogen adsorption on Metal-doped  $\text{MoS}_2\text{-V}_5$  systems. Red and green cycles denote the sulphur vacancy and the metal adsorption site.

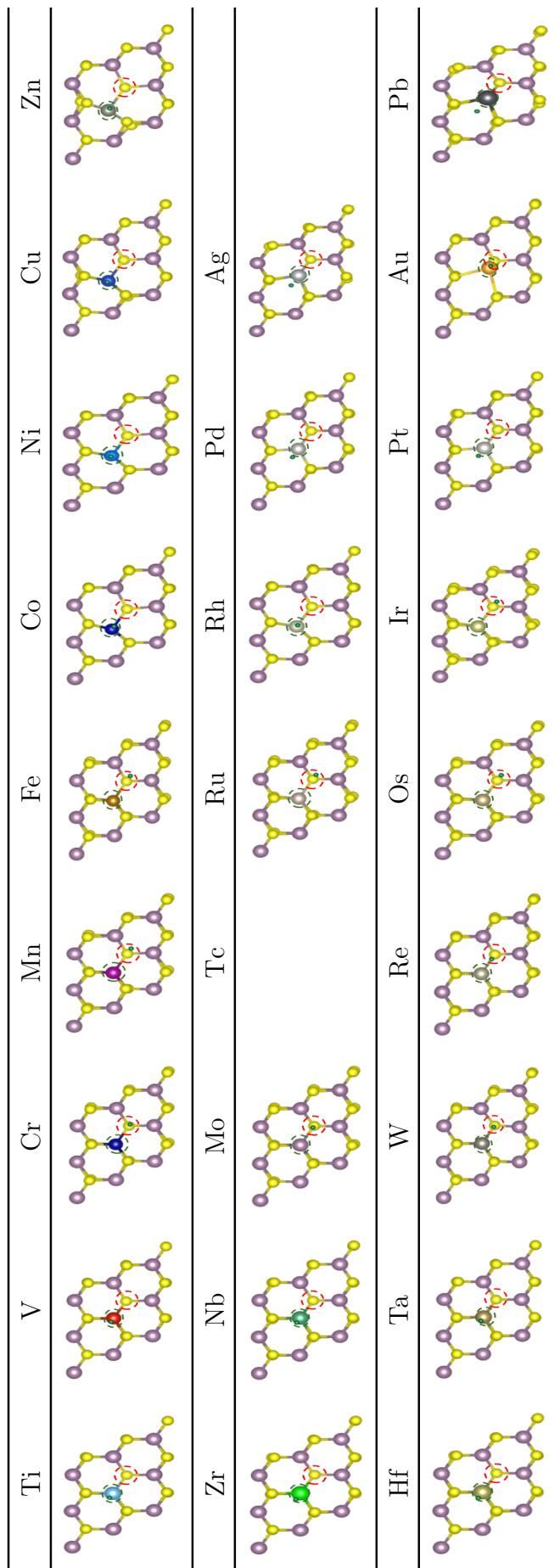


Table 30: Structural configurations for S1 adsorption site after hydrogen adsorption on Metal-doped  $\text{MoS}_2\text{-V}_5$  systems. Red and green cycles denote the sulphur vacancy and the metal adsorption site.

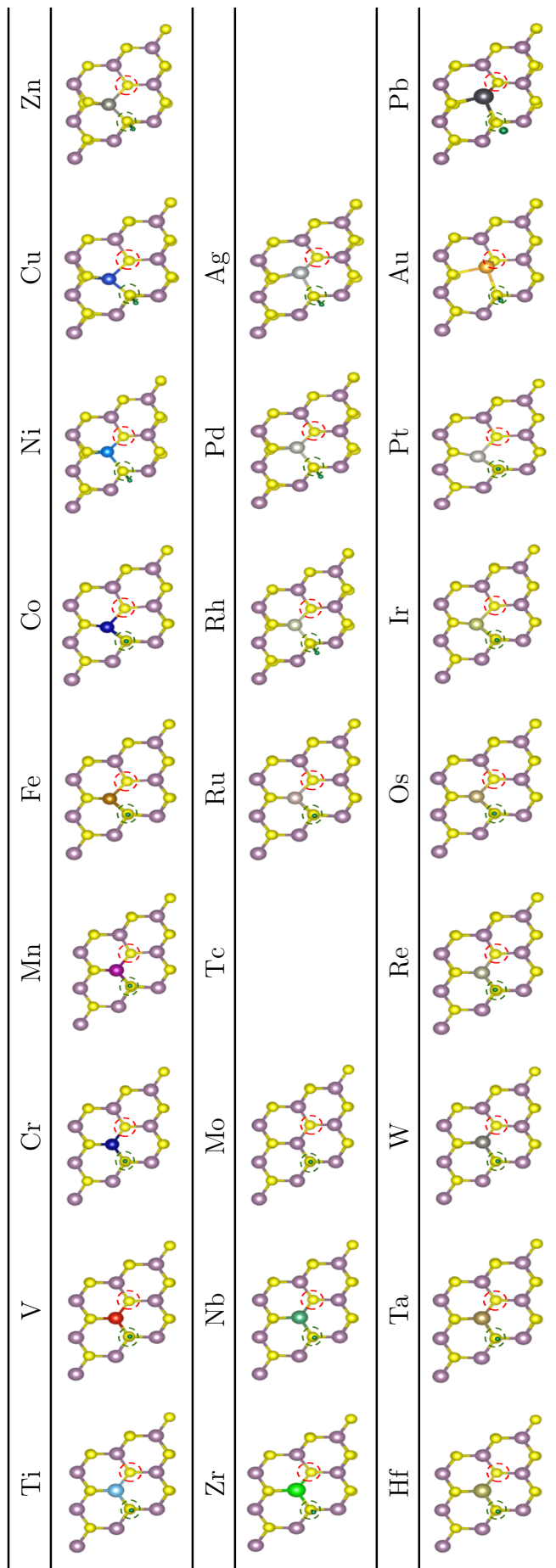
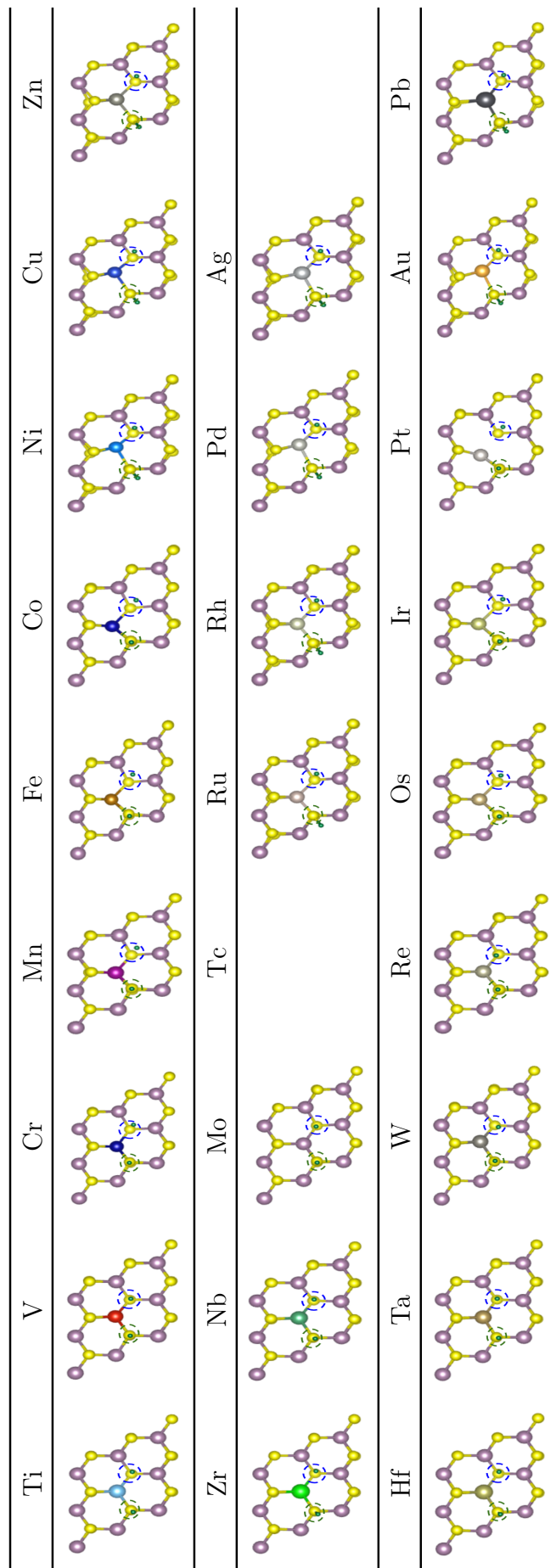


Table 31: Structural configurations for  $V_S$  and S1 adsorption sites after hydrogen adsorption on Metal doped  $\text{MoS}_2\text{-V}_S$  systems. Red and green cycles denote the sulphur vacancy and the metal adsorption site.



## 8 References

- [1]J. K. Nørskov, F. Abild-Pedersen, F. Studt and T. Bligaard. Density functional theory in surface chemistry and catalysis. *PNAS*, 108:937-943, 2011
- [2]J. K. Nørskov, T. Bligaard, J. Rossmeisl and C. H. Christensen. Towards the computational design of solid catalysts. *Nature Chem.*, 1:37-46, 2009
- [3]T. F. Jaramillo et al. Identification of active edges for electrochemical H<sub>2</sub> evolution from MoS<sub>2</sub> nanocatalysts. *Science*, 317:100-102, 2007
- [4]J. Greeley et al. Computational high-throughput screening of electrocatalytic materials for hydrogen evolution. *Nature Mater.* 5:909-913, 2006
- [5]K. Honkala, A. Hellman, I. N. Remediakis, A. Logadottir, A. Carlsson, S. Dahl, C. H. Christensen, J. K. Nørskov. Ammonia Synthesis from First Principle Calculations. *Science*, 307:55-558, 2005
- [6]B. Hinnemann, P. G. Moses, et al. Biomimetic Hydrogen Evolution: MoS<sub>2</sub> Nanoparticles as Catalysts for Hydrogen Evolution Reaction. *J. Am.Chem.Soc.*, 127:5308-5309, 2005
- [7]J. K. Nørskov, T. Bligaard, A. Logadottir, J. R. Kitchin. Trends in the Exchange Current for Hydrogen Evolution, *J. Electrochem. Soc.*, 152:J23-J26, 2005
- [8]C. J. H. Jackobsen, S. Dahl, A. Boisen, B. S. Clausen and J.K.Nørskov. Optimal Catalyst Curves: Connecting Density Functional Theory Calculations with Industrial Reactor Design and Catalyst Selection. *J. Catal.*, 205:382-387, 2002
- [9]J. D. Benck, T. R. Hellstern, J. Kibsgaard, P. Chakthranont and T. F. Jaramillo. Catalyzing the Hydrogen Evolution Reaction (HER) with Molybdenum Sulfide Nanomaterials. *ACS Catal.*, 4:3957-3971, 2014
- [10]Z. W. Seh et al. Combining theory and experiment in electrocatalysis: Insights into materials design. *Science*, 355:146, 2017
- [11]S. J. Gutic, et al. Hydrogen Evolution Reaction-From Single Crystal to Single Atom Catalysts. *Catalysis*, 10:290, 2020
- [12]Y. Jiao, Y. Zheng, M. Jaroniec and S. Z. Qiao. Design of electrocatalysts for oxygen- and hydrogen- involving energy conversion reactions. *Chem. Soc. Rev.*, 44: 2023-2576, 2015
- [13]R. Gomez, J. M. Feliu and A. Aldaz. Effects of irreversibly adsorbed bismuth on hydrogen adsorption and evolution on Pt(111). *Electrochim. Acta*, 42:1675-1683, 1997

- [14]F. Sabatier. La catalyse en chimie organique, Berauge: Paris, 1920.
- [15]S. Trasatti. Work function, electronegativity and electrochemical behaviour of metals. *J. Electroanal. Chem*, 39:163, 1972
- [16]P. Quaino, F. Juarez, E. Santos and W. Schmickler. Volcano plots in hydrogen electrocatalysis-uses and abuses. *Beilstein J. Nanotechnol.*, 5:846-85, 2014
- [17]R. A. Marcus. On the Theory of Oxidation-Reduction Reactions Involving Electron Transfer.I. *J. Chem. Phys.* 24:966, 1956
- [18]N. M. Markovic, B. N. Grgur, P. N. Ross. Temperature-Dependent Hydrogen Electrochemistry on Platinum Low-Index Single-Crystal Surfaces in Acid Solutions. *J. Phys. Chem. B*, 101:5405, 1997
- [19]B. E. Conway, B. V. Tilak. Interfacial processes involving electrocatalytic evolution and oxidation of H<sub>2</sub>, and the role of chemisorbed H. *Electrochim. Acta*, 47:3571, 2002
- [20]E. Skulason et al. Density functional theory calculations for the hydrogen evolution reaction in an electrochemical double layer on the Pt(111) electrode. *Phys. Chem. Chem. Phys.*, 9: 3241, 2007
- [21]C. Tsai, K. Chan, J.K. Norskov and F. Abild-Pedersen. Rational design of MoS<sub>2</sub> catalysts: tuning the structure and activity via transition metal doping. *Catal. Sci. Technol.*, 5:246-253, 2015
- [22]M. Hakala, R. Kronberg and K. Laasonen. Hydrogen adsorption on doped MoS<sub>2</sub> nanostructures. *Scientific Reports*, 7: 15243, 2017
- [23]H. Tributsch, J. C. Bennet. Electrochemistry and photochemistry of MoS<sub>2</sub> layer crystals.1. *J. Electroanal. Chem.*, 81:97-111, 1977
- [24]B. Hinnemann and J. K. Nørskov. Chemical Activity of the Nitrogenase FeMo Cofactor with a Central Nitrogen Ligand: Density Functional Study. *J. Am.Chem.Soc.*, 126:3920-3927, 2004
- [25]C. Tsai, K. Chan, J. K. Nørskov and F. Abild-Pedersen. Theoretical insights into the hydrogen evolution activity of layered transition metal dichalcogenides. *Surface Science*, 640: 133-140, 2015
- [26]J. Kibsgaard, Z.Chen, B. N. Reinecke, T.F.Jaramillo. Engineering the surface structure of MoS<sub>2</sub> to preferentially expose active edge sites for electrocatalysis. *Nat. Mater.*, 11:963-969, 2012

- [27]Z. Chen, D. Cummins, B. N. Reinecke, E. Clark, M. K. Sunkara and T. F. Jaramillo. Core shell MoO<sub>3</sub>-MoS<sub>2</sub> nanowires for hydrogen evolution: A functional design for electrocatalytic materials. *Nano Lett.*, 11:4168-4175, 2011
- [28]D. Kong, H. Wang, J. J. Cha, M. Pasta, K. J. Koski, J. Yao and Y. Cui. Synthesis of MoS<sub>2</sub> and MoSe<sub>2</sub> films with vertically aligned layers. *Nano Lett.*, 13:1341-1347, 2013
- [29]H. Wang et al. Electrochemical tuning of vertically aligned layers. *Nano Lett.* 13:1341-1347, 2013
- [30]Y. Li et al. MoS<sub>2</sub> nanoparticles grown on graphene: An advanced catalyst for the hydrogen evolution reaction. *J. Am. Chem. Soc.* 133: 7296-7299, 2011
- [31]A. E. Maniadaki and G. Kopidakis. Hydrogen on hybrid MoS<sub>2</sub>/graphene nanostructures. *Phys. Status Solidi RRL*, 10:453-457, 2016
- [32]M. A. Lukowski, A. S. Daniel, F. Meng, A. Forticaux, L. Li, and S. Jin. Enhanced hydrogen evolution catalysis from chemically exfoliated metallic MoS<sub>2</sub> nanosheets. *J. Am. Chem. Soc.* 135:10274-10277, 2013
- [33]D. Voiry et al. Conducting MoS<sub>2</sub> nanosheets as catalysts for hydrogen evolution reaction. *Nano Lett.*, 13:6222-6227, 2013
- [34]D. Voiry et al. Enhanced catalytic activity in strained chemically exfoliated WS<sub>2</sub> nanosheets for hydrogen evolution. *Nat. Mater.*, 15:48-53, 2013
- [35]Q. Tang and D. Jiang. Mechanism of Hydrogen Evolution Reaction on 1T-MoS<sub>2</sub> from First Principles. *ACS Catal.*, 6:4953-4961, 2016
- [36]Y. Hao et al. 1T-MoS<sub>2</sub> monolayer doped with isolated Ni atoms as highly active hydrogen evolution catalysts: A density functional study. *Applied Surface Science.*, 469: 292-297, 2019
- [37]D. Merki, S. Fierro, H. Vrubel and X. Hu. Amorphous molybdenum sulfide films as catalysts for electrochemical hydrogen production in water. *Chem. Sci.*, 2:1262-1267, 2011
- [38]J. D. Benck, Z. Chen, L. Y. Kuritzky, A. J. Forman, and T. F. Jaramillo. Amorphous Molybdenum Sulfide Catalysts for Electrochemical Hydrogen Production: Insights into the Origin of their Catalytic Activity. *ACS Catal.*, 2:1916-1923, 2012
- [39]D. Bae, B. Seger, P. C. K. Vesborg, O. Hansen and I. Chorkendorff. Strategies for stable water splitting via protected photoelectrodes. *Chem. Soc. Rev.*, 46:1933-1954, 2017

[40]L. Wu et al. The Origin of High Activity of Amorphous MoS<sub>2</sub> in the Hydrogen Evolution Reaction. *ChemSusChem*, 12:4383–4389, 2019

[41]H. G. S. Casalongue et al. Operando Characterization of an Amorphous Molybdenum Sulfide Nanoparticle Catalyst during the Hydrogen Evolution Reaction. *J.Phys. Chem. C*, 118:29252-29259, 2014

[42]D. Merki, H. Vrubel, L. Rovelli, S. Fierro and X. Hu. Fe, Co, and Ni ions promote the catalytic activity of amorphous molybdenum sulfide films for hydrogen evolution. *Chem. Sci.*, 3:2515-2525, 2012

[43]Y. Yan, B. Xia, Z. Xu and X. Wang. Recent Development of Molybdenum Sulfides as Advanced Electrocatalysts for Hydrogen Evolution Reaction. *ASC. Catal.*, 4:1693-1705, 2014

[44]J. Kristensen, J. Zhang, I. Chorkendorff, J. Ulstrup and B. L. Ooi. Assembled monolayers of [Mo<sub>3</sub>S<sub>4</sub>]<sup>4+</sup> clusters on well-defined surfaces. *Dalton Trans.*, 2006:3985-3990, 2006

[45]T. F. Jaramillo et al. Hydrogen Evolution on Supported Incomplete Cubane-type [Mo<sub>3</sub>S<sub>4</sub>]<sup>4+</sup> Electrocatalysts. *J. Phys. Chem. C*, 112:17492-17498, 2008

[46]H. I. Karunadasa et al. A Molecular MoS<sub>2</sub> Edge Site Mimic for Catalytic Hydrogen Generation. *Science*, 335:698-702, 2012

[47]J. Kibsgaard, T. F. Jaramillo and F. Besenbacher. Building an appropriate active-site motif into a hydrogen-evolution catalyst with thiomolybdate [Mo<sub>3</sub>S<sub>13</sub>]<sup>2-</sup> clusters. *Nat. Chem.*, 6:248-253, 2014

[48]L. S. Byskov, J. K. Norskov, B. S. Clausen and H. Topsøe. DFT Calculations of Unpromoted and Promoted MoS<sub>2</sub>-Based Hydrodesulfurization Catalysts. *Journal of Catalysis*, 187:109-122, 1999

[49]H. Li et al. Activating and optimizing MoS<sub>2</sub> basal planes hydrogen evolution through the formation of strained sulphur vacancies. *Nature Materials*, 15:48-53, 2016

[50]G. Ye et al. Defects engineered monolayer MoS<sub>2</sub> for improved hydrogen evolution reaction. *Nano Lett.*, 16:1097-1103, 2016

[51]C. Tsai, et al. Electrochemical generation of sulfur vacancies in the basal plane of MoS<sub>2</sub> for hydrogen evolution. *Nature Communication*, 8:15113, 2017

[52]J. Deng et al. Triggering the electrocatalytic hydrogen evolution activity of the inert two-dimensional MoS<sub>2</sub> surface via single-atom metal doping. *Energy Environ.*, 8:1594-1601, 2015

[53]T. H. M. Lau et al. Transition metal atom doping of the basal plane of MoS<sub>2</sub> monolayer nanosheets for electrochemical hydrogen evolution. *Chem. Sci.*, 9:4769-4776, 2018

[54]J. J. L. Humphrey, R. Kronberg, R. Cai, K. Laasonen, R. E. Palmer and A.j. Wain. Active site manipulation in MoS<sub>2</sub> cluster electrocatalysts by transition metal doping. *Nanoscale*, 12:4459-4472, 2020

[55]M. Liu, M. S. Hybertsen and Q. Wu. A Physica Model for Understanding the Activation of MoS<sub>2</sub> Basal-plane Sulfur Atoms for the Hydrogen Evolution Reaction. *Angew. Chem. Int. Ed.* 10.1002/anie.202003091, 2020

[56]B. Hammer and J. K. Nørskov. Why is the gold the noblest of all the metals. *Nature*, 376:238-240, 1995

[57]A. Nilsson, L. G. M. Pettersson, B. Hammer, T. Bligaard, C.H. Christensen and J.K. Nørskov. The electronic structure effect in heterogeneous catalysis. *Catal. Lett.*, 100:111-114, 2005

[58]J. K. Nørskov, F. Abild-Pedersen, F. Studt and T. Bligaard. Density functional theory in surface chemistry and catalysis. *PNAS*, 108:937-943, 2011

[59]C. Tsai, K. Chan, F. Abild-Pedersen and J. K. Nørskov. Active edge sites in MoS<sub>2</sub> and WSe<sub>2</sub> catalysts for the hydrogen evolution reaction: a density functional theory. *Phys. Chem. Chem Phys.*, 16:13156-13164, 2014

[60]W. Kohn. Electronic structure of matter-wave functions and density functionals. *Rev. Mod. Phys.*, 71 :1253, 1999

[61]D. S. Sholl and J. A. Steckel. *Density Functional Theory: A Practical Introduction*. Wiley, 2009

[62]R. M. Martin. *Electronic Structure Basic Theory and Practical Methods*. Cambridge University Press, 2004

[63]E. N. Economou, *Solid State Physics: A shortened version*. . Crete University Press, 2017

[64]W. Kohn and L. J. Sham. Self-consistent equations including exchange and correlation effects. *Phys. Rev. A.* 140:1133–1138, 1965

[65]S. Cottenier, Online Courses on Computational Materials Physics, Ghent University.(  
<http://www.compmatphys.org>)

[66]A. E. Mattsson. In Pursuit of the "Divine" Functional. *Science*, 298 :759, 2002

[67]P. Hohenberg and W. Kohn. Inhomogeneous electron gas. *Phys. Rev. B*, 136: 864–871, 1964

[68]P. Schwerdtfeger. The Pseudopotential Approximation in Electronic Structure Theory. *ChemPhysChem*, 12: 3143–3155, 2011

[69]J. Thijssen. *Computational Physics*. Cambridge University Press, 2007

[70]By Wolfram Quester - Own workThis PNG graphic was created with Inkscape., Public Domain, <https://commons.wikimedia.org/w/index.php?curid=10227075>

[71]P. E. Blochl. Projector augmented wave-method. *Physical Review B*, 50:24, 1994

[72]G. Kresse and J. Hafner. Ab initio molecular dynamics for liquid metals. *Phys. Rev. B*, 47: 558, 1993

[73]G. Kresse and J. Hafner. Ab initio molecular-dynamics simulation of the liquid-metal amorphous-semiconductor transition in germanium. *Phys. Rev. B*, 49: 14251, 1994

[74]G. Kresse and J. Furthmuller, Efficiency of ab-initio total energy calculations for metals and semiconductors using a plane-wave basis set. *Comput. Mater. Sci.*, 6: 15, 1996

[75]G. Kresse and J. Furthmuller. Efficient iterative schemes for ab initio total-energy calculations using a plane-wave basis set. *Phys. Rev. B*, 54: 11169, 1996

[76]P. E. Blochl. Improved tetrahedron method for Brillouin-zone integrations. O. Jepsen, and O. K. Andersen, *Phys. Rev. B*, 49: 16223, 1994.

[77]G. Kresse and D. Joubert. From ultrasoft pseudopotentials to the projector augmented-wave method. *Phys. Rev. B*, 59: 1758, 1999

[78]J. P. Perdew, K. Burke, and M. Ernzerh. Generalized Gradient Approximation Made Simple *Phys. Rev. Lett.*, 77: 3865, 1996

[79]J. Wilson and A. D. Yoffe.The transition metal dichalcogenides discussion and interpretation of the observed optical, electrical and structural properties.*Adv. Phys.*18:193-000,1969

[80]K. K. Kam and B. A. Parkinson. Detailed photocurrent spectroscopy of the semiconducting group VIB transition metal dichalcogenides. *J.Phys.Chem.*, 86:463-467.1982

[81]A. Kumar and P. K. Ahluwalia. Electronic structure of transition metal dichalcogenides monolayers  $1H-MX_2$  ( $M = Mo, W$ ;  $X = S, Se, Te$ ) from ab-initio theory: new direct band gap semiconductors

[82]A. Kumar and P. K. Ahluwalia. A first principle Comparative study of electronic and optical properties of  $1H - MoS_2$  and  $2H - MoS_2$ .*Materials Chemistry and Physics*.135:755-761.135:755-761

[83]Z. M. Wang. *Materials ,Physics, Devices. Lecture Notes in Nanoscale Science and Technology*.Springer.2014

[84]A. E. Maniadaki, G. Kopidakis, I. Remediakis. Strain engineering of electronic properties of transition metal dichalcochenide monolayers. *Solid State Communications*, 227:33-39, 2016

[85]R. Kronberg, M. Hakala, N. Holmberg and K. Laasonen. Hydrogen adsorption on  $MoS_2$ -surfaces: a DFT study on preferential sites and the effect of sulfur and hydrogen coverage. *Phys. Chem. Chem. Phys.*19:16231-16241,2017

[86]H.-P. Komsa and A. V. Krasheninnikov. Native defects and monolayer  $MoS_2$  from first principles. *Physical Review B*, 91: 125304-125317, 2015

[87]NIST Computational Chemistry Comparison and Benchmark Database NIST Standard Reference Database Number 101 Release 20, August 2019, Editor: Russell D. Johnson III <http://cccbdb.nist.gov/DOI:10.18434/T47C7Z>

[88]E. Kaxiras. *Atomic and Electronic Structure of Solids*. Cambridge: Cambridge University Press, 2003.